


Alveolar macrophage-expressed Plet1 is a driver of lung epithelial repair after viral pneumonia

Received: 1 February 2023

Accepted: 13 December 2023

Published online: 02 January 2024

 Check for updates

Leartha Pervizaj-Oruqaj ^{1,2,3,12}, Balachandar Selvakumar ^{1,4,5,12}, Maximiliano Ruben Ferrero ^{1,2,3,4,5,12}, Monika Heiner^{1,2,3}, Christina Malainou ^{1,2,3}, Rolf David Glaser ^{2,6}, Jochen Wilhelm ^{2,3,7}, Marek Bartkuhn^{2,6}, Astrid Weiss ^{3,7}, Ioannis Alexopoulos ^{1,2,3}, Biruta Witte⁸, Stefan Gattenlöhner⁹, István Vadász ^{2,3,7}, Rory Edward Morty ¹⁰, Werner Seeger ^{2,3,4,5,7}, Ralph Theo Schermuly ^{2,3,7}, Ana Ivonne Vazquez-Armendariz ^{1,2,3,11} & Susanne Herold ^{1,2,3} 

Influenza A virus (IAV) infection mobilizes bone marrow-derived macrophages (BMDM) that gradually undergo transition to tissue-resident alveolar macrophages (TR-AM) in the inflamed lung. Combining high-dimensional single-cell transcriptomics with complex lung organoid modeling, in vivo adoptive cell transfer, and BMDM-specific gene targeting, we found that transitioning (“regenerative”) BMDM and TR-AM highly express *Placenta-expressed transcript 1* (Plet1). We reveal that Plet1 is released from alveolar macrophages, and acts as important mediator of macrophage-epithelial cross-talk during lung repair by inducing proliferation of alveolar epithelial cells and re-sealing of the epithelial barrier. Intratracheal administration of recombinant Plet1 early in the disease course attenuated viral lung injury and rescued mice from otherwise fatal disease, highlighting its therapeutic potential.

Tissue-resident alveolar macrophages (TR-AM) are long-lived cells¹ localized to the alveolar space, where they exert key functions in maintaining tissue homeostasis and in immediate host defense. Several studies revealed that TR-AM are depleted upon viral pneumonia and gradually replaced by BMDM (CD11c⁺CD11b⁺Ly6C⁺CX3CR1⁺) during the infection course, eventually resulting in reprogramming of the TR-AM pool^{1–4}. BMDM are recruited to sites of infection via CCR2 ligation⁵

and are considered to reveal high functional plasticity. Polarization of BMDM into different macrophage phenotypes in the infected lung is thought to be driven by integration of spatially and timely resolved signals from the inflamed microenvironment or tissue niche in a disease-specific manner^{6,7}. Whereas pro-inflammatory macrophages were found to contribute to the severity of viral pneumonia by directly damaging the lung parenchyma, and to aberrant lung remodeling^{8–11},

¹Department of Internal Medicine V, Universities of Giessen and Marburg Lung Center, University Hospital Giessen, Justus Liebig University, Member of the German Center for Lung Research (DZL), Giessen, Germany. ²Institute for Lung Health (ILH), Justus Liebig University, Giessen, Germany. ³Excellence Cluster Cardio-Pulmonary Institute (CPI), Giessen, Germany. ⁴Max Planck Institute for Heart and Lung Research, Bad Nauheim, Germany. ⁵Instituto de Investigación en Biomedicina de Buenos Aires (iBiBA), Buenos Aires, Argentina. ⁶Biomedical Informatics and Systems Medicine, Justus Liebig University, Giessen, Germany. ⁷Department of Internal Medicine II, Universities of Giessen and Marburg Lung Center, University Hospital Giessen, Justus Liebig University, Member of the German Center for Lung Research (DZL), Giessen, Germany. ⁸Department of General and Thoracic Surgery, University Hospital of Giessen, Giessen, Germany. ⁹Department of Pathology, University Hospital of Giessen, Giessen, Germany. ¹⁰Department of Translational Pulmonology and the Translational Lung Research Center, University Hospital Heidelberg, Member of the German Center for Lung Research (DZL), Heidelberg, Germany. ¹¹University of Bonn, Transdisciplinary Research Area Life and Health, Organoid Biology, Life & Medical Sciences Institute, Bonn, Germany. ¹²These authors contributed equally: Leartha Pervizaj-Oruqaj, Balachandar Selvakumar, Maximiliano Ruben Ferrero. ✉e-mail: Susanne.herold@innere.med.uni-giessen.de

the role of distinct macrophage subsets in lung repair, and in particular their effector molecules mediating cross-talk with lung epithelial (stem/progenitor) cells during such processes are poorly understood. Nevertheless, mounting evidence supports that recruitment and expansion of macrophages are necessary to promote tissue regeneration after injury¹². Efforts to elucidate the molecular mechanisms by which macrophages support the expansion of epithelial (stem/progenitor) cells, increase their resilience towards injury and infection, or halt their apoptotic death aim to prevent the rapid decline of gas exchange function associated with severe pneumonia, and to accelerate its re-establishment through coordinated regeneration processes. Indeed, a recent study revealed airway epithelial repair driven by an IL-33/ST2-induced macrophage differentiation program, and signals activating the IL-4 receptor on BMDM accelerated de novo lung tissue formation after pneumonectomy^{13,14}.

Placenta-expressed transcript 1 (Plet1) is a 207 amino acid glycosylphosphatidylinositol (GPI)-anchored protein with unknown receptor, expressed in proliferating epithelia and in stem cell niches, such as differentiating trophoblasts^{15,16}, follicular and thymic stem cells^{17–19}. It is involved in keratinocyte migration²⁰ and gut epithelial wound healing from the Lgr5⁺ colon stem cell niche²¹. We and others recently identified its expression in myeloid cells and its role in dendritic cell migration and in the instruction of innate lymphoid cells to release IL-22^{22–24} (data accessible at NCBI GEO database, GEO accession GDS1874). However, its expression pattern and function in the context of lung injury and regeneration have been unknown.

Here, we reveal that during the resolution phase of viral pneumonia a transitional subpopulation of BMDM and the re-emerging TR-AM pool constitute key components of epithelial stem/progenitor cell niches and contribute to lung regeneration after injury through the expression of Plet1. Using bone marrow chimeric mice and single-cell transcriptome data, we confirmed the spatiotemporal kinetics of the BMDM-to-TR-AM transition, and captured that this trajectory is associated with distinct functional phenotypes from inflammatory towards tissue-regenerative, characterized by gradual increase of Plet1 expression. Adoptive transfer of Plet1⁺ macrophage populations sampled along this differentiation trajectory, into *Ccr2*^{-/-} mice, combined with conditional CX₃CR1^{iCRE}-Plet1^{lox/tom} transgenic mouse and lung organoid assays modeling the macrophage-epithelial niche during alveologenesis, revealed that Plet1⁺ macrophages efficiently attenuate influenza A virus (IAV)-induced epithelial injury and foster stem/progenitor cell-driven alveolarization and barrier repair. Finally, intra-alveolar administration of recombinant Plet1 rescued mice from fatal viral pneumonia, highlighting its potential as a therapeutic to combat severe inflammatory lung injury in viral pneumonia.

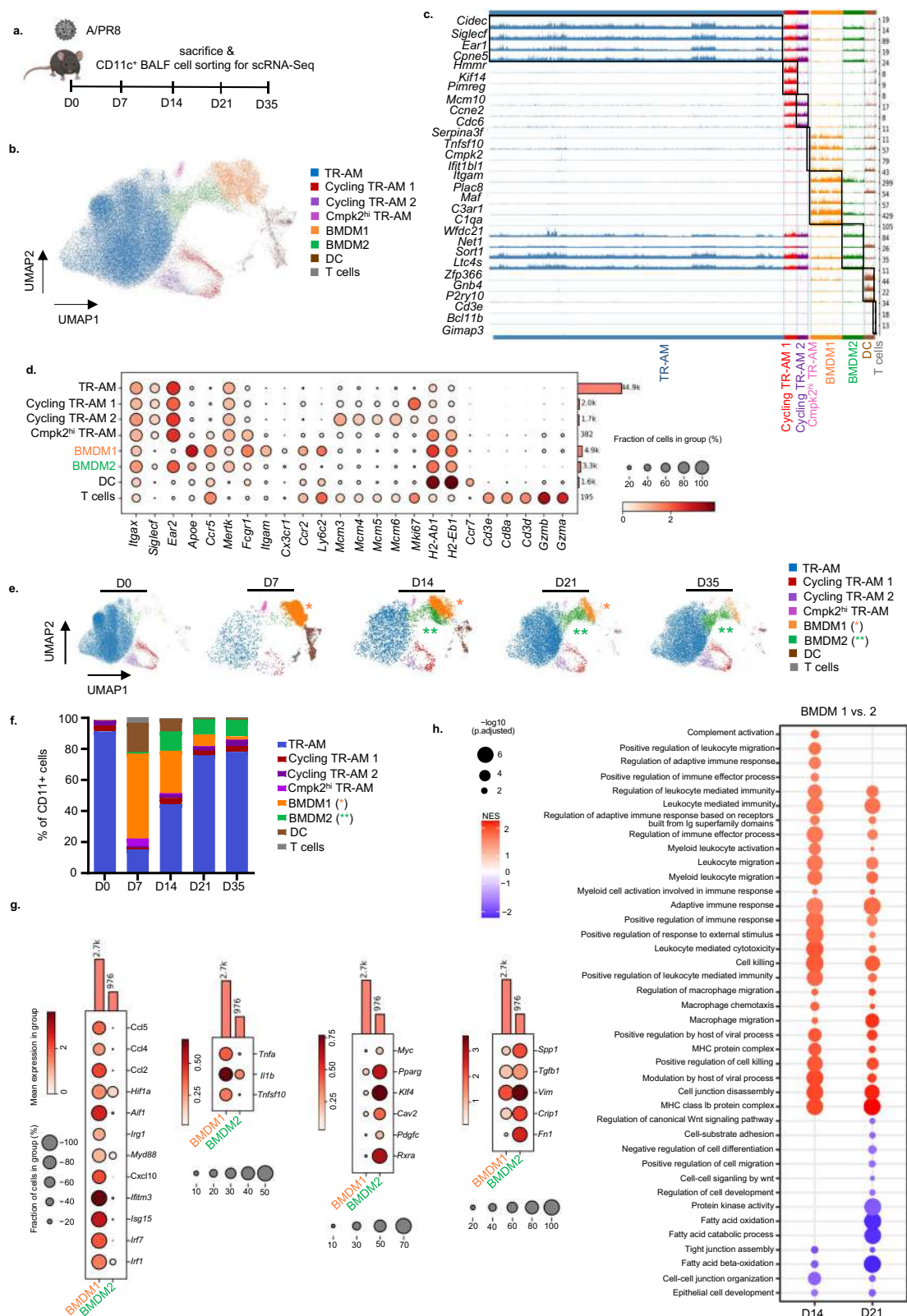
Results

Alveolar macrophages cluster into TR-AM and CD40^{high} inflammatory versus CD206^{high} transitional BMDM subsets that reveal a regenerative phenotype in IAV-infected mice

Macrophage-epithelial interactions during epithelial repair were suggested to widely occur in the bronchoalveolar airspace compartment^{25,26}. To map the dynamics of macrophage composition and phenotypes in the intraalveolar compartment of the murine lung after IAV infection, flow-sorted CD11c⁺ bronchoalveolar lavage fluid (BALF) cells were profiled by single-cell (sc) RNA-seq at the indicated time post infection (p.i.), capturing the alveolar injury and resolution phase of the infection (Fig. 1a and Supplementary Fig. 1a). Unsupervised clustering over all time points distributed cells into 8 transcriptionally distinct clusters of CD11c⁺ cells (Fig. 1b). As shown in Fig. 1c (depicting the 3–5 top differentially expressed genes in each cluster) and Fig. 1d (depicting selected/canonical marker genes), we identified a population of antigen-presenting dendritic cells (DC; expressing *H-2* MHC II genes, *Ccr7*, and the conventional DC1 marker *Zfp366*, coding for DC-SCRIPT²⁷) and a cluster of CD11c⁺ cytotoxic T

cells (expressing *Cd3d*, *Cd3e*, *CD8a*, *Ccr5*, and granzymes (*Grzma*/*Grzmb*)²⁸. TR-AM were characterized by expression of *Siglec*, *Ear2*, *Mertk*, and *Fabp1* (see also Supplementary Fig. 1b), and revealed two low-frequent proliferating subclusters (cycling TR-AM 1 and 2, characterized by genes associated with DNA replication, *Mcm3-6*, and by the proliferation marker *Mki67*, respectively). Another low-frequent TR-AM population expressed antiviral genes dependent on type I interferon signaling, such as *Tnfsf10*, *Ifit1b1*, and *Cmpk2*^{29,30} termed Cmpk2^{hi} TR-AM. Of note, two different clusters of BMDMs were identified (BMDM1/2). Compared to BMDM2, BMDM1 were *Ly6c2*^{high} and expressed higher levels of transcripts related to immediate immune response and inflammation, such as *Apoe*, complement-associated genes *C1qa* and *C3ar1*, *Fcgr1* (coding for the high-affinity Fc gamma receptor), *Itgam* (coding for CD11b), and of chemokine receptors (*Ccr2*, *Cx3cr1*, *Ccr5*). Resolution over time revealed distinct kinetics of alveolar CD11c⁺ cell clusters (for kinetics of TR-AM and BMDM marker genes, see Supplementary Fig. 1b). At D7 p.i., TR-AM (except Cmpk2^{hi} TR-AM) were widely depleted and gradually returned between D14 to D35 p.i. BMDM1 appeared in the alveoli at high frequency by D7 p.i., coinciding with the peak alveolar injury in this model¹¹, and their numbers declined until D35. Conversely, whereas few BMDM2 cells were already present in the airspace at day 7, their numbers increased at D14 and peaked at D21 p.i., coinciding with the phase of injury resolution, alveolar repair and return to homeostasis (Fig. 1e, f)⁸. In line, transcripts associated with antiviral host defense (*Irf1*, *Irf7*, *Isg15*, *Ifitm3*, *Cxcl10*), inflammation (*MyD88*, *Irf1*, *Aif1*, *Hif1a*), chemotaxis (*Ccl2*, *Ccl4*, *Ccl5*) or with epithelial injury induction (*Tnfsf10*, *Tnfa*, *Il1b*) were highly expressed in D7 BMDM1, whereas transcripts associated with alternative activation (*Pparg*, *Klf4*, *Myc*³¹, *Cau2*³², *Rxra*³³, tissue remodeling (*Fln*, *Vim*, *Tgfb1*), and cell growth (*Crip1*, *Pdgfc*) were higher in D21 BMDM2 (Fig. 1g), suggesting that BMDM2 might exert distinct functions in tissue regeneration. We next performed gene set enrichment analyses (GSEA) based on gene ontology (GO) terms in BMDM1/2 at D14 and 21 p.i. Differentially enriched GO terms are presented in Fig. 1h, revealing a predominant activation of genes related to inflammation and host defense in BMDM1 at both time points, while genes related to fatty acid metabolism, wnt signaling, tight junction (TJ) organization, and epithelial cell development were enriched in BMDM2. In addition, the BMDM2 cluster expressed genes or transcription factors associated with TR-AM identity (*Ear2*, *Mertk*, *Spp1*, *Sort1*, *Pparg*, *Klf4*; Supplementary Fig. 1b); thus, we hypothesized that this cluster represents a transitional state along the differentiation program into TR-AM driving return to tissue homeostasis^{3,34}. This hypothesis was further supported by trajectory inference by RNA velocity analysis of the scRNA-Seq dataset (Fig. 1) and partition-based graph abstraction (PAGA), predicting that BMDM1 transitioned to BMDM2, which in turn, represented an intermediate state towards differentiation into TR-AM clusters (Supplementary Fig. 1 c, d). In line with these data, using CD45.1/2 chimeric mice undergoing total body irradiation, BM transplant, and IAV infection after BM reconstitution (Supplementary Fig. 1e), depleted TR-AM of recipient (CD45.1) phenotype were gradually replenished between D14 and D21 by CD45.2⁺ BM-derived precursors, confirming that BMDM are able to replenish the TR-AM pool in this model (Supplementary Fig. 1f, g), as previously reported^{3,4,35}.

In an effort to correlate transcriptional heterogeneity of BMDM with unique functional phenotypes in the course of IAV infection, we aimed to establish a robust protocol to flow-sort BMDM subsets for further analyses, using distinct surface markers for identification. Out of several surface antigens differentially expressed according to the single cell transcriptome dataset in Fig. 1, we identified CD40 (*Cd40*) and CD206 (*Mrc1*) to be most suitable to identify BMDM1 and 2, respectively (Fig. 2a, b; gating strategy in Supplementary Fig. 2a). BMDM sub-phenotyping according to CD40^{high} and CD206^{high} populations by FACS reproduced the BMDM1/2 kinetics identified in the



scRNA-seq dataset (Fig. 1e and Supplementary Fig. 2b), with a peak accumulation of CD40^{high} BMDM1 at D7, and alveolar presence of CD206^{high} BMDM2 by D14 to D21 (Fig. 2c). BMDM kinetics in lung homogenates of pre-lavaged IAV-infected mice revealed similar kinetics as observed in the airspaces for BMDM1. However, BMDM2 appeared earlier in lung tissue, at day 10, and lower numbers of these cells were observed at later time points compared to BALF analyses,

likely capturing their rapid interstitial-to-alveolar transmigration (Supplementary Fig. 2c). To unambiguously verify that this gating strategy corresponded to the respective UMAP clusters of BMDM, we performed transcriptional profiling by cDNA microarray on BALF of flow-sorted CD40^{high} versus CD206^{high} BMDM, obtained on days 7 and 21 p.i., respectively. Data in Fig. 2d confirmed differential gene expression in CD206^{high} BMDM2 (genes associated with alternative

Fig. 1 | scRNA-seq analyses reveal two distinct alveolar BMDM clusters with defined kinetics of appearance over the course of IAV infection. **a** Schematic representation of the infection model and sample collection in uninfected mice (D0) and at the indicated time points p.i. The figure was created with BioRender. **b** Uniform manifold approximation and projection (UMAP) map displaying CD11c⁺ alveolar cell clusters (pooled data from all time points), integrated and embedded using the Harmony algorithm. Colors represent different cell populations after Leiden clustering in 1.4 resolution (58,998 individual cells with signals from 32,286 genes; average number per time point from $n = 3$ –5 mice). **c** Track plot showing unbiased analysis of the top three to five expressed genes in each particular cluster; pooled data from all time points. **d** Dot plot representing signature markers for each cell cluster. The size of the dots encodes the percentage of cells within a cluster expressing a particular marker. Color of the dots represents the average expression level throughout all cells within a cluster. **e** UMAP depiction of alveolar

CD11c⁺ cell clusters at the respective time points p.i. **f** Stacked bar chart showing the percentage of CD11c⁺ cells during the infection course. **g** Dot plots displaying expression of selected phenotype markers in BMDM1 and BMDM2 populations. Genes shown in the plot were selected among the significantly higher expressed genes ($p < 0.05$). The Wilcoxon rank sum test was employed as the statistical method. The size of the dots encodes the percentage of cells within a cluster expressing a particular marker. Color of the dots represents the average expression level throughout all cells within a cluster. **h** Gene ontology (GO)-based GSEA showing normalized enrichment scores (NES) for expression differences of genes comparing BMDM1 compared to BMDM2 on D14 and 21 p.i. An array of statistical tests provided by the fgsea package was employed. Data in (b)–(h) refer to the experiment depicted in (a). Tissue-resident alveolar macrophages (TR-AM), bone marrow-derived macrophages (BMDM), dendritic cell (DC), T lymphocyte (T).

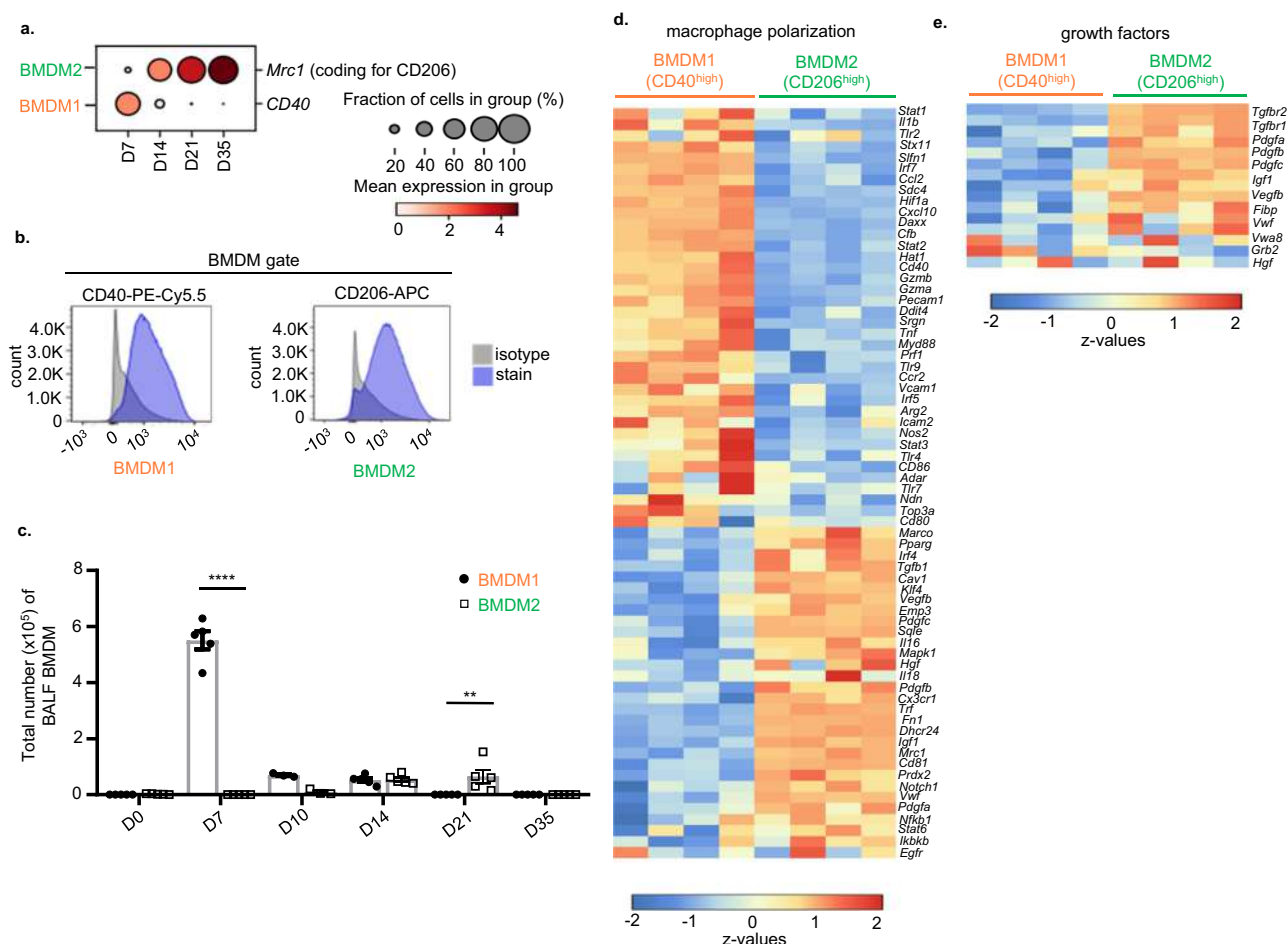


Fig. 2 | CD40 and CD206 expression identify BMDM1 and BMDM2 clusters in the lungs of IAV-infected mice. **a** Dot plot graph showing expression of CD40 and CD206 in BMDM1 and BMDM2, respectively. The size of the dots encodes the percentage of cells within a cluster expressing the particular marker. Color of the dots represents the average expression level throughout all cells within a cluster. Data refer to the scRNA-seq experiment in Fig. 1. **b** Representative FACS histograms displaying CD40 expression in BMDM1 and CD206 expression in BMDM2 collected from BALF of IAV-infected mice on days 7 and 21, respectively. **c** Bar graphs show total BMDM1 and BMDM2 cell counts in BALF samples of mice at the indicated time points. Values are representative of three independent experiments shown as

mean \pm SEM with individual data points for each group with $n = 5$, except for D10 samples where $n = 3$. Probability determined using two-way ANOVA (Holm–Sidak’s multiple comparisons test) **** $p < 0.0001$, ** $p = 0.0043$; for comparison between BMDM1 and BMDM2. **d** Heatmap of DNA microarray profiling depicting genes associated with macrophage polarization phenotypes and **e** with genes associated to epithelial growth factor signaling in CD40^{high} BMDM1 and CD206^{high} BMDM2 flow-sorted from BALF of IAV-infected mice at D7 and D21 p.i., respectively; prior gating of BMDM was performed according to Supplementary Fig. 2a. Source data are provided as a Source Data file. BMDM bone marrow-derived macrophage, BALF bronchoalveolar lavage fluid, D day.

macrophage polarization and TR-AM phenotype; e.g. *Pparg*, *Klf4*, *Pdgfr*, *Fn1*, *Tgfb1*) vs. CD40^{high} BMDM1 (genes associated with an inflammatory phenotype, e.g., *Cxcl10*, *Ccl2*, *Tnfa*, *Il1b*, *Hif1a*). The expression of selected genes indicative of d7 BMDM1 and d21 BMDM2 phenotypes by qPCR (*Cd40*, *Il1b*, *Inos*, *Tnfa* in CD40^{high} d7 BMDM1

versus *Mrc1*, *Arg1*, *Fizz1* and *Tgfb* in CD206^{high} d21 BMDM2; Supplementary Fig. 2d) confirmed the phenotype differences observed in cDNA microarray. When we compared BMDM1/2 expression of the same selected genes on d14, when both BMDM are simultaneously present in the lung, the differences were attenuated, suggesting

transitional phenotypes at that time point (Supplementary Fig. 2d). Of note, we confirmed increased expression of several genes related to epithelial growth factor signaling in CD206^{high} BMDM2 (Fig. 2e). Together, these data suggest that BMDM recruited to the airways undergo a sequential progression through two distinct phenotypes, with defined kinetics, following severe IAV infection. In contrast to CD40^{high} pro-inflammatory BMDM1, transitional CD206^{high} BMDM2 reveal a transcriptional profile associated with tissue regeneration, similar to the TR-AM profile, and are present during the resolution phase of the disease course, contributing to TR-AM pool replenishment.

BMDM2 as opposed to BMDM1 exert proliferative and barrier-protective effects on alveolar epithelial cells in vitro and in vivo

To investigate whether BMDM transition towards BMDM2 endowed the latter with an epithelial-regenerative phenotype, as suggested by the transcriptome analysis, flow-sorted BALF BMDM subsets were co-cultured with ex vivo IAV-infected murine alveolar epithelial cells (AEC). While BMDM1 (collected at d7 p.i.) increased IAV-induced AEC apoptosis, BMDM2 (collected at d21 p.i.) induced AEC proliferation after infection (Fig. 3a, b). To confirm the latter, we used bronchoalveolar lung organoid (BALO) cultures that reveal proximo-distal patterning with branched airways and alveoli allowing modeling of lung development and epithelial cell differentiation (Supplementary Fig. 3a), and profiling of macrophage-epithelial cell interactions³⁶ (experimental setup in Fig. 3c). BMDM2 but not BMDM1 supported the generation of BALO (in terms of numbers and size), suggesting that the presence of BMDM2 promoted epithelial stem cell proliferation and organoid differentiation (Fig. 3d–f). To confirm the robustness of the BMDM2 phenotype outside of its local (inflammation-resolving) microenvironment, we developed a short-term infection model and applied in vivo-generated BMDM2 (vs. BMDM1) by intrapulmonary transfer into IAV-infected *Ccr2*^{-/-} mice lacking BM-monocyte mobilization and BMDMs in inflamed tissues⁸, in an effort to prevent severe injury peaking at D7 (Fig. 3g). BMDM2 were far less injury-promoting than BMDM1 (as quantified by AEC apoptosis; Fig. 3h), and induced proliferation of CD45/31^{neg}EpCam^{low}T1- α ^{neg} alveolar epithelial progenitor cells (AEC II)³⁷, resulting in improved barrier function at D7 p.i. (Fig. 3i, j). We demonstrated previously that lack of BMDM recruitment in *Ccr2*^{-/-} mice per se did not substantially impair IAV clearance (compared to WT)⁸, and we did not detect differences in IAV titers in BMDM1 versus BMDM2-transferred *Ccr2*^{-/-} mice (Supplementary Fig. 3b), suggesting a minor contribution of BMDM of any polarization phenotype to viral clearance. Notably, the tissue-protective features of BMDM2 were conserved in the “experienced” TR-AM (i.e., partially BMDM-replenished) in this model, as opposed to naive, fetal monocyte-derived TR-AM that were sampled before depletion by the infection (Supplementary Fig. 3c–f). Together, these data confirm the alveolar epithelial-regenerative function of transitional BMDM2 (and of experienced TR-AM) implied by their transcriptomic profile in ex vivo and in vivo models, and confirm functional heterogeneity of macrophage subsets identified by scRNA-seq.

Tissue-regenerative macrophage clusters are characterized by expression of *Plet1*

To define putative key regulators of epithelial-regenerative macrophage functions, we compared the top 10 DEGs in the transcriptome data of flow-sorted BMDM subsets. We identified *Plet1* (Placenta-expressed transcript 1), a gene that has been previously associated with wound healing in skin and gut^{20,21} and encoding a protein with a GPI (glycosylphosphatidylinositol) anchor localized to cell membranes²⁰, as the top gene expressed in BMDM2 versus BMDM1 (Fig. 4a). In line with the BMDM2 transitional state towards TR-AM differentiation, *Plet1* has been reported to be a marker gene of TR-AM identity^{34,38}. Correspondingly, we found *Plet1* highly expressed

in the BMDM2 and TR-AM clusters in the scRNA-seq dataset across all time points (Fig. 4b, c), whereas BMDM1 showed low expression. *Plet1* expression was confirmed by qPCR (Fig. 4d) and corresponding cell surface expression was quantified by FACS (Fig. 4e) in D7 BMDM1, D21 BMDM2 and in D21, experienced, TR-AM. As a GPI-anchored membrane protein, *Plet1* can be shed from the cell surface. Quantification of soluble *Plet1* in BALF of IAV-infected WT mice revealed a significant increase starting in the injury phase and peaking at D21 throughout the resolution phase until D35, declining at D60 (Fig. 4f). We next quantified *Plet1* in BALF of *Ccr2*^{-/-} mice at D7 p.i. after adoptive transfer of naive TR-AM, BMDM1, BMDM2 or experienced TR-AMs (Fig. 3g and experimental setup in Supplementary Fig. 3c). In this model where macrophages are exposed to acutely infected/injured lung tissue (from D3 to D7 p.i.), we observed that BMDM2 and experienced TR-AMs are major sources of soluble *Plet1* in BALF (Fig. 4g). These data suggest that *Plet1* surface expression on, or release from, regenerative macrophages was induced by an inflamed or injured alveolar microenvironment. To identify whether a soluble mediator released from the injured AEC during infection was involved, *Plet1*⁺ macrophages were stimulated with IAV-infected versus non-infected AEC conditioned medium. In fact, whereas no *Plet1* could be detected in supernatants of infected and non-infected AEC in the absence of macrophages, conditioned medium of 12 or 24 h infected AEC but not of non-infected AEC significantly increased *Plet1* release by TR-AM compared to baseline, indicating that *Plet1* surface expression and/or secretion/shedding are significantly increased by AEC signals induced by IAV infection (Fig. 4h).

Plet1 induces AEC proliferation and exerts epithelial barrier-stabilizing effects through signaling via MEK and Src kinases

To corroborate our hypothesis that BMDM2-expressed *Plet1* supported AEC (re-)generation, we co-cultured BALO with BMDM2 in the presence of a neutralizing anti-*Plet1* mAb or isotype control (ctl), or without BMDM (Fig. 3c setup). Both organoid numbers and size were significantly increased in the presence of *Plet1*^{high} BMDM2 (ctl), and this effect was abolished with anti-*Plet1* mAb at D7 of culture (Fig. 5a–c) and correspondingly, the alveoli number in fully developed BALO was reduced (Fig. 5d, a). Given that the putative receptor of *Plet1* and its downstream signaling events are unknown, we used recombinant (r) *Plet1*-treated, ex vivo cultured murine AEC for phosphoproteome profiling using a peptide-based kinase activity screen that allows for robust analyses of phospho-tyrosine (PTK) and serine/threonine kinase (STK) activity³⁹ (Supplementary Fig. 5a). Among the most highly regulated kinases, the screen predicted five kinases of the non-receptor tyrosine family Src to have reduced activity, and five kinases to have increased activity, among them STK and CK2a1 with a known role in cell growth/proliferation and suppression of apoptosis⁴⁰, the atypical mitogen-activated protein (MAP) kinase ERK7 and three STKs, a-Raf, b-Raf, and RSK3, all involved in cell growth and survival (Fig. 5e). These data suggest that a Raf-MEK-ERK signaling pathway might be activated in response to r*Plet1* stimulation in AEC II (Fig. 5f). Indeed, we confirmed phosphorylation of c-Raf and ERK1/2 in response to r*Plet1* stimulation in AEC (Supplementary Fig. 5b–d), and an increase in AEC proliferation in absence, but not in presence of the MEK inhibitor U0126 (Fig. 5g).

Given the beneficial effects of *Plet1*^{high} BMDM2 compared to BMDM1 on alveolar barrier function in vivo (Fig. 3i), we next addressed further putative mechanisms of r*Plet1*-mediated improvement of AEC barrier function in the context of IAV injury and analyzed tight junction gene expression. IAV infection of ex vivo cultured murine AEC reduced the mRNA expression of *Tjp-1* (encoding zonula occludens-1, ZO-1), but not of tight junction genes *Cldn1* or *Ocln* (encoding claudin-1 and occludin). Treatment with r*Plet1* increased expression of all three genes compared to non-treated controls (Fig. 5h), and increased

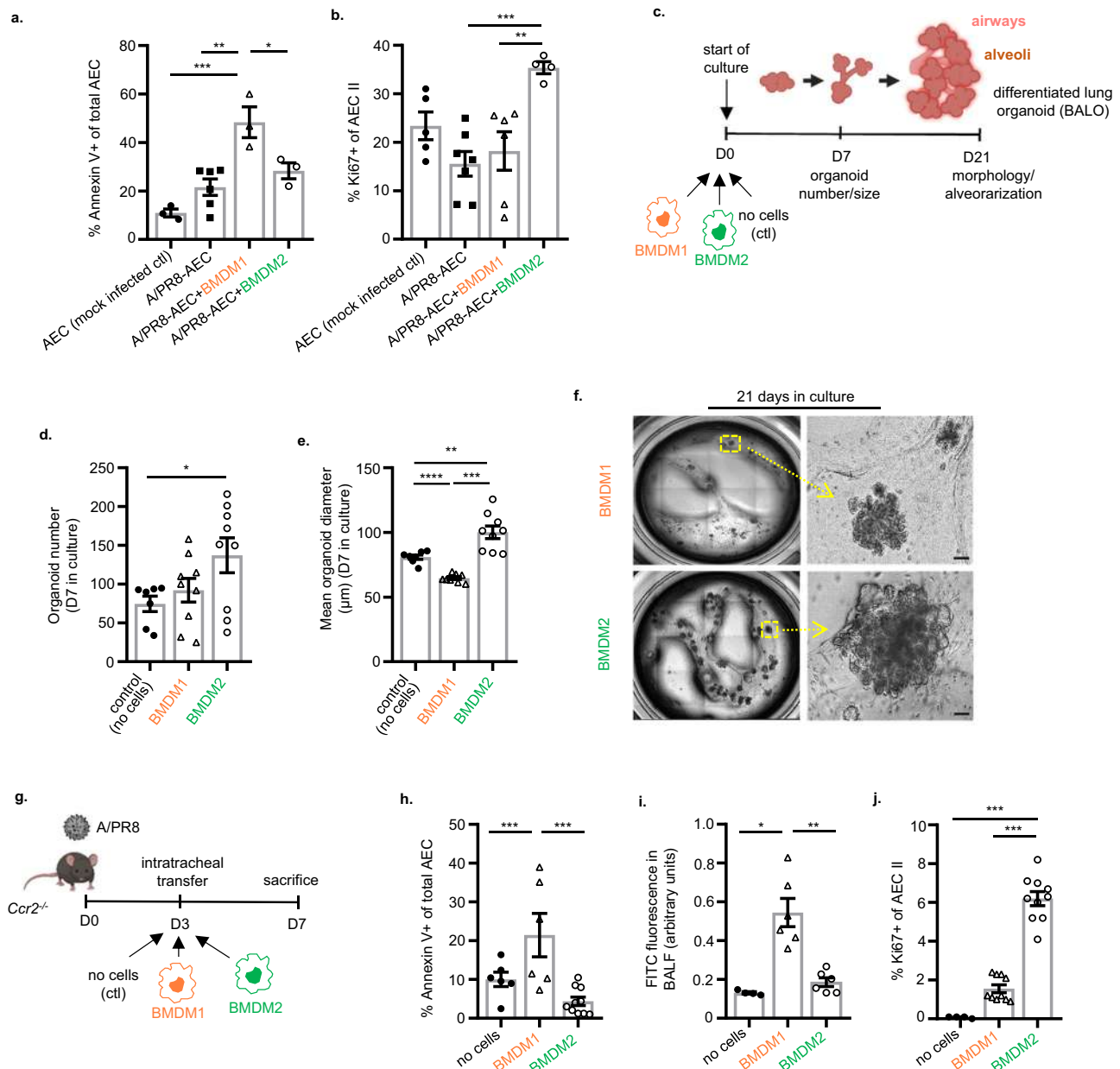


Fig. 3 | BMDM2 as opposed to BMDM1 exert proliferative and barrier-protective effects on alveolar epithelial cells in vitro and in vivo. Bar graphs indicate the percentage of apoptotic (a, Annexin V+) ($p = 0.038$, $p = 0.0023$, $p = 0.0005$), and proliferating (b, Ki67+) ($p = 0.008$, $p = 0.0018$) control ($n = 3$; 5) or IAV-infected ($n = 6$; 7) (24 h) primary murine AECs that were co-cultured with BMDM1 ($n = 3$; 6) or BMDM2 ($n = 3$; 4) (flow-sorted from BALF of infected mice) for further 24 h. c Schematic representation of BALO-BMDM co-culture assay setup. d Quantification of organoid numbers ($p = 0.041$) and e diameter (μm) ($p = 0.0099$, $p = 0.0002$, $p < 0.0001$) of BALO after 7D of co-culture, in control experiments ($n = 7$) (no BMDM) and in co-culture with BMDM1 ($n = 9$) or BMDM2 ($n = 9$). f Representative whole-well picture of organoids after 21D in culture. Images were obtained using EVOS FL microscope. Scale bars indicate 50 μm . g Schematic representation of experimental setup of BMDM intrapulmonary transfer into IAV-infected *Ccr2*^{-/-} mice referring to data in (h)–(j). The figure was created with BioRender. h Percentage of apoptotic AEC (CD31/45^{neg}EpCam⁺Annexin V⁺) analyzed by FACS. Groups: no cells ($n = 6$), BMDM1 ($n = 6$),

BMDM2 ($n = 10$) ($p = 0.049$, $p = 0.0012$). i Assessment of lung barrier permeability by FITC fluorescence in BALF of *Ccr2*^{-/-} recipient mice after intravenous application of FITC-labeled albumin, ratios of BALF to serum fluorescence are given as arbitrary units. Groups: no cells ($n = 4$), BMDM1 ($n = 6$), BMDM2 ($n = 6$) ($p = 0.0079$, $p = 0.0053$). j Percentage of proliferating AEC II (CD31/45^{neg}EpCam⁺T1 α ^{neg}Ki67⁺) analyzed by flow cytometry. BMDM1 and BMDM2 were flow-sorted from BALF of IAV-infected WT mice at D7 and D21, respectively for experiments in (a)–(j). Groups: no cells ($n = 4$), BMDM1 ($n = 10$), BMDM2 ($n = 10$) ($p < 0.0001$, $p = 0.0236$). Bar graphs are representative of three independent experiments showing means \pm SEM and individual data points. Statistical significance was calculated using one-Way ANOVA and Tukey's post-hoc tests except in (d) where Dunnett's post-test was used, and (e), (i) where Brown Forsythe and Welch ANOVA followed by Games–Howell's test was used. In (d) and (e), single data points represent means of organoid numbers and diameters per well. BMDM bone marrow-derived macrophage, ACE alveolar epithelial cell, BALO bronchoalveolar lung organoid, D day. Source data are provided as a Source Data file.

protein levels of ZO-1 as revealed by immunofluorescence (Fig. 5i). Correspondingly, transepithelial resistance of primary murine and human AEC monolayers was significantly impaired by IAV infection, and this was rescued at least in part by rPlet1 treatment (Fig. 5j). In line

with the findings in Fig. 5e, Src kinase Src, Fyn and Lyn (but not Yes) gene expression were downregulated upon rPlet1 stimulation (Supplementary Fig. 5e), and in turn, Src kinase activation abolished the rPlet1-mediated upregulation of TJ gene expression (Fig. 5k). These

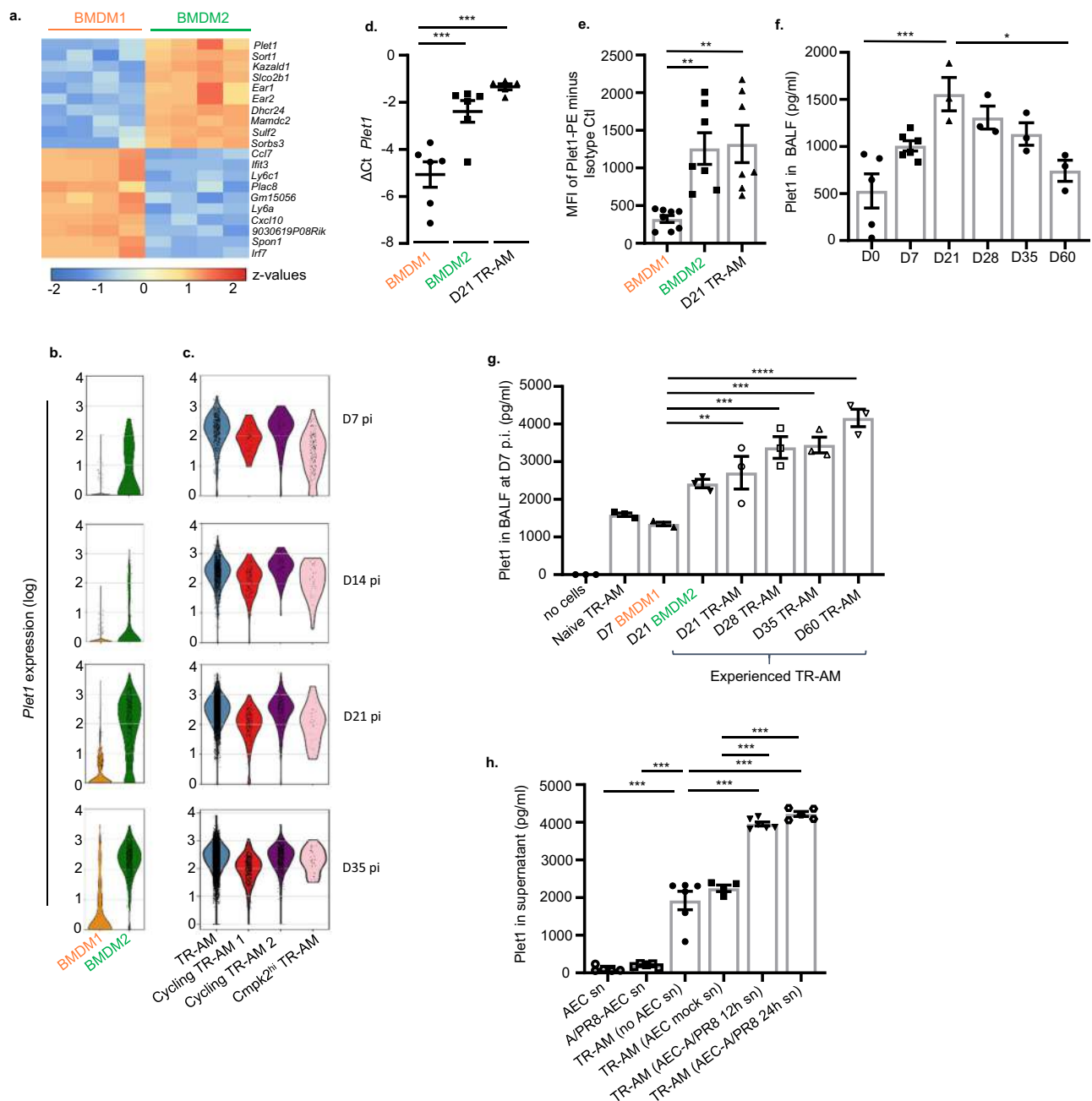


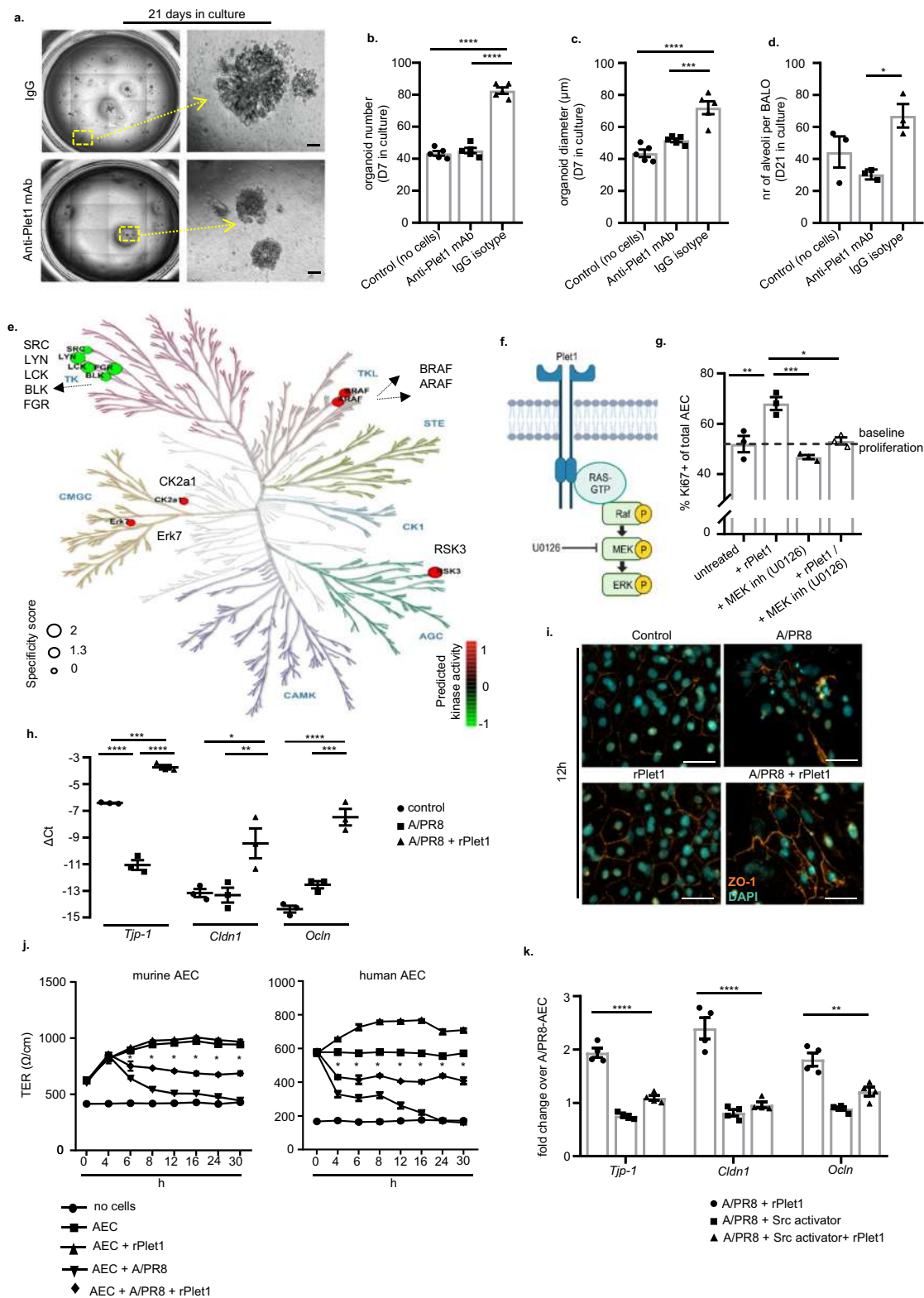
Fig. 4 | BMDM2 and TR-AM are characterized by increased Plet1 expression and release compared to BMDM1. **a** Heatmap of cDNA microarray analysis showing top 10 DEG in BMDM2 versus BMDM1 flow-sorted at D7/D21 p.i., respectively. Genes shown in the heatmap were selected according to p value ($p < 0.05$). **b** Violin plots showing expression level (log) of *Plet1* in BMDM and **c** in TR-AM of IAV-infected mice at D7, D14, D21 and D35. Colored areas indicate density distribution in each cluster. Data refer to scRNA-seq experiments in Fig. 1b. **d** Comparative *Plet1* mRNA expression analysis by qPCR in BMDM1 of IAV-infected mice obtained at D7; in BMDM2 and TR-AM at D21 p.i. Results are expressed as ΔC_t value (Ct reference–Ct target) ($n = 6$) (** $p = 0.0016$, *** $p = 0.0001$). **e** Mean fluorescence intensity (MFI) of Plet1 (PE) analyzed by FACS in BMDM1 (D7 p.i.) ($n = 8$), BMDM2 (D21 p.i.) ($n = 7$) and TR-AM (D21 p.i.) ($n = 7$) from BALF of IAV-infected mice (** $p = 0.0042$, *** $p = 0.0025$). **f** Quantification of soluble Plet1 in BALF of IAV-infected WT mice at

D0/7/21/28/35/60 p.i. $n = 3$ except on D0 where $n = 5$ and D7 where $n = 6$ (* $p = 0.0164$, *** $p = 0.0007$). **g** Quantification of soluble Plet1 in BALF of D7 IAV-infected *Ccr2*^{-/-} mice, adoptively transferred at D3 p.i. with BMDM or TR-AM subsets flow-sorted from BALF of IAV-infected WT mice at the indicated time points ($n = 3$) (** $p = 0.0087$, *** $p = 0.0001$, **** $p < 0.0001$). **h** Plet1 concentration in supernatant of non-infected or infected AEC (24 h) ($n = 5$); in supernatant of BALF-isolated TR-AM treated for 12 h with conditioned medium of non-infected ($n = 4$) or infected AEC (12 h, $n = 6$, and 24 h, $n = 5$) or of untreated TR-AM ($n = 6$) (** $p < 0.0001$). Data are representative of three independent experiments shown as mean \pm SEM statistical differences were calculated using one-way ANOVA and Tukey's post-hoc tests. BMDM bone marrow-derived macrophage, AEC alveolar epithelial cell, BALF bronchoalveolar lavage fluid, TR-AM tissue-resident alveolar macrophage, D day. Source data are provided as a Source Data file.

data indicate that, BMDM2-expressed Plet1 drives AEC proliferation, resulting in alveolarization in lung organoids, and that Plet1 restores alveolar epithelial barrier function after infectious challenge *ex vivo*, effects that we suggest to be mediated via MAPK activation and Src kinase inhibition, respectively.

BMDM2-expressed Plet1 drives alveolar epithelial progenitor cell (AEC II) expansion and protection of lung barrier function in IAV-induced lung injury *in vivo*

We next confirmed that Plet1 is a crucial mediator of the macrophage epithelial cell protective phenotype *in vivo*, focusing on BMDM2 as the



key transitional cell population upregulating *Plet1* during the course of IAV infection. We applied the BMDM2 \rightarrow *Ccr2*^{-/-} mice intrapulmonary transfer model using BMDM2 from *Plet1*^{-/-} mice or BMDM2 pre-incubated with anti-*Plet1* mAb, and analyzed AEC parameters at D7 where we observed the peak of alveolar injury. *Plet1*^{-/-} mice were obtained by generation of *Plet1*^{tdtomato-flox/flox} (termed *Plet1*^{flox/flox}) crossbred with Cre-deleter mice, with loss of *Plet1* mRNA and concomitant loss of tdTomato reporter confirmed in BMDM2 of IAV-

infected *Plet1*^{-/-} mice compared to Cre-negative *Plet1*^{flox/flox} mice (Supplementary Fig. 6a–c). *Plet1* neutralization or knockout in BMDM2 reduced the beneficial effects of BMDM2, resulting in increased AEC apoptosis, reduced expression of tight junction genes in epithelial cells, and alveolar barrier dysfunction, as well as reduced proliferation of AEC II, as compared to controls (Supplementary Fig. 6d–g). Finally, *Ccr2*^{-/-} mice receiving *Plet1*-deficient or *Plet1*-neutralized BMDM2 revealed persistent tissue inflammation compared to controls at D7

Fig. 5 | Soluble Plet1 drives AEC expansion and promotes alveolar epithelial barrier function in ex vivo models. **a** Representative image of BALO co-cultured with BMDM2 for 21D and treated with anti-Plet1 mAb or isotype control. Scale bar represents 50 μ m. **b** Quantification of BALO numbers; single data points represent the mean of organoid numbers per each well ($n = 5$) ($****p < 0.0001$). **c** Mean diameter (μ m) of organoids ($n = 40-87$) per each well, $n = 5$ well/group, after 7D in culture; single data points represent mean diameter of organoids per each well ($****p < 0.0001$, $***p = 0.0006$). **d** average numbers of alveoli per BALO after 21D in culture (control) or co-culture with BMDM2 and anti-Plet1 mAb or isotype control (alveoli were counted from $n = 3$ BALO per group) ($*p = 0.0252$). **e** Predicted kinase activity (5 top phosphorylated, red, and de-phosphorylated kinases, green; shown within phylogenetic kinome tree) in AEC treated with 20 ng/ml rPlet-1 for 12 h. **f** Suggested kinase signaling pathway activated by Plet1. The figure was created with BioRender. **g** Assessment of Ki67 staining in murine primary AEC culture treated with rPlet1 (20 ng/ml) and/or MEK inhibitor U0126 (10 μ M) ($n = 3$) ($*p = 0.0065$, $**p = 0.004$, $***p = 0.0006$). **h** Quantification of tight junction gene expression (*Tjp-1*, *Cldn1*, *Ocln*) by qPCR in murine AEC IAV-infected and treated with rPlet1 (20 ng/ml) ($n = 3$) (*Tjp-1* $***p = 0.0004$, $****p < 0.0001$; *Cldn1* $*p = 0.0282$,

$**p = 0.0236$; *Ocln* $***p = 0.0003$, $****p < 0.0001$). **i** Representative image of ZO-1 localization in AEC monolayers, IAV-infected and/or treated with rPlet1. Scale bar represents 50 μ m. **j** Time course of transepithelial resistance (TER) in murine ($n = 3$) and human AEC ($n = 4$) monolayers on transwells, IAV-infected and/or treated with rPlet1 ($*p < 0.0001$ for the comparison between AECs+A/PR8 and AECs+A/PR8+rPlet1). **k** Quantification of tight junction gene expression (*Tjp-1*, *Cldn1*, *Ocln*) by qPCR in murine AEC IAV-infected and treated with rPlet (20 ng/ml) with/without Src activator (10 μ M). Results are shown as fold change over IAV-infected AEC without rPlet1 ($n = 4$) (*Tjp-1* $****p < 0.0001$; *Cldn1* $****p < 0.0001$; *Ocln* $**p = 0.0024$). Data are representative of three independent experiments showing mean \pm SEM calculated using one-way ANOVA and Tukey's post-hoc tests. **j** represents a single experiment performed with 3 (mouse) or 4 (human) different biological independent samples showing mean \pm SEM and results were analyzed by two-way ANOVA and Tukey's post-hoc test. BMDM bone marrow-derived macrophage, AEC alveolar epithelial cell, BALO bronchoalveolar lung organoid, TER transepithelial resistance, TR-AM tissue-resident alveolar macrophage, D day, inh inhibitor. Source data are provided as a Source Data file.

(Supplementary Fig. 6h). We next generated a conditional (Tamoxifen (Txf)-dependent) BMDM-specific *Plet1*-knockout line by breeding *Plet1^{flx/flx}* mice to *Cx3cr1^{tm2.1(cre/ERT2)luc}* mice (*Cx3cr1^{Cre}-Plet1^{flx/flx}*). Circulating classical monocytes express high levels of *Cx3cr1*, while TR-AM do not^{41,42}. Of note, if *Cx3cr1⁺* monocytes give rise to BMDM and then to TR-AM, these will permanently remain *Plet1*-deficient and tdTomato^{neg} after Cre recombination by Txf administration, even after the expression of endogenous *Cx3cr1* has ceased during differentiation into TR-AM⁴³, allowing genetic targeting of BMDM and BMDM-derived TR-AM. In line, *Cx3cr1^{neg}* (not BMDM-replenished, fetal monocyte-derived) TR-AM of Txf-treated *Cx3cr1^{Cre}-Plet1^{flx/flx}* mice revealed similar levels of *Plet1* mRNA and tdTomato expression as those of Txf-treated *Plet1^{flx/flx}* control mice, whereas BMDM2 (analyzed at D21 p.i.) showed significantly reduced *Plet1* mRNA and tdTomato expression (Supplementary Fig. 6i-l; tdTomato-MFI of C57BL/6 WT TR-AM and D21 BMDM2 depicted for comparison).

We next co-cultured *Cx3cr1^{Cre}-Plet1^{flx/flx}* versus *Plet1^{flx/flx}* BMDM2 flow-sorted at D21 from IAV-infected, Txf-treated mice with BALO as described in Fig. 3c. As expected, loss of *Plet1* in BMDM2 resulted in reduced organoid numbers and growth at D7 and D21 of culture, with reduced BALO complexity and limited alveolarization at D21 (Fig. 6a-d). We next analyzed parameters of persistence of alveolar injury and induction of alveolar repair in Txf-treated *Cx3cr1^{Cre}-Plet1^{flx/flx}* versus *Plet1^{flx/flx}* mice, a process starting around D10 post IAV infection. Lung histopathology reveals that *Plet1^{flx/flx}* mice had widely (D10) or completely (D14, D21) resolved the injury-associated inflammation, whereas dense inflammatory infiltrates were found in *Cx3cr1^{Cre}-Plet1^{flx/flx}* mice with partial resolution until D21 (Fig. 6e). Concomitantly, AEC apoptosis was still significantly increased and AEC II proliferation decreased in *Cx3cr1^{Cre}-Plet1^{flx/flx}* mice at D10 p.i., together with reduced expression of tight junction genes (*Tjp-1*, *Cldn1*, *Ocln*), resulting in higher alveolar barrier leak persisting until D14 p.i. (Fig. 6f-i). Alveolar repair was incomplete in *Cx3cr1^{Cre}-Plet1^{flx/flx}* mice with evidence of disrupted alveoli (Fig. 6j, asterisks, Fig. 6k) and increased thickness of septa (Fig. 6j). Finally, after IAV infection with a virus dose that resulted in low mortality in control mice (Fig. 6l), *Cx3cr1^{Cre}-Plet1^{flx/flx}* mice revealed significantly reduced survival between D10 and D14 p.i., coinciding with BMDM2 appearance in the interstitium and airspaces that confer protection in the *Plet1^{flx/flx}* control mice (according to scRNAseq and FACS data; Figs. 1e and 2c and Supplementary Fig. 2c). *Plet1* was not detected in BALF of Txf-treated *Cx3cr1^{Cre}-Plet1^{flx/flx}* mice compared to *Plet1^{flx/flx}* control mice at D7 and 21 p.i., indicating that BMDM2 (and BMDM2-derived TR-AM) are a major source of *Plet1* in the alveolar compartment (Supplementary Fig. 6m, q). Of note, quantification of cytokines and chemokines, and extent of inflammatory infiltrates revealed that lack of BMDM2-*Plet1* delayed the resolution of the inflammatory responses at d10-14, whereas the level of

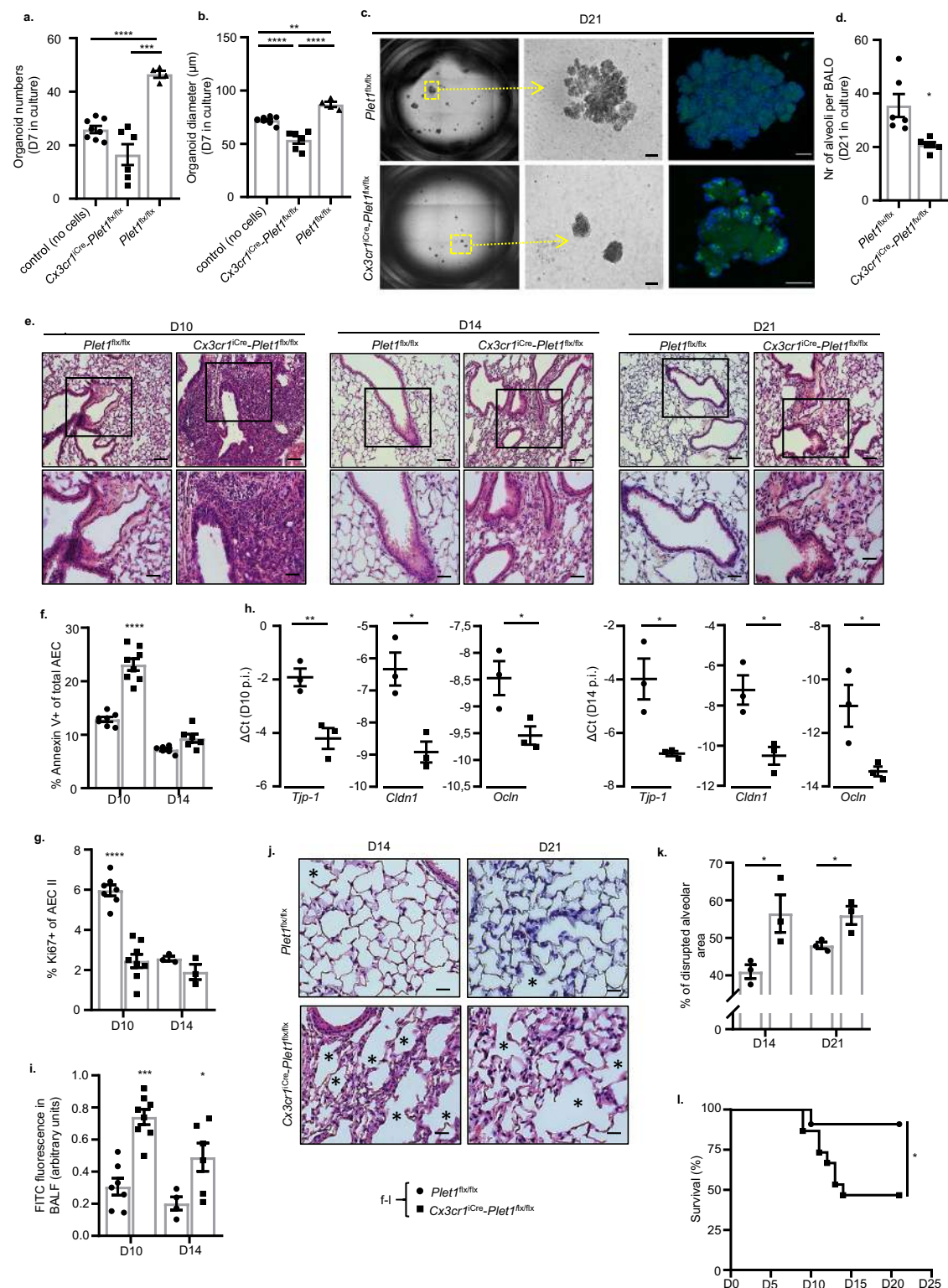
tissue fibrosis was not affected (Supplementary Fig. 6n-p) at the indicated time points. These data indicate that *Plet1* expressed in BMDM2 (and likely, in BMDM-derived TR-AM arising after D14) is crucial for lung tissue recovery and to survive severe viral infection.

Orotracheal administration of rPlet1 rescues mice after lethal IAV infection with therapeutic implications

Treatment of human IAV-infected AEC with rPLET1 resulted in significant improvement of barrier function (Fig. 5j). To verify the putative relevance of PLET1 in the context of human disease, we quantified PLET1 levels in BALF of patients with IAV-induced ARDS compared to a control group of patients with non-inflammatory/non-infectious lung disease (patient characteristics provided in Supplementary Table), and detected high levels in a subset of IAV-ARDS patients (Fig. 7a). To correlate PLET1 levels in IAV-ARDS BALF with the level of alveolar epithelial injury, we additionally quantified total BALF protein as a measure of alveolar barrier dysfunction in both cohorts (Fig. 7b), and PLET1 concentrations negatively correlated with total BALF protein concentrations (Fig. 7c), indicating that soluble PLET1 was present in BALF of patients with IAV-ARDS and might exert similar barrier-protective functions as observed in mice. We next evaluated the therapeutic potential of alveolar administration of rPlet1 in mice at D3 p.i., using an experimental setup (Fig. 7d) aimed to attenuate the peak of lung injury at D7 to D10⁸ in a severe IAV infection model. rPlet1 treatment reduced the injury-associated tissue inflammation, reduced AEC apoptosis, upregulated expression of tight junction genes *Tjp-1* and *Cldn1* together with improvement of alveolar barrier function, and induced substantial AEC II proliferation, indicative of a tissue-protective and -regenerative effect (Fig. 7e-i). Of note, quantification of cytokines (IL-6, KC, MIP1 α , IL10), extent of inflammatory infiltrates and collagen deposition revealed that rPlet1 did not affect inflammatory responses or levels of tissue fibrosis (Supplementary Fig. 7a-c). In addition, viral clearance was not affected by rPlet1 treatment either (Supplementary Fig. 7d). Finally, mice challenged with a lethal dose of IAV were rescued by 85.7% by rPlet1 compared to control treatment (Fig. 7j), suggesting that local administration of rPlet1 may represent a putative treatment strategy in human virus-induced ARDS.

Discussion

Respiratory infections by endemic and emerging viruses pose a major threat to human health as currently evidenced by the COVID-19 pandemic. Lung macrophages have been attributed a crucial role in driving the severity of virus-induced lung tissue injury in IAV^{8,11,44} and COVID-19^{10,45}. Several studies revealed that TR-AM pools are depleted upon viral pneumonia to different extent, depending on viral strain and dose, and are gradually replaced by BMDM during the healing phase, resulting in reprogramming of the TR-AM pool that can either



confer trained immunity, tolerance or resilience to subsequent challenges^{1-3,46-48}. The bone marrow origin of replaced, rather than training of locally persisting TR-AM by pathogen encounter or microenvironmental cues, seem to determine the net functional phenotype of the TR-AM pool at least after viral infections. To date, most of the data relating to macrophage ontology and the resulting phenotype have focused on their contribution to subsequent infections and remain conflicting; however, far less is known about their role in the resolution of inflammation and tissue repair^{3,4,49-51}.

Our data provide evidence that a specific epithelial repair program is induced in alveolar macrophages, via a distinct trajectory of functional BMDM specification from pro-inflammatory/injury-promoting to tissue-healing, with the latter effects mediated by *Plet1*. The BMDM2 *Plet1*-driven epithelial-protective phenotype remained upregulated in replenished, experienced TR-AM for at least 60D p.i., whereas the direct epithelial-proliferative effect declined at 35D p.i. As we could detect *Plet1* expression in TR-AM at D60 p.i., other co-factors may be needed in addition to exert the pro-proliferative effect of *Plet1*.

Fig. 6 | BMDM2-expressed Plet1 drives epithelial progenitor (AEC II) cell expansion and improves lung barrier function in IAV-induced lung injury in vivo. **a** Quantification of BALO numbers after 7D in culture (control) ($n = 8$) or co-culture with BMDM2 derived from Txf-treated control ($Plet1^{flx/flx}$) ($n = 4$) or $Cx3cr1^{Cre}-Plet1^{flx/flx}$ ($n = 6$) mice; single data points represent mean of organoid numbers per each well ($***p = 0.0008$, $****p < 0.0001$). **b** BALO diameter (μm) from the same experiment; single data points represent mean diameter of organoids ($n = 20-49$) per each well. Groups: Control (no cells) ($n = 8$ well); $Plet1^{flx/flx}$ ($n = 4$ well) and $Cx3cr1^{Cre}-Plet1^{flx/flx}$ ($n = 6$ well) ($**p = 0.0026$, $****p < 0.0001$). **c** Representative image of BALO at 21D of culture, stained with LysoTracker® Green DND. The scale bar in the EVOS FL microscope images (middle) represents 50 μm while in confocal images 25 μm (top) and 50 μm (bottom). **d** Average numbers of alveoli per BALO from the experiment in (c); quantified from $n = 6$ BALO/group ($*p = 0.0182$). **e** Lung histological sections of IAV-infected, Txf-treated $Cx3cr1^{Cre}-Plet1^{flx/flx}$ or $Plet1^{flx/flx}$ mice obtained after 10/14/21D p.i., stained with H&E. Images underneath are magnifications of the areas within squares. Scale bars represent 100 μm (top) and 50 μm (bottom). **f** Percentage of Annexin V⁺ AECs in $Plet1^{flx/flx}$ mice at day 10 ($n = 7$) and day 14 ($n = 6$) or $Cx3cr1^{Cre}-Plet1^{flx/flx}$ mice at day 10 ($n = 8$) and day 14 ($n = 6$) ($****p < 0.0001$). **g** Percentage of Ki67⁺ AECs in $Plet1^{flx/flx}$ mice at day 10 ($n = 7$) and day 14 ($n = 3$) or $Cx3cr1^{Cre}-Plet1^{flx/flx}$ mice at day 10 ($n = 8$) and day 14 ($n = 3$) ($****p < 0.0001$). **h** mRNA expression (qPCR) of tight junction component genes in the lung ($n = 3$) (*Tjp1* D10 $**p = 0.01$, D14 $*p = 0.0224$; *Cldn1D10* $*p = 0.013$,

D14 $*p = 0.0185$; *Ocln* D10 $*p = 0.0405$, D14 $*p = 0.0348$). **i** Quantification of barrier dysfunction by FITC-Albumin fluorescence analysis in BALF of $Plet1^{flx/flx}$ mice at day 10 ($n = 7$) and day 14 ($n = 4$) or $Cx3cr1^{Cre}-Plet1^{flx/flx}$ mice at day 10 ($n = 8$) ($****p < 0.0001$) and day 14 ($n = 6$) ($*p = 0.0368$). **f-i** refer to the experiment described in (e). **j** Lung sections of IAV-infected $Plet1^{flx/flx}$ or $Cx3cr1^{Cre}-Plet1^{flx/flx}$ mice obtained at D14/21 p.i., stained with H&E. Scale bars represent 50 μm . Images provide a detailed visualization of specific regions from the corresponding images in 6e (bottom) while maintaining the same magnification as in 6e, bottom. * indicates areas of disrupted, non-repaired alveoli. **k** Quantification of disrupted alveolar area in lung slides of IAV-infected mice. Single data points represent the mean of three randomly chosen areas from each paraffin lung section ($n = 3$ biologically independent mouse lung sections for each group) (D14 $*p = 0.0439$, D21 $*p = 0.0367$). **l** Survival analysis of IAV-infected, Txf-treated $Cx3cr1^{Cre}-Plet1^{flx/flx}$ ($n = 15$) or $Plet1^{flx/flx}$ mice ($n = 11$) ($*p = 0.029$). Data are representative of three independent experiments; bar graphs show means \pm SEM and single data points. Significance was calculated using Brown Forsythe and Welch ANOVA followed by Games-Howell's test on (a) and ANOVA followed by Tukey's post-hoc tests in (b), two-sided Student's *t*-test performed in (d), Welch's correction) (f) (Welch's correction) (g, h, i, k) and Log-rank (Mantel-Cox) test in (l). AEC alveolar epithelial cell, BALO bronchoalveolar lung organoid, BALF bronchoalveolar lavage fluid, D day. Source data are provided as a Source Data file.

at later stages. Also, despite our RNA velocity data on a likely in vivo transition of BMDM1 to BMDM2 phenotype, we cannot exclude that an additional wave of BMDM2 enters the lungs at later stages of the infection course, when repair of the lungs starts to be initiated.

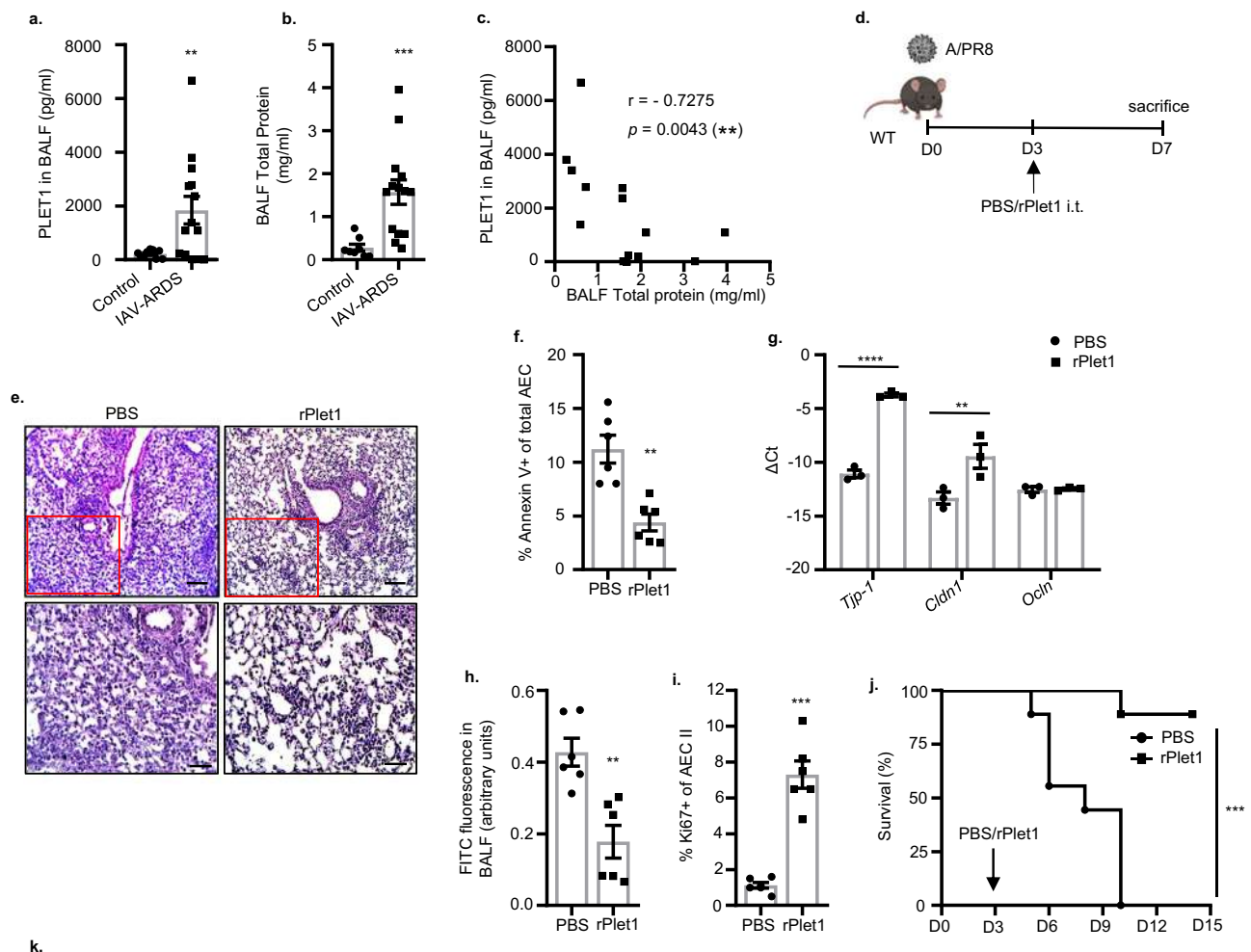
Plet1 is a GPI-anchored membrane protein, mediating epithelial repair responses such as keratinocyte migration in wound healing²⁰ and proliferation of Lgr5⁺ colonic stem cells after injury²¹ in a cell-autonomous manner. It was recently identified as a marker gene for alveolar macrophage specification among tissue-resident macrophages of various organs³⁸; however, no data so far have revealed a role for Plet1 in myeloid cell-mediated tissue repair. At least two different effects were induced by Plet1 in the lung epithelium ex vivo, in organoids, and in vivo, ultimately resulting in the protection of barrier function: First, Plet1 mediated organoid outgrowth from BASC and subsequent alveolarization in BALO, and increased proliferation of AEC II in vivo, indicating its pro-proliferative action on lung epithelial progenitor cells. Furthermore, Plet1 protected AEC from apoptosis, an effect likely associated with the self-renewal program induced³². Proliferation of progenitor cells in different niches of the distal lung is a crucial step in repair after viral lung injury. The alveolar epithelium can be re-established from different local stem/progenitor pools, the most important being Axin2⁺ subsets of AEC II, that via Krt8⁺ intermediates de-differentiate into AEC I to ultimately re-establish alveolar epithelial barrier function. At least in mice, alveolar repair after IAV injury is additionally driven by expansion of bronchoalveolar stem cells, the BALO cells of origin, that de-differentiate into AEC II and further into AEC I^{36,53,54}. In search of a putative signaling mechanism by which Plet1 would drive proliferation of alveolar epithelial cells with regenerative capacity, we identified a MAPK pathway, as MEK inhibition completely abolished Plet1-induced proliferation, suggesting that Raf-MEK-ERK signaling was involved. Similar findings were reported²¹, where Plet1 induced colonic stem cell proliferation via ERK1/2. However, we cannot exclude further mechanisms being involved, e.g. CK2a1 (a further hit in the phosphokinome screen) known to mediate cell survival and proliferation⁵⁵, or others. Ongoing experiments aimed at identification of the Plet1 receptor will likely reveal the full spectrum of Plet1-driven progenitor cell activation.

A second effect elicited by Plet1 was re-establishment of epithelial barrier properties, associated with increased expression of tight junction-associated molecules ZO-1, occludin and claudin-1, the latter previously described to confer sealing properties of tight junctions in airway epithelia⁵⁶. Disruption of the apical junction complex in pulmonary epithelial cells is one of the pathomechanisms driving loss of

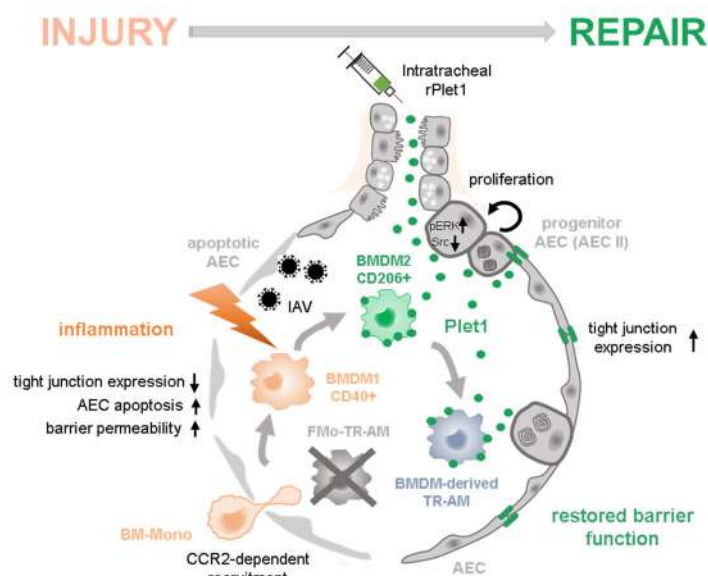
barrier integrity in IAV infection⁵⁷. Therefore, we expected that, in addition to the regenerative program elicited in lung epithelial progenitor cells, induction of tight junction proteins by Plet1 is crucial in both, protection from IAV-induced epithelial barrier disruption, and re-sealing of newly generated AEC. We speculated that this re-sealing program was mediated by pathways distinct from those driving proliferation as it was demonstrated that inhibition of Src kinases prevented inflammation-dependent loss of tight junction proteins in lung epithelial cells⁵⁸. In addition to our own phosphoproteome prediction data showing that Plet1 treatment was associated with reduction of Src kinase activity, treatment with a Src kinase activator abolished these Plet1-induced tight junction protein upregulation. This certainly does not rule out further mechanisms involved, but indicates that, likely, two separate regeneration and repair programs are induced by Plet1 in alveolar epithelial cells, driving proliferation and re-establishment of cell-cell contacts, respectively.

The mechanism by which macrophage Plet1 interacts with the epithelium is an important question to be discussed. We speculate that it might act as a soluble protein, at least in addition to its membrane-expressed form, for several reasons. First, use of recombinant soluble Plet1 instead of Plet1⁺ macrophages reproduced many of the observed effects in vitro and in vivo. In fact, Plet1 can be removed from cells by the addition of Phospholipase C, suggesting that shedding from macrophage surfaces might occur in vivo²⁰. In addition, shedding of Plet1 from the surface of TR-AM occurred in in vitro culture and was significantly increased upon treatment with conditioned medium of infected AEC, indicating that mediators released from IAV-injured AEC, possibly cytokines or danger-associated molecular patterns (DAMPs), were a major signal to increase soluble Plet1 concentrations at sites of infection or injury. Interestingly, naïve, non-replenished TR-AM express Plet1, but did not release high amounts upon transfer into inflamed/injured lungs of IAV-infected *Ccr2*^{-/-} mice, whereas transfer of BMDM2 or experienced TR-AM resulted in highly increased Plet1 BALF concentrations. This could explain why BMDM2/experienced TR-AM transfer, but not naïve TR-AM transfer, protected the lung epithelium of IAV-infected *Ccr2*^{-/-} mice.

TR-AM self-renewal has been pointed out as a major contributor to TR-AM replenishment in lung viral infection, being progressively outcompeted by BMDM-derived TR-AM following IAV infection^{3,59}. Although we cannot fully exclude a contribution of self-renewing fetal monocyte-derived TR-AM to Plet1-mediated repair, this seems unlikely since *Cx3cr1*^{Cre}.*Plet1*^{flx/flx} mice had undetectable levels of Plet1 in BALF. With regard to this transgenic model, the possibility exists



k.



that Plet1 knockout in other *Cx3cr1*-expressing cells might contribute to the outcome of *Cx3cr1^{iCre}-Plet1^{flx/flx}* mice. For instance, interstitial macrophages, DCs and T cells can express *Cx3cr1*; however, we found no significant levels of Plet1 expression in those cell populations in IAV-infected mice by flow cytometry (Supplementary Fig. 6q). Together, our data reveal an innovative mechanism of macrophage-mediated epithelial repair that is key to survive IAV-induced lung injury (Fig. 7k). Independently of the source; it has to be highlighted

that local administration of recombinant Plet1 reproduced the epithelial-protective and -regenerative effects driven by Plet1⁺ macrophage populations, and rescued 85% of mice from fatal influenza. Remarkably, in BALF of a small cohort of patients with IAV-induced ARDS, PLET1 concentrations negatively correlated with a marker of alveolar injury, underscoring Plet1 administration as a putative therapeutic approach in patients with virus-induced lung injury and beyond, that are urgently needed to date.

Fig. 7 | PLET1 is present in patients with human IAV-induced ARDS and rPlet1 administration protects lung epithelial barrier function and rescues mice after lethal IAV infection. **a** Soluble PLET1 and **b** total protein concentration in BALF of patients with IAV-induced ARDS ($n = 14$) or healthy patients ($n = 8$) (patient characteristics provided in Supplementary Table) ($**p = 0.0075$, $***p = 0.0005$). **c** PLET1 concentration was negatively correlated with total protein concentration ($n = 14$). **d** Schematic representation of the experiments conducted in **(e)–(i)**, rPlet1 ($5 \mu\text{g}$; squares) or PBS (circles) were applied intratracheally (i.t.) at D3 p.i. The figure was created with BioRender. **e** Lung histological sections of IAV-infected mice stained with H&E at D7 p.i. Bottom images underneath are magnifications of the top images (red squares); scale bars represent $100 \mu\text{m}$ (top) and $50 \mu\text{m}$ (bottom). **f** Percentage of Annexin V⁺ AECs ($n = 6$) ($**p = 0.0011$). **g** mRNA expression (qPCR) of tight junction component genes in flow-sorted EpCam⁺ cells ($n = 3$) ($*p = 0.0046$, $***p < 0.0001$). **h** Quantification of barrier dysfunction by FITC-Albumin

fluorescence analysis in BALF ($n = 6$) ($**p = 0.002$). **i** Ki67⁺ percentage of AEC II indicating proliferation ($n = 6$) ($***p = 0.0003$). **j** Survival of IAV-infected mice (5×10^2 pfu) treated with PBS or rPlet1 at D3 p.i. ($n = 9/\text{group}$ in two separate experiments) ($***p = 0.0001$). **k** Schematic summary: CD206⁺ BMDM2- and BMDM2-derived TR-AM express Plet1 driving AEC II proliferation and upregulation of tight junction genes, ultimately resulting in AEC barrier repair. Application of exogenous, recombinant Plet1 reproduces these effects, highlighting its therapeutic potential. The figure was created with BioRender. Data are representative of three independent experiments showing mean \pm SEM. Significance was calculated using two-sided Student's t-test on **(a)** (Welch's correction), **(b)** (Welch's correction), **(f, h, i)** (Welch's correction), Spearman's rank correlation test in **(c)**, Log-rank (Mantel–Cox) test in **(j)**, **(g)** two-way ANOVA (followed by Šidák's test). AEC alveolar epithelial cell, BALF bronchoalveolar lavage fluid, D day. Panel **(k)** was generated by BioRender. Source data are provided as a Source Data file.

Methods

Study approvals

Animal experiments were approved by the regional authorities of the State of Hesse (Regierungspräsidium Giessen) and by the Institutional Ethics Committee at the IBioBA Institute. Human lung tissue and BALF samples were obtained from patients who underwent lobectomy or received bronchoscopy for diagnostic reasons after written consent. Use of human lung tissue and BALF samples was approved by the University of Giessen Ethics Committee.

Mice

C57BL/6 and B6.SJL-*Ptprca*^a mice expressing the CD45.1 alloantigen (Ly5.1 PTP) on circulating leukocytes with C57BL/6 genetic background were purchased from Charles River Laboratories. *Ccr2*^{−/−} (B6.129P2-*Ccr2*^{tm1Mae}) mice were generated as described previously and backcrossed to the C57BL/6 background⁶⁰. All mice together with their respective littermate controls were bred under specific pathogen-free conditions and were used between 10 and 14 weeks of age.

Housing conditions for the mice are as follows: light/dark cycle of 4/10 h, temperature maintained at $22 \pm 2^\circ\text{C}$, relative humidity at $55 \pm 10\%$.

Generation of Plet1 transgenic mice

Mice were generated in cooperation with Taconic Biosciences with a tdTomato (tandem dimer tomato red) reporter gene tandemly expressed with a floxed *Plet1* gene on C57BL/6 background to obtain constitutive knock-in of T2A-tdTomato in the *Plet1* locus (Plet1 reporter) with optional conditional knockout of the *Plet1* gene together with the reporter gene. The sequences for the T2A and the open reading frame of tdTomato have been inserted between the last amino acid and the translation termination codon in exon 4, and exon 3 has been flanked by loxP sites. The targeting vector was generated using BAC clones from the C57BL/6J RPCI-23 BAC library and was transfected into C57BL/6N Tac ES cells. The presence of the T2A sequence resulted in the co-translational cleavage between the PLET1 and tdTomato proteins, with co-expression of the Plet1 and tdTomato proteins under the control of the endogenous *Plet1* promoter. Deletion of exon 3 results in the loss of function of the *Plet1* gene by generating a frameshift from exon 2 to exon 4 (premature Stop codon in exon 4). Homozygous *Plet1*^{tdtomato-flox/flox} (abbreviated *Plet1*^{flx/flx}) mice. This line was further crossbred with B6.129P2(C)-*Cx3cr1*^{tm2.1(Cre/ERT2)Jung} mice (Jackson) for the generation of tamoxifen-responsive *Cx3cr1*⁺ (BMDM-specific) *Plet1* conditional knockout mice (abbreviated *Cx3cr1*^{Cre}-*Plet1*^{flx/flx}) by tamoxifen (TXF) feeding. Tamoxifen was administered via chow (Taconic Biosciences, GmbH, 0.4 g/kg) prior to the start of the experiment to target circulating *Cx3cr1*⁺ BMDM precursors (monocytes) before recruitment to the lung (including *Plet1*^{flx/flx} controls when compared to *Cx3cr1*^{Cre}-*Plet1*^{flx/flx} mice, to control for food-/TxF-caused effects). Breeding of *Plet1*^{flx/flx} with Cre-deleter (B6.C-Tg (CMV-

cre)1Cgn/J) mice resulted in ubiquitous, non-conditional loss of the *Plet1* gene (abbreviated *Plet1*^{−/−}).

In vivo infection and treatment protocols

Mice were anesthetized and oro-tracheally inoculated with $2.5\text{--}5 \times 10^2$ pfu/ml (Plaque-forming units per milliliter) of influenza A virus PR8 (A/PR/8/1934(H1N1)) diluted in $70 \mu\text{l}$ sterile PBS^{−/−}. In the treatment approach, $5 \mu\text{g}$ recombinant murine Plet1 (CUSABIO) dissolved in $70 \mu\text{l}$ sterile PBS^{−/−} or PBS^{−/−} alone was applied oro-tracheally to infected mice on D3 p.i. Treated mice were monitored 1–3 \times per day and weighed daily. In survival experiments mice were euthanized when reaching a defined illness score validated for A/PR8 infection and predicting death of the animal within short time. The score included several morbidity criteria (ruffled fur, breathing, movement), and high body weight loss, according to the legal requirements. Euthanized mice were noted as dead in the survival analyses.

Bone marrow (BM) chimeric mice were generated as follows: BM cells were isolated under sterile conditions from the tibias and femurs of wt C57BL/6 donor mice (expressing the CD45.2 alloantigen) as previously described and transferred to CD45.1 alloantigen-expressing recipient mice which had received total body irradiation (6 Gy)³⁰. To assess BM engraftment, the proportion of donor CD45.2-expressing leukocytes in blood, BALF and lung homogenate was analyzed by flow cytometry (FACS). Two weeks after transplantation, regularly $>95\%$ of circulating leukocytes were of donor type (CD45.2), whereas $>95\%$ TR-AM were of recipient type (CD45.1). Chimeric mice were housed under specific pathogen-free conditions for 14 days before PR8 infection.

For pulmonary transfer of macrophages, BMDM or TR-AM were obtained by bronchoalveolar lavage at the indicated time points p.i. from PR8-infected mice of the given genotype. TR-AM were identified by the signature CD45⁺Ly6C^{lo}Ly6G[−]CD11b^{lo}CD11c^{hi}SiglecF^{hi}, BMDM1 and BMDM2 were identified by the signature CD40^{hi}CD206^{lo}CD45⁺Ly6C⁺Ly6G[−]CD11b^{hi}CD11c^{lo}SiglecF[−] and CD40^{lo}CD206^{hi}CD45⁺Ly6C⁺Ly6G[−]CD11b^{hi}CD11c^{lo}SiglecF[−], respectively, and flow-sorted. Cell suspensions were used when the purity was $\geq 95\%$ as ensured by FACS and pappenheim-stained cytopins. $50,000$ cells in $50 \mu\text{l}$ sterile PBS^{−/−} were transferred oro-tracheally to PR8-infected *Ccr2*^{−/−} mice on D3 p.i. For Plet1 neutralization on BMDM2, cells were incubated for 10 min at 4°C with anti-Plet1 antibody (R&D Systems) or recommended IgG isotype control, washed, and transferred directly thereafter.

Flow cytometry and cell sorting

Cells ($1\text{--}5 \times 10^5$) derived from bronchoalveolar lavage or from lavaged, perfused, and homogenized murine lungs were resuspended in FACS buffer (PBS^{−/−}, 10% FBS, 0.1% NaN₃), preincubated with Fc block for 5 min and stained with fluorochrome-conjugated antibodies for 30 min at 4°C . For Annexin V staining, cells were resuspended in Annexin V staining buffer (10 mM HEPES, 140 mM

NaCl, and 2.5 mM CaCl₂). The fluorochrome-labeled antibodies used for FACS analysis of macrophage subsets/phenotypes, Plet1 expression, AEC proliferation and apoptosis are CD326 (Epcam) (APC-Cy7, clone G8.8, Cat No 118218 BioLegend) (1/100), CD24 (PE-Cy7, clone M1/69, BioLegend, Cat No 101821) (1/100), CD31 (Alexa Fluor 488 clone MEC13.3, BioLegend, Cat No 102513, or Pacific blue clone 390, BioLegend, Cat No 102413) (1/50), CD45 (FITC Clone 30-F11 BioLegend, Cat No 103107, APC-Cy7 30-F11 BioLegend, Cat No 103115, or Pacific blue, clone 30-F11 BioLegend, Cat No 103125) (1/100), T1α/podoplanin (APC, clone 8.1.1 BioLegend, Cat No 127409) (1/20), Ki67 (FITC clone 16A8 BioLegend, Cat No 652409 or BV605, clone 16A8, BioLegend, Cat No 652413; PE, clone 16A8, BioLegend, Cat No 652403) (1/50), and corresponding isotype control FITC Rat IgG2a, κ Isotype Ctrl Antibody (clone RTK2758, BioLegend, Cat No 400505, 1/50), Brilliant Violet 605™ Rat IgG2a, κ Isotype Ctrl Antibody (clone RTK2758, BioLegend, Cat No 400539, 1/50), PE Rat IgG2a, κ Isotype Ctrl Antibody (clone RTK2758, BioLegend, Cat No 400508, 1/50), Annexin V (Alexa Fluor 647, clone 640907 Invitrogen, Cat No A23204, PE, clone 640907, Invitrogen, Cat No A35111) (1/20), GR-1 (PE-Cy7 clone RB6-8C5, BioLegend, Cat No 108415, or PerCP, clone RB6-8C5, BioLegend, Cat No 108425) (1/100), Ly6G (APC clone 1A8 BioLegend, Cat No 127617, or PE-Cy7, clone 1A8, BioLegend, Cat No 127613) (1/50), Ly6C (FITC, clone AL-21 BD Biosciences, Cat No 553104) (1/20), Siglec-F (PE clone E50-2440, BD Biosciences, Cat No 562068 or BV421, clone E50-2440, BD Biosciences, Cat No 562681) (1/50), CD11c (PerCP-Cy5.5, clone N418, BioLegend, Cat No 117327) (1/20), CD11b (V500 clone M1/70 BD Biosciences, Cat No 532127 or Pacific blue, clone M1/70, BD Biosciences, Cat No 532681) (1/50), MERTK (FITC, clone 2B10C42, BioLegend, Cat No 151503) (1/50), CD64 (PE, clone X54-5/7.1, BioLegend, Cat No 139303) (1/20), MHC II (FITC clone AF6-120.1, BD Biosciences, Cat No 562011 or PE-CF594, clone AF6-120.1, BD Biosciences, Cat No 562824) (1/50), CD45.1 (FITC, clone A20, BioLegend, Cat No 110705) (1/50), CD45.2 (APC-Cy7, clone 104, BioLegend, Cat No 109823) (1/50), CD206 (APC, clone C068C2, BioLegend, Cat No 141707) (1/20), CD40 (PE-Cy5, clone 3/23, BioLegend, Cat No 124617) (1/20). Rat IgG2a, κ Isotype Ctrl Antibody (APC, Clone RTK2758, BioLegend, Cat No 400511) (1/20), Rat IgG2a, κ Isotype Ctrl Antibody (PE-Cy5, Clone RTK2758, BioLegend, Cat No 400509) (1/20). Cells were routinely stained with 7-AAD (BioLegend Cat No 420403) (1/100) or Sytox (Thermo Fisher Scientific, Cat No S34862) (1/1000) for dead cell exclusion. All fluorochrome-labeled antibodies were from BioLegend unless otherwise mentioned. FACS analyses were performed using a BD LSRFortessa flow cytometer (BD Biosciences) and cell sorting was performed on a BD ARIAIII. The purities of sorted cells were ≥90% in all sorted samples. Data were analyzed using FACS Diva and FlowJo software packages. The list of antibodies in Excel format including clone, company name, Cat No and the concentration used, is provided as Supplementary Data 1.

Isolation of primary murine alveolar epithelial cells (AEC)

Lung homogenates were obtained by instillation of dispase (BD Biosciences) through the trachea into HBSS (Gibco) perfused lungs, followed by incubation (in dispase) for 40 min as previously described⁶¹. After removal of the trachea and proximal bronchial tree, the lungs were homogenized (GentleMACS, MACS Miltenyi Biotech) in DMEM/2.5% HEPES with 0.01% DNase (Serva) and filtered through 100 and 40 μm nylon filters. Cell suspensions were incubated with biotinylated rat anti-mouse CD45 (Clone 30-F11, BD, Cat No 553078), CD16/32 (clone 2.4G2, BD, Cat No 553143) and CD31 (clone MEC13.3, BD, Cat No 553371) mAbs for 30 min at 37 °C followed by incubation with biotin-binding magnetic beads and magnetic separation to deplete leukocytes and endothelial cells prior to further culture. AEC suspensions with a purity ≥90% as determined by FACS were seeded at a

density of 120–150,000 cells/cm² in 4-μm-pore size transwells (Corning Inc.), in 24-well plates at a density of 250,000 cells/cm², or in chamber slides (Corning Inc.), and cultured in DMEM enriched with HEPES, L-Glutamine, FCS, and pen/strep. The list of antibodies in Excel format including clone, company name, Cat No is provided as Supplementary Data 1.

AEC apoptosis

The AEC pellet was resuspended in 10 μl of FC block solution, and after 15 min, Annexin V antibody (Alexa Fluor 647, BioLegend 1:20) diluted in 100 μl Annexin V buffer was added (BioLegend, Cat No 640922). The samples were incubated for 15–25 min at 4 °C. All stained cell suspensions were filtered in 5 ml polystyrene tubes and analyzed by a BD LSRFortessa™ flow cytometer to quantify the proportion of apoptotic AEC.

AEC proliferation

The AEC pellet was resuspended in 150 μl of diluted permeabilization/fixation buffer (eBioscience™) and incubated for 30 min at RT. 100 μl of permeabilization/wash buffer (eBioscience™) was added after the incubation period and the cell suspension was centrifuged at 1000 g for 5 min at 4 °C. The supernatant was discarded and 50 μl of Ki67 antibody (11F6, PE, BioLegend) diluted 1:50 in permeabilization/wash buffer was added to each sample for 1 h incubation, in the dark, at 4 °C. After staining, the cells were washed with permeabilization/wash buffer and centrifuged at 1000 g for 5 min. The cell pellet was resuspended in 200 μl of sorting buffer and proliferation was quantified.

Alveolar leakage measurement

Alveolar barrier leakage was assessed by i.v. injection of 100 μl FITC-labeled albumin (Sigma-Aldrich) and quantification of FITC fluorescence ratios in BALF and serum (diluted 1:100) with a fluorescence reader (FLX 800, Bio-Tek instruments) as described previously⁸, and given as arbitrary units (AU).

Isolation of primary human AEC

Primary human AEC were isolated as described previously³⁰. Briefly, the lung was cut into small pieces and washed with HAM's F12 + 10% FCS + 1% Pen/Strep/Amphotericin. Tissue was incubated in dispase overnight and thereafter at 37 °C with gentle rotation for 3 h. The tissue was homogenized in MACS dissociater (GentleMACS, MACS Miltenyi Biotech) and the supernatant filtered through 100, 40 and 20 μm nylon filters. Cell suspension was centrifuged and the pellet was resuspended in DNase-containing medium. As a density gradient media, ficoll was overlaid with 15 ml cell suspension and, afterwards, centrifuged and the interphase was taken out and put into DNase-containing medium. Followed by a centrifugation step and thereafter the pellet was resuspended in cell culture medium. Cell viability was assessed by using Trypan Blue staining. Approximately 3.0 × 10⁵ AEC (purity ≥90% determined by FACS) were seeded in 24-well inserts with 0.4 μm pore size, and kept in HAM's F12 medium (Biochrom, Berlin, Germany) supplemented with 10% FCS, Pen/Strep and Amphotericin for 7–10 days until confluency. AEC with a purity ≥90% determined by FACS (Epcam⁺ CD45/CD31^{neg}) were used for further analyses.

AEC in vitro assays

Primary murine and human AEC were infected with PR/8 at MOI 0.5, as described previously¹¹. A/PR8 was diluted in PBS⁻ containing BSA and was added to the cells for 1 h, until the inoculum was removed and changed to infection medium (DMEM supplemented with BSA, pen/strep, L-Glutamine and trypsin) for further incubation. For co-culture experiments, AEC were seeded first, allowed to reach confluence, and were infected with A/PR8 or mock infected. 24 h p.i., BMDM were flow-sorted from the BALF of A/PR8-infected mice (BMDM1 were sorted at D7 p.i., BMDM2 were sorted at D21 p.i.) and added directly to the

monolayer for 24 h. Cells were stained with Annexin V for apoptosis and Ki67 for proliferation assays and quantified by FACS. For western blot analysis, murine AEC were cultured in medium DMEM supplemented with pen/strep, L-glutamine and 10% heat-inactivated FCS. Cells were incubated at 37 °C for 5 days and thereafter treated with rPLET1 (40 ng/ml) for 12 h. Cell lysates were prepared in the same manner, as those used for the kinase activity assay described below. For the proliferation assays, murine AEC were cultured in DMEM enriched with pen/strep, L-glutamine and 2% FCS. Cells were incubated at 37 °C for 4 days and thereafter treated with rPLET1 (40 ng/ml) and/or MEK inhibitor U0126 (Promega, #V1121, 10 μ M) for 12 h. For qPCR analysis, murine AEC were cultured in DMEM, pen/strep, L-glutamine and 10% FCS, after reaching the confluence they were infected with PR/8 at MOI 0.5, as described previously¹¹ and treated with rPlet1 (20–40 ng/ml) and/or Src activator (Santa Cruz Biotechnology, Cat No #sc-3052, 10 μ M) for 12 h. Cells were stored RLT buffer and stored in –80 °C for further qPCR analyses. For qPCR analyses of Src family-related genes, murine AEC were cultured as described above and treated with rPlet1 for 1 and 2 h. Cells were taken into RLT buffer and stored in –80 °C for qPCR analysis. In the stimulation assay of TR-AM with the AEC supernatant, AEC were cultured as mentioned above. When the cells reached confluence, they were infected with PR/8 at MOI 2.0 or mock infected, as described above and incubated at 37 °C for 12 h/24 h. The supernatant of these cells was used to stimulate the TR-AM (300,000 cells/cm² in a 24-well plate, seeded in RPMI medium supplemented with pen/strep, L-glutamine, 2% FCS and 2.5% HEPES, 6 h prior to the treatment) for 12 h. The supernatant of TR-AM cultures was used for soluble Plet1 quantification by ELISA.

Quantitative real-time polymerase chain reaction (qRT-PCR)

Cells were centrifuged at 1400 rpm for 10 min at 4 °C and pellets were resuspended in 350 μ l of RLT buffer and stored at –80 °C for RNA isolation. RNA was isolated using RNeasy Kit (QIAGEN) and cDNA synthesized. Quantitative PCR (qPCR) was performed with SYBR green I (Invitrogen) in the AB StepOnePlus Detection System (Applied Bioscience) using the reaction setup provided by the manufacturer's instructions. The following murine primers were used: *β -actin* (FP 5'-ACCCTAAGGCCAACCGTGA-3'; RP 5'-CAGAGGCATACAGGGACAGCA-3'); *Gapdh* (FP 5'-TCCCACTCTTCCACCTTCGA-3'; RP 5'-AGTTGGGATAGGGCTCTCTT-3'); *Hprt* (FP 5'-ACAGGCCAGACTTTGTTGGAT-3'; RP 5'-ACTTGGCTCATCTTAGGCTT-3'); *Tgfb1* (FP 5'-CCACCTGCAAGACCATCGAC-3'; RP 5'-CTGGCGAGCCTTAGTTTGGAC-3'); *Fizz1* (FP 5'-TCCTGCCCTGTGGGATGAC-3'; RP 5'-GGCAGTGGTCCAGTCAACGA-3'); *Il1b* (FP 5'-TACCTGTGGCTTGGGCTCAA-3'; RP 5'-GCTTGGGATCCACTCTCCAGCT-3'); *Inos* (FP 5'-TTGGAGGCCTGTGTGAGCCC-3'; RP 5'-AAGGCAGCGGCACATGCAA-3'); *Arg1* (FP 5'-ACCACAGTCTGGCAGTTGGAAGC-3'; RP 5'-AGAGCTGGTGTGAGGGAGTGT-3'); *Tnfa* (FP 5'-CGGTCCCAAAGGGATGAGAAGT-3'; RP 5'-ACGACGTGGGCTACAGGCTT-3'); *Mrc1* (FP 5'-GGGACGTTTCGGTGGACTGTG-3'; RP 5'-CCGCCTTTCGCTGCGCATGT-3'); *Cd40* (FP 5'-GTTTAAAGTCCCGGATGGA-3'; RP 5'-CTCAAGGCTATGCTGTCTGT-3'); *Cldn1* (FP 5'-CGACATTAGTGGCCACAGCA-3'; RP 5'-TGGCCAAATTCATACCTGCA-3'); *Tjp1* (FP 5'-GCTTCTCTGTGTCGGCCCTAA-3'; RP 5'-GGGAGCCTGTAGACGTTTTT-3'); *Ocln* (FP 5'-TCTTTCCTTAGGCGACAGC-3'; RP 5'-AGATAAGCGAACCTGCCGAG-3'); *Plet1* (FP 5'-TCCTCATCGTCGTAATCGC-3'; RP 5'-TGAGGCTGAGGGTTGTAAGTGT-3'); *Yes* (FP 5'-TGAGGCTGCTGTATGGTC-3'; RP 5'-GCATTCTGTATCCCCGCTCT-3'); *Lyn* (FP 5'-TGGCTAAGGGTAGTTTGCTGG-3'; RP 5'-CGCAGATCACGGTGGATGTA-3'); *Src* (FP 5'-GCCTCACTACCGTATGTCC-3'; RP 5'-TTTGTATGGCAACCCTCGTG-3'); *Fyn* (FP 5'-AAGCACGGACGGAAGATGAC-3'; RP 5'-ATGGAGTCACTGGAGCCAC-3'). *β -actin* and *Gapdh* expression served as normalization control. The data are calculated as $\Delta C_t = (C_t^{\text{reference}} - C_t^{\text{target}})$ and given as ΔC_t (larger ΔC_t values indicate a higher normalized expression of the target gene) or fold induction of

control ($2^{\Delta\Delta C_t}$). The list of primers in Excel format including sequences, Oligo ID and the company name is provided as Supplementary Data 2.

Transcriptome analysis by whole-genome microarray

For microarray analysis, different subsets of macrophages at different time points p.i., were sorted as described above. The sorted BMDM1 and BMDM2 were resuspended in 300 μ l RLT buffer and stored at –80 °C until RNA isolation and further processing. The isolated RNA was amplified and labeled using the LIRAK kit (Agilent) following the kit instructions. Per reaction, 200 ng of total RNA was used. 2 μ g labeled cDNA was hybridized on SurePrint G3 Mouse GE 8 \times 60 K Microarrays (Agilent, Design ID 028005) following the Agilent protocol. Washed slides were dried with acetonitrile, treated with Agilent dye-stabilization solution and scanned at a resolution of 2 μ m/pixel with an InnoScan 900 instrument. Image analysis was done with Mapix 6.5.0. Further data analysis was done using R 3.6.1 (R Core Team, R, <https://www.R-project.org/2015>) and the limma package⁶² from BioConductor. Mean spot signals were quantile-normalized. Log-signals of replicate spots were averaged.

Single-cell capture and library preparation

Following the 10xGenomics library preparation protocol, all samples were sequenced on an Illumina NovaSeq6000 sequencer. We used demultiplexing and the subsequent FASTQ file generation Illumina bcl2fastq (2.19.0.316) to generate the library. Sequencing reads were aligned to the mouse mm10 reference genome (refdata-gex-mm10-2020-A downloaded from 10xGenomics) using STAR solo (2.7.9a) resulting in a UMI count matrix where cells (barcodes) are columns and rows are genes. During the alignment step UMI deduplication was performed by STAR, as well. STAR was run in Velocity mode in order to allow for downstream velocity analysis. Droplet filtering was done using the EmptyDrops_CR parameter setting.

Analyses of single-cell RNA-seq data

Resulting UMI count matrices were pre-processed for further analyses using Scanpy (1.7.2) in a Python (3.8.10) environment⁶³. We used scrublet with standard parameters in order to identify the doublets. Overall, 77 doublets were found, evenly distributed across the data; therefore, we did not discard these cells (please see https://github.com/agbartkuhn/Pervizaj-Oruqaj-Plet1_sc_analysis for detailed parameter settings). In order to filter out low-quality cells, doublets, cell debris or ambient RNA the following filter criteria were applied to the data. Cells contain a maximum of 40,000 and a minimum of 1500 UMI counts. Less than 15% of all UMI counts are allowed to map to a mitochondrial origin. Finally, at least 2000 different genes must be detectable (at least one read mapped to the gene) for each cell. In order to reduce the gene set, only those genes were kept, which were expressed in at least 20 cells. UMI counts underwent normalization in respect to the library size and such that each cell contains 10,000 reads. The resulting counts were log transformed. For dimensionality reduction and for data integration with Harmony PCAs were calculated. The data integration with Harmony finished after 3 iterations. A k-nearest-neighbor approach was applied to calculate a neighborhood graph, on which Leiden clustering was performed with resolutions of 0.4, 0.6, 1.0 and 1.4. For further analysis, the Leiden clustered cells with a resolution of 1.4 were used. A two-dimensional visualization of the cells was achieved by calculating UMAPs. Next, automatic cell-type annotation was performed by calculating the average gene expression of all clusters individually. Data was compared to the Mouse Cell Atlas (MCA)⁶⁴ using the scMCA R package (<https://github.com/ggijlab/scMCA>). All clusters belonging to the large central aggregate of cell were annotated as alveolar macrophages and subsequently merged into a single cluster. Differentially expressed genes were identified by the Scanpy rank_gene_groups function. Velocity analysis was done

using scVeloc⁶⁵. Gene set enrichment analysis was done using clusterProfiler⁶⁶ and fgsea packages in R (R Core Team, 2021) using GO and KEGG annotations. For estimation of connectivity between cell clusters, PAGA (partition-based graph abstraction) algorithm was calculated in order to determine BMDM-to-TR-AM transition using the PAGA function as part of the scVeloc package using default settings. Standard settings were applied as described in <https://scvelo.readthedocs.io/en/stable/VelocityEngine/> (please see https://github.com/agbartkuhn/Pervizaj-Oruqaj_Plet1_sc_analysis, for detailed parameter settings).

Lung organoid experiments

Bronchoalveolar lung organoids (BALO) were generated from flow-sorted murine lung epithelial stem cells co-cultured with flow-sorted mesenchymal cells as previously described³⁶. In lung organoid cultures, 3×10^5 WT BMDM (1 or 2) or 4×10^5 BMDM2 from *Plet1^{flx/flx}* or *CX3CR1^{Cre}-Plet1^{flx/flx}* and organoids were cultured in Matrigel® (Corning) (α MEM, 10% FCS, 100 U/ml penicillin, 0.1 mg/ml streptomycin, 2 mM L-glutamine, $1 \times$ insulin/transferrin/selenium, 0.0002% heparin)³⁷. In selected experiments, anti-Plet1 Ab (20 ng/ml) or isotype control (20 ng/ml) was added to the organoid medium upon cell seeding. BALO numbers and size were analyzed manually, by light microscopy with an EVOS FL imaging system (Thermo Fisher Scientific) and data are provided as means per each well with single data points representing one well.

Foci forming assay

For virus quantification, MDCK II cells were seeded in 96-well plates and dilutions for FFU (foci forming unit) (equivalent to plaque-forming units. PFU) quantification were prepared in duplicates from 10^{-1} to 10^{-8} in PBS/0.2% BSA. Cells were washed once with PBS and infected with 50 μ l of virus dilutions. Cells were incubated at 37 °C and 5% CO₂ for 45 min, inoculum was removed and cells were covered with 100 μ l Avicel medium (2 \times MEM, 1% Penicillin/Streptomycin, 0.1% NaHCO₃, 0.2% BSA, 2 μ g/ml Trypsin-TPCK, 1.25% Avicel). Cells were incubated for 30 h at 37 °C and 5% CO₂, washed twice, fixed and permeabilized in 4% PFA containing 1% Triton-X-100 for 30 min at RT. Cells were washed with washing buffer (PBS and 0.05% Tween-20) and incubated with 50 μ l of primary anti-NP (nucleoprotein) antibody solution (3% (w/v) BSA in PBS^{+/+}) for 2 h at RT. After further washing steps, cells were incubated with 50 μ l of Horse-Radish Peroxidase (HRP) labeled anti-mouse secondary antibody at RT for 1 h, washed again and plates were left to air-dry and scanned, using the Methods 29 Epson Perfection V500 Photo scan (Epson) at 1200 dpi. The virus titer was calculated according to the dilution factor and is expressed as pfu per milliliter (pfu/ml).

PLET1 enzyme-linked immunosorbent assay

BAL fluid (BALF) from mice or from IAV-ARDS versus control patients was concentrated using Pierce™ Protein Concentrator PES, 3 K MWCO, 2–6 ml (Thermo Scientific™) and analyzed by commercial PLET1 ELISA (mouse PLET1: Antibody research corporation, USA, human PLET1: MyBioSource, USA) according to the manufacturer's instructions. The absorbance was quantified at 450 nm wavelength in the microplate reader (iMark™, Bio-Rad). Human BALF protein concentration was quantified using Quick Start™ Bradford Protein Assay Kit 2 (#5000202, Bio-Rad), absorbance was quantified at 595 nm wavelength in the microplate reader (iMark™, Bio-Rad).

Histology and immunofluorescence

Lungs were clipped at the trachea before opening of the chest cavity, then perfused with 4% paraformaldehyde (PFA), removed, and then fixed for 24 h in 4% PFA. Lungs were embedded in Paraffin (Leica ASP200S), cut into 5- μ m-thick sections, and stained with hematoxylin and eosin (Merck). Images of paraffin lung sections with H&E staining

were quantified using Fiji/ImageJ as follows: from each image, three different regions of interest (ROIs) avoiding bronchial and peri-bronchial regions, were marked. For quantification of alveolar area of each ROI, we measured the total area and upon thresholding (using the built-in Huang segmentation algorithm) the area that is occupied by lung tissue. The % of alveolar space is calculated with the following formula: (ROI_Total_Area - ROI_Tissue_Area)*100 / ROI_Total_Area.

For the analysis of fibrosis, lung sections were stained by Mason's trichrome and the bright field images acquired with the EVOS microscope were corrected for their white balance. Subsequently, for these images, we used a custom-made macro (<https://doi.org/10.5281/zenodo.10135192>) to perform pixel classification using a pre-trained Ilastik⁶⁴ model. This pre-trained model (also available online) classifies all pixels of the input image into 6 different classes (background, non-lung tissue, infiltrative area, regenerative area, connective tissue and healthy tissue). The custom-made macro, opens the bright field images, calls the pixel classification module of Ilastik and then pulls back the classified image. Using the six different intensities of the six classes quantifies the % of each class in relation to the total area of the lung tissue. The macro saves the classified images as well as a tab-separated file with all quantifications from all analyzed images.

For immunofluorescence microscopy, isolated AEC cultured in chamber slides (Nunc) were infected with 0.5 MOI PR8 or mock infected and treated with rPLET1 (CUSABIO, 20 ng/mL in medium) or left untreated. After 12 h of incubation at 37 °C, 5% CO₂, the slides were fixed in a 1:1 ratio of cold acetone/methanol for 5 min and blocked with 3% BSA in PBS for 30 min at 4 °C prior to staining. The cells were stained with Alexa Fluor® 594 conjugate ZO-1 antibody (Clone ZO1-1A12; Invitrogen) or mouse PE-IgG1, k isotype control (Clone P3.6.2.8.1; eBioscience™) diluted in PBS^{+/+}, 0.1% BSA, 0.2% Triton-X-100 for 2 h, followed by washing and mounting with DAPI containing mounting medium (Vectashield, Vector Labs). For organoid staining, cultures were fixed with 4% PFA for 15 min at RT, washed with PBS^{+/+} and stained with LipidTOX™ neutral lipid staining solution (Thermo Scientific) for 6 h at RT to visualize alveoli. Cultures were washed with PBS^{+/+}, co-stained with DAPI and mounted for imaging. Confocal images of organoids were acquired either with a Leica SP5 (software version LAS AF 2.7.3) or a Leica SP8 (software version LAS X 3.5.7) confocal microscope. For the quantification of the organoids (area, diameter and alveoli number), we delineated manually each organoid using Fiji and we also marked manually every alveolus on each confocal z-stack acquired for each organoid.

Transepithelial resistance

Transepithelial resistance (TER) in murine and human AEC was quantified by a Millicell-ERS2 device. Cells were seeded on 0.4 μ m pore size transwells and cultured until achieving electrochemical resistances of $\geq 600 \Omega / \text{cm}^2$ in murine and $\geq 400 \Omega / \text{cm}^2$ in human AEC. Cells were infected with PR8 at MOI 0.5 or mock infected for 1 h at 37 °C and then supplied with recombinant murine (20 ng/ml) or human (40 ng/ml) PLET1 (CUSABIO Technology LLC) in medium or left untreated. The TER was recorded at the indicated time points and is given as Ω / cm^2 .

Peptide-based kinase activity assay (phosphoproteome)

AEC were cultured until they reached confluence. rPlet1 treatment (20 ng/ml) was started 12 h prior to protein extraction for peptide-based kinase activity assay and western blot analysis. For protein lysate preparation, we placed cell cultures, grown in petri dishes (10 cm diameter dishes), on ice, and washed the cells twice with 5–6 ml cold PBS. Then we added 170 μ l M-PER lysis buffer (Thermo Fisher Scientific, Waltham, MA, USA) containing phosphatase and protease inhibitors (Pierce, Rockford, IL, USA). Cells were scraped and homogenized at least 3 times using a syringe-and-needle (20-gauge). The lysate was incubated for 1 h at 4 °C on rotating shaker followed by centrifugation at $16,000 \times g$ for 15 min. The supernatant containing

proteins was aliquoted and immediately flash-frozen in liquid nitrogen and stored at -80°C . Protein concentration was determined according to the manufacturer's instructions using bicinchoninic acid (BCA) protein assay kit (Thermo Fisher Scientific). Prepared cell lysates were used for peptide-based kinase activity assay and western blot analyses. We performed protein isolation and peptide-based tyrosine kinase activity assay on PTK (phospho-tyrosine kinase) as well as STK (serine/threonine kinase) chips using the PamStation[®]12 platform (Pamgene, BJ's-Hertogenbosch, The Netherlands) as previously described³⁹. Instrument operations such as initial processing of samples and arrays as well as image capture were conducted with Evolve12 software (Pamgene, BJ's-Hertogenbosch, The Netherlands). Numerical values of the individual phospho-peptide spot intensity were obtained by software-assisted densitometric quantification. Background reduction and log₂-transformation were done prior normalization (i.e., centering) for the two independent runs. Individual signatures of substrate peptide phosphorylation for each experimental condition (with or without rPlet1 treatment) are compared with databases containing empirical in vitro/in vivo as well as literature-based protein modifications.

Kinases that show a significant change in activity between the two experimental conditions (w/o rPlet1 vs rPlet1 treatment) are described by two important parameters: the “normalized median kinase statistics” (i.e., the predicted differential kinase activity) that depicts the overall change of the peptide set that represents the group of substrates for the given kinase, and the “mean specificity score”, which is expressed as the negative log₁₀ *p* value, where *p* < 0.05 refers to the statistical significance for the changes of the phosphorylation for the substrate peptide sets between the two experimental conditions. Therefore, predicted kinases with a high differential kinase activity (i.e. “normalized median kinase statistics”) and a “mean specificity score” higher than 1.3 were considered as promising candidates for subsequent investigations.

Western blot

Protein lysates were performed as described above. Equal protein amounts (30 µg) were added into each well. Proteins were separated by SDS-PAGE and transferred to nitrocellulose membranes for 60 min at 100 V. Membranes were blocked with 5% non-fat dry milk in PBS/Tween-20 for 1 h at RT. Thereafter, membranes were incubated with the primary antibody for 1 h at RT or at 4 °C o/n, in PBS/Tween-20 with non-fat dry milk, on a shaker. Primary antibodies were obtained from Cell Signaling Technology (Danvers, MA, USA) unless otherwise stated. The following primary antibodies were used: c-Raf (#9422, 1:1,000 dilution), p44/42 MAPK (Erk1/2) (#4695, 1:1,000 dilution), phospho-p44/42 MAPK (Erk1/2) (#4370, 1:1,000 dilution), phospho-c-raf (#9427, 1:1,000 dilution), GAPDH (#2118, 1:2,000 dilution). Membranes were washed with PBS/Tween-20 for 5 min, 3×, on a shaker. The HRP-linked secondary antibody (#7074S, Cell Signaling Technology) was diluted 1:2000 in 2% dry milk with PBS/Tween-20 and incubated with the membrane for 1 h at RT. Membranes were washed with PBS/Tween-20 for 5 min, 3×, on a shaker. Protein bands were visualized using SuperSignal[™] West Femto Maximum Sensitivity Substrate (Thermo Fisher Scientific) and detected using the enhanced chemiluminescent (ECL) western blotting system (GE Healthcare, München, Germany). The list of antibodies in Excel format including clone, company name, Cat No and the concentration used, is provided as Supplementary Data 1.

Cytokine quantification

We quantified concentrations of selected cytokines and chemokines in BALF of mice using a BioPlex MAGPIX Multiplex Reader (BIO-RAD, United States) according to the manufacturer's instructions. Data were analyzed with BioPlex Data Pro software.

Statistics

Data are shown in scatterplots as single data points. Mean ± SEM per group is indicated by bars and error bars. We used two-sided Student's test to compare between two groups, performing Welch's correction when sample distribution was significantly different between the compared groups. For the analysis of three or more groups, we used ANOVA followed by Tukey's post-test or Brown Forsythe and Welch ANOVA when samples presented different distributions. We used two-way ANOVA to compare samples presenting two variables followed by Sidak's post-test. We used Spearman's rank correlation test to detect a significant correlation in Fig. 7c, and Log-rank (Mantel–Cox) test to analyze survival curves. The statistical test used to address significant differences between groups is described in the legend of every graph and also the exact *p* values and *n* numbers. Graphs were prepared using GraphPad Prism (GraphPad Software version 9.3.1).

Reporting summary

Further information on research design is available in the Nature Portfolio Reporting Summary linked to this article.

Data availability

The microarray data used in this publication have been deposited in NCBI's Gene Expression Omnibus⁶⁵ and are accessible through GEO Series accession number [GSE208000](https://www.ncbi.nlm.nih.gov/geo/query/acc.cgi?acc=GSE208000). The scRNA-seq data have been deposited in NCBI's Gene Expression Omnibus⁶⁵ and are accessible through GEO Series accession number [GSE208294](https://www.ncbi.nlm.nih.gov/geo/query/acc.cgi?acc=GSE208294). Source Data are provided with this paper.

Code availability

Code for the scRNA-seq analysis is accessible at https://github.com/agbartkuhn/Pervizaj-Oruqaj_Plet1_sc_analysis. The custom-made macro and the pre-trained model that was used to quantify the fibrosis in lung sections are freely available online (<https://doi.org/10.5281/zenodo.10135192>).

References

1. Tighe, R. M. et al. Improving the quality and reproducibility of flow cytometry in the lung. An official American Thoracic Society Workshop Report. *Am. J. Respir. Cell Mol. Biol.* **61**, 150–161 (2019).
2. Ghoneim, H. E., Thomas, P. G. & McCullers, J. A. Depletion of alveolar macrophages during influenza infection facilitates bacterial superinfections. *J. Immunol.* **191**, 1250–1259 (2013).
3. Li, F. et al. Monocyte-derived alveolar macrophages autonomously determine severe outcome of respiratory viral infection. *Sci. Immunol.* **7**, eabj5761 (2022).
4. Aegerter, H. et al. Influenza-induced monocyte-derived alveolar macrophages confer prolonged antibacterial protection. *Nat. Immunol.* **21**, 145–157 (2020).
5. Serbina, N. V. & Pamer, E. G. Monocyte emigration from bone marrow during bacterial infection requires signals mediated by chemokine receptor CCR2. *Nat. Immunol.* **7**, 311–317 (2006).
6. Murray, P. J. et al. Macrophage activation and polarization: nomenclature and experimental guidelines. *Immunity* **41**, 14–20 (2014).
7. Herold, S., Mayer, K. & Lohmeyer, J. Acute lung injury: how macrophages orchestrate resolution of inflammation and tissue repair. *Front Immunol.* **2**, 65 (2011).
8. Herold, S. et al. Lung epithelial apoptosis in influenza virus pneumonia: the role of macrophage-expressed TNF-related apoptosis-inducing ligand. *J. Exp. Med.* **205**, 3065–3077 (2008).
9. Merad, M. & Martin, J. C. Pathological inflammation in patients with COVID-19: a key role for monocytes and macrophages. *Nat. Rev. Immunol.* **20**, 355–362 (2020).

10. Wendisch, D. et al. SARS-CoV-2 infection triggers profibrotic macrophage responses and lung fibrosis. *Cell* **184**, 6243–6261.e6227 (2021).
11. Peteranderl, C. et al. Macrophage-epithelial paracrine crosstalk inhibits lung edema clearance during influenza infection. *J. Clin. Invest.* **126**, 1566–1580 (2016).
12. Lucas, C. D. et al. Pannexin 1 drives efficient epithelial repair after tissue injury. *Sci. Immunol.* **7**, eabm4032 (2022).
13. Dagher, R. et al. IL-33-ST2 axis regulates myeloid cell differentiation and activation enabling effective club cell regeneration. *Nat. Commun.* **11**, 4786 (2020).
14. Lechner, A. J. et al. Recruited monocytes and type 2 immunity promote lung regeneration following pneumonectomy. *Cell Stem Cell* **21**, 120–134.e127 (2017).
15. Depreter, M. G. et al. Identification of Plet-1 as a specific marker of early thymic epithelial progenitor cells. *Proc. Natl Acad. Sci. USA* **105**, 961–966 (2008).
16. Murray, A., Sienerth, A. R. & Hemberger, M. Plet1 is an epigenetically regulated cell surface protein that provides essential cues to direct trophoblast stem cell differentiation. *Sci. Rep.* **6**, 25112 (2016).
17. Nijhof, J. G. et al. The cell-surface marker MTS24 identifies a novel population of follicular keratinocytes with characteristics of progenitor cells. *Development* **133**, 3027–3037 (2006).
18. Bennett, A. R. et al. Identification and characterization of thymic epithelial progenitor cells. *Immunity* **16**, 803–814 (2002).
19. Ulyanchenko, S. et al. Identification of a bipotent epithelial progenitor population in the adult thymus. *Cell Rep.* **14**, 2819–2832 (2016).
20. Raymond, K. et al. Expression of the orphan protein Plet-1 during trichilemmal differentiation of anagen hair follicles. *J. Invest. Dermatol.* **130**, 1500–1513 (2010).
21. Zepp, J. A. et al. IL-17A-induced PLET1 expression contributes to tissue repair and colon tumorigenesis. *J. Immunol.* **199**, 3849–3857 (2017).
22. Karrich, J. J. et al. Expression of Plet1 controls interstitial migration of murine small intestinal dendritic cells. *Eur. J. Immunol.* **49**, 290–301 (2019).
23. Guendel, F. et al. Group 3 innate lymphoid cells program a distinct subset of IL-22BP-producing dendritic cells demarcating solitary intestinal lymphoid tissues. *Immunity* **53**, 1015–1032.e1018 (2020).
24. Woodruff, P. G. et al. A distinctive alveolar macrophage activation state induced by cigarette smoking. *Am. J. Respir. Crit. Care Med.* **172**, 1383–1392 (2005).
25. Hung, L. Y. et al. Macrophages promote epithelial proliferation following infectious and non-infectious lung injury through a Trefoil factor 2-dependent mechanism. *Mucosal Immunol.* **12**, 64–76 (2019).
26. Hewitt, R. J. & Lloyd, C. M. Regulation of immune responses by the airway epithelial cell landscape. *Nat. Rev. Immunol.* **21**, 347–362 (2021).
27. Zhang, S. et al. Type 1 conventional dendritic cell fate and function are controlled by DC-SCRIPT. *Sci. Immunol.* **6**, eabf4432 (2021).
28. Beyer, M. et al. The beta2 integrin CD11c distinguishes a subset of cytotoxic pulmonary T cells with potent antiviral effects in vitro and in vivo. *Respir. Res.* **6**, 70 (2005).
29. Kim, H. et al. UMP-CMP kinase 2 gene expression in macrophages is dependent on the IRF3-IFNAR signaling axis. *PLoS One* **16**, e0258989 (2021).
30. Högner, K. et al. Macrophage-expressed IFN- β contributes to apoptotic alveolar epithelial cell injury in severe influenza virus pneumonia. *PLoS Pathog.* **9**, e1003188 (2013).
31. Pello, O. M. et al. Role of c-MYC in alternative activation of human macrophages and tumor-associated macrophage biology. *Blood* **119**, 411–421 (2012).
32. Liu, Y., Qi, X., Li, G. & Sowa, G. Caveolin-2 deficiency induces a rapid anti-tumor immune response prior to regression of implanted murine lung carcinoma tumors. *Sci. Rep.* **9**, 18970 (2019).
33. Ma, F. et al. Retinoid X receptor α attenuates host antiviral response by suppressing type I interferon. *Nat. Commun.* **5**, 5494 (2014).
34. Aran, D. et al. Reference-based analysis of lung single-cell sequencing reveals a transitional profibrotic macrophage. *Nat. Immunol.* **20**, 163–172 (2019).
35. Watanabe, S., Alexander, M., Misharin, A. V. & Budinger, G. R. S. The role of macrophages in the resolution of inflammation. *J. Clin. Invest.* **129**, 2619–2628 (2019).
36. Vazquez-Armendariz, A. I. et al. Multilineage murine stem cells generate complex organoids to model distal lung development and disease. *EMBO J.* **39**, e103476 (2020).
37. Quantius, J. et al. Influenza virus infects epithelial stem/progenitor cells of the distal lung: impact on Fgfr2b-driven epithelial repair. *PLoS Pathog.* **12**, e1005544 (2016).
38. Scott, C. L. et al. The transcription factor ZEB2 is required to maintain the tissue-specific identities of macrophages. *Immunity* **49**, 312–325.e315 (2018).
39. Weiss, A. et al. Targeting cyclin-dependent kinases for the treatment of pulmonary arterial hypertension. *Nat. Commun.* **10**, 2204 (2019).
40. Ahmad, K. A., Wang, G., Unger, G., Slaton, J. & Ahmed, K. Protein kinase CK2- α key suppressor of apoptosis. *Adv. Enzym. Regul.* **48**, 179–187 (2008).
41. Gibbings, S. L. et al. Three unique interstitial macrophages in the murine lung at steady state. *Am. J. Respir. Cell Mol. Biol.* **57**, 66–76 (2017).
42. Yona, S. et al. Fate mapping reveals origins and dynamics of monocytes and tissue macrophages under homeostasis. *Immunity* **38**, 79–91 (2013).
43. Joshi, N. et al. A spatially restricted fibrotic niche in pulmonary fibrosis is sustained by M-CSF/M-CSFR signalling in monocyte-derived alveolar macrophages. *Eur. Respir. J.* **55**, 1900646 (2020).
44. Hogner, K. et al. Macrophage-expressed IFN- β contributes to apoptotic alveolar epithelial cell injury in severe influenza virus pneumonia. *PLoS Pathog.* **9**, e1003188 (2013).
45. Grant, R. A. et al. Circuits between infected macrophages and T cells in SARS-CoV-2 pneumonia. *Nature* **590**, 635–641 (2021).
46. Liao, M. et al. Single-cell landscape of bronchoalveolar immune cells in patients with COVID-19. *Nat. Med.* **26**, 842–844 (2020).
47. Williams, M. & Svedberg, F. R. Does tissue imprinting restrict macrophage plasticity? *Nat. Immunol.* **22**, 118–127 (2021).
48. Netea, M. G. et al. Defining trained immunity and its role in health and disease. *Nat. Rev. Immunol.* **20**, 375–388 (2020).
49. Machiels, B. et al. A gammaherpesvirus provides protection against allergic asthma by inducing the replacement of resident alveolar macrophages with regulatory monocytes. *Nat. Immunol.* **18**, 1310–1320 (2017).
50. Roquilly, A. et al. Alveolar macrophages are epigenetically altered after inflammation, leading to long-term lung immunoparalysis. *Nat. Immunol.* **21**, 636–648 (2020).
51. Arafa, E. I. et al. Recruitment and training of alveolar macrophages after pneumococcal pneumonia. *JCI Insight* **7**, e150239 (2022).
52. Wu, J. et al. Calcitonin gene-related peptide promotes proliferation and inhibits apoptosis in endothelial progenitor cells via inhibiting MAPK signaling. *Proteome Sci.* **16**, 18 (2018).
53. Alysandratos, K. D., Herriges, M. J. & Kotton, D. N. Epithelial stem and progenitor cells in lung repair and regeneration. *Annu. Rev. Physiol.* **83**, 529–550 (2021).
54. Salwig, I. et al. Bronchioalveolar stem cells are a main source for regeneration of distal lung epithelia in vivo. *EMBO J.* **38**, e102099 (2019).

55. Duncan, J. S. & Litchfield, D. W. Too much of a good thing: the role of protein kinase CK2 in tumorigenesis and prospects for therapeutic inhibition of CK2. *Biochim. Biophys. Acta* **1784**, 33–47 (2008).
56. Wittekindt, O. H. Tight junctions in pulmonary epithelia during lung inflammation. *Pflug. Arch.* **469**, 135–147 (2017).
57. Short, K. R. et al. Influenza virus damages the alveolar barrier by disrupting epithelial cell tight junctions. *Eur. Respir. J.* **47**, 954–966 (2016).
58. Hardyman, M. A. et al. TNF- α -mediated bronchial barrier disruption and regulation by src-family kinase activation. *J. Allergy Clin. Immunol.* **132**, 665–675.e668 (2013).
59. Zhu, B. et al. Uncoupling of macrophage inflammation from self-renewal modulates host recovery from respiratory viral infection. *Immunity* **54**, 1200–1218.e1209 (2021).
60. Kuziel, W. A. et al. Severe reduction in leukocyte adhesion and monocyte extravasation in mice deficient in CC chemokine receptor 2. *Proc. Natl Acad. Sci. USA* **94**, 12053–12058 (1997).
61. Herold, S. et al. Alveolar epithelial cells direct monocyte trans-epithelial migration upon influenza virus infection: impact of chemokines and adhesion molecules. *J. Immunol.* **177**, 1817–1824 (2006).
62. Ritchie, M. E. et al. limma powers differential expression analyses for RNA-sequencing and microarray studies. *Nucleic Acids Res.* **43**, e47 (2015).
63. Wolf, F. A., Angerer, P. & Theis, F. J. SCANPY: large-scale single-cell gene expression data analysis. *Genome Biol.* **19**, 15 (2018).
64. Berg, S. et al. ilastik: interactive machine learning for (bio)image analysis. *Nat. Methods* **16**, 1226–1232 (2019).
65. Edgar, R., Domrachev, M. & Lash, A. E. Gene Expression Omnibus: NCBI gene expression and hybridization array data repository. *Nucleic Acids Res.* **30**, 207–210 (2002).
66. Yu, G., Wang, L. G., Han, Y. & He, Q. Y. clusterProfiler: an R package for comparing biological themes among gene clusters. *Omics* **16**, 284–287 (2012).

Acknowledgements

This study was funded by the German Research Foundation (DFG; KFO309 project number 284237345 to S.H., R.E.M., I.V. and W.S.; SFB-TR84 project number 114933180 to S.H.; SFB1021 project number 197785619 to S.H. and J.W.; EXC2026 project number 390649896 to S.H., I.V. and W.S.), the German Ministry for Education and Research (BMBF, grant IPSELON to S.H.), the German Center for Lung Research (DZL; to S.H., R.E.M., I.V., R.T.S., W.S.), the Institute for Lung Health (ILH; A.I.V.A., S.H., W.S.), and the von Behring Röntgen Foundation (grant 66-LV07 to I.V.).

We highly appreciate the contribution of Larissa Hamann, Stefanie Jarmer, Maria Gross, Florian Lueck and Melina Cohen for support with animal experiments, human BAL preparation and histology.

Author contributions

L.P.O., B.S., and M.F. designed and performed experiments, evaluated and interpreted data and wrote the manuscript. J.W., R.D.G. and M.B.

performed sequencing and bioinformatic analyses. M.H. and C.M. supported flow cytometry and infection experiments. A.W. and R.T.S. performed and interpreted phosphoproteome analyses. I.A. conducted image analysis on lung sections and interpreted the resulting data. B.W. and S.G. provided human lung tissue. A.I.V.A. designed, performed and interpreted organoid and scRNA-seq experiments. R.E.M., I.V. and W.S. edited the manuscript. S.H. designed experiments, interpreted data, wrote the manuscript, and financed the study.

Funding

Open Access funding enabled and organized by Projekt DEAL.

Competing interests

The authors declare no competing interests.

Additional information

Supplementary information The online version contains supplementary material available at <https://doi.org/10.1038/s41467-023-44421-6>.

Correspondence and requests for materials should be addressed to Susanne Herold.

Peer review information *Nature Communications* thanks Juan Quintana, Carlos Talavera-López and the other, anonymous, reviewer(s) for their contribution to the peer review of this work. A peer review file is available.

Reprints and permissions information is available at <http://www.nature.com/reprints>

Publisher's note Springer Nature remains neutral with regard to jurisdictional claims in published maps and institutional affiliations.

Open Access This article is licensed under a Creative Commons Attribution 4.0 International License, which permits use, sharing, adaptation, distribution and reproduction in any medium or format, as long as you give appropriate credit to the original author(s) and the source, provide a link to the Creative Commons licence, and indicate if changes were made. The images or other third party material in this article are included in the article's Creative Commons licence, unless indicated otherwise in a credit line to the material. If material is not included in the article's Creative Commons licence and your intended use is not permitted by statutory regulation or exceeds the permitted use, you will need to obtain permission directly from the copyright holder. To view a copy of this licence, visit <http://creativecommons.org/licenses/by/4.0/>.

© The Author(s) 2024

Macrophage-epithelial paracrine crosstalk inhibits lung edema clearance during influenza infection

Christin Peteranderl, ... , G.R. Scott Budinger, Susanne Herold

J Clin Invest. 2016;**126**(4):1566-1580. <https://doi.org/10.1172/JCI83931>.

Research Article

Infectious disease

Pulmonology

Influenza A viruses (IAV) can cause lung injury and acute respiratory distress syndrome (ARDS), which is characterized by accumulation of excessive fluid (edema) in the alveolar airspaces and leads to hypoxemia and death if not corrected. Clearance of excess edema fluid is driven mostly by the alveolar epithelial Na,K-ATPase and is crucial for survival of patients with ARDS. We therefore investigated whether IAV infection alters Na,K-ATPase expression and function in alveolar epithelial cells (AECs) and the ability of the lung to clear edema. IAV infection reduced Na,K-ATPase in the plasma membrane of human and murine AECs and in distal lung epithelium of infected mice. Moreover, induced Na,K-ATPase improved alveolar fluid clearance (AFC) in IAV-infected mice. We identified a paracrine cell communication network between infected and noninfected AECs and alveolar macrophages that leads to decreased alveolar epithelial Na,K-ATPase function and plasma membrane abundance and inhibition of AFC. We determined that the IAV-induced reduction of Na,K-ATPase is mediated by a host signaling pathway that involves epithelial type I IFN and an IFN-dependent elevation of macrophage TNF-related apoptosis-inducing ligand (TRAIL). Our data reveal that interruption of this cellular crosstalk improves edema resolution, which is of biologic and clinical importance to patients with IAV-induced lung injury.

Find the latest version:

<https://jci.me/83931/pdf>



Macrophage-epithelial paracrine crosstalk inhibits lung edema clearance during influenza infection

Christin Peteranderl,^{1,2} Luisa Morales-Nebreda,³ Balachandar Selvakumar,^{1,2} Emilia Lecuona,³ István Vadász,^{1,2} Rory E. Morty,^{1,2,4} Carole Schmoltdt,^{1,2} Julia Besselow,^{1,2} Thorsten Wolff,⁵ Stephan Pleschka,⁶ Konstantin Mayer,^{1,2} Stefan Gattenloehner,⁷ Ludger Fink,^{2,8} Juergen Lohmeyer,^{1,2} Werner Seeger,^{1,2,4} Jacob I. Sznajder,³ Gökhan M. Mutlu,⁹ G.R. Scott Budinger,³ and Susanne Herold^{1,2}

¹Department of Internal Medicine II, University of Giessen and Marburg Lung Center (UGMLC) Giessen, Germany. ²German Center for Lung Research (DZL). ³Division of Pulmonary and Critical Care Medicine, Northwestern University Feinberg School of Medicine, Chicago, Illinois, USA. ⁴Department of Lung Development and Remodeling, Max Planck Institute for Heart and Lung Research, Bad Nauheim, Germany. ⁵Division of Influenza Viruses and Other Respiratory Viruses, Robert Koch Institut, Berlin, Germany. ⁶Institute of Medical Virology and ⁷Department of Pathology, Justus Liebig University Giessen, Giessen, Germany. ⁸Institute of Pathology and Cytology, Wetzlar, Germany. ⁹Section of Pulmonary and Critical Care Medicine, The University of Chicago, Chicago, Illinois, USA.

Influenza A viruses (IAV) can cause lung injury and acute respiratory distress syndrome (ARDS), which is characterized by accumulation of excessive fluid (edema) in the alveolar airspaces and leads to hypoxemia and death if not corrected. Clearance of excess edema fluid is driven mostly by the alveolar epithelial Na,K-ATPase and is crucial for survival of patients with ARDS. We therefore investigated whether IAV infection alters Na,K-ATPase expression and function in alveolar epithelial cells (AECs) and the ability of the lung to clear edema. IAV infection reduced Na,K-ATPase in the plasma membrane of human and murine AECs and in distal lung epithelium of infected mice. Moreover, induced Na,K-ATPase improved alveolar fluid clearance (AFC) in IAV-infected mice. We identified a paracrine cell communication network between infected and noninfected AECs and alveolar macrophages that leads to decreased alveolar epithelial Na,K-ATPase function and plasma membrane abundance and inhibition of AFC. We determined that the IAV-induced reduction of Na,K-ATPase is mediated by a host signaling pathway that involves epithelial type I IFN and an IFN-dependent elevation of macrophage TNF-related apoptosis-inducing ligand (TRAIL). Our data reveal that interruption of this cellular crosstalk improves edema resolution, which is of biologic and clinical importance to patients with IAV-induced lung injury.

Introduction

Influenza A viruses (IAV) infect cells in the alveolus and induce primary viral pneumonia, which can progress to acute respiratory distress syndrome (ARDS) with high mortality (1). IAV-induced lung injury is characterized by exaggerated inflammatory responses and loss of barrier function, resulting in edema formation and severe hypoxemia (1–4). Resolution of inflammation together with repair of the damaged epithelium and edema fluid clearance are crucial events in the recovery phase of ARDS (5). It has been demonstrated that impaired edema resolution in ARDS patients is strongly correlated with increased mortality (6, 7). Therefore, understanding the molecular mechanisms by which IAV infection decreases lung edema clearance might provide therapeutic targets to improve clinical outcome in IAV-induced ARDS.

Fluid reabsorption is driven by an osmotic gradient generated by the coordinated regulation of the apically expressed epithelial sodium channel (ENaC) and the basolaterally expressed Na,K-ATPase. Sodium ions enter the epithelial cells via ENaC and are transported out of cells by the Na,K-ATPase, which promotes the

aquaporin-driven or transcellular removal of water from the alveolar airspace (8, 9). The Na,K-ATPase is a heterodimeric protein that couples the transfer of 3 sodium ions out of the cell in exchange for the intracellular transfer of 2 potassium ions with energy provided by the hydrolysis of ATP. It is therefore the major driver of vectorial sodium transport and has been shown to be an important determinant and limiting factor of net fluid clearance (10–15).

During IAV infection of the distal respiratory tract, the functional and structural impairment of the tight alveolar epithelial cell (AEC) layer, and thus the alveolo-capillary barrier results in fluid leakage from the vascular compartment into the alveolar space and persistent edema (4, 16, 17). However, the underlying mechanisms are not well understood. Recent findings suggest that an overly exuberant inflammatory response may contribute to alveolar barrier disruption via a mechanism that requires both tissue-resident and BM-derived macrophages (BMM) (4, 16, 18, 19). We have recently demonstrated that the cytokine TNF-related apoptosis-inducing ligand (TRAIL), when released in excessive amounts from alveolar macrophages (AMs) upon auto-crine IFN β stimulation, significantly contributes to IAV-induced immunopathology (4, 16).

Here, we identify a paracrine communication network between different cellular subsets within the inflamed alveolus, which we found is critical to affect alveolar fluid clearance (AFC) in IAV-induced lung injury. In vitro and in vivo IAV infection led

► Related Commentary: p. 1245

Conflict of interest: The authors have declared that no conflict of interest exists.

Submitted: August 4, 2015; **Accepted:** January 26, 2016.

Reference information: *J Clin Invest.* 2016;126(4):1566–1580. doi:10.1172/JCI83931.

to reduced plasma membrane expression of alveolar epithelial Na,K-ATPase and thus impaired lung edema clearance in vivo. We discovered that IAV-infected epithelial cells and macrophages, as well as noninfected neighboring epithelial cells, establish a specific communication network via epithelial type I IFN and especially the IFN-dependent, macrophage-expressed TRAIL, which determines Na,K-ATPase plasma membrane protein abundance and, thus, edema clearance during IAV infection. The identified pathways underlying this macrophage-epithelial crosstalk are amenable to therapeutic targeting to improve alveolar edema clearance in vivo and putatively improve outcome in patients with severe IAV-induced lung injury.

Results

IAV infection leads to decreased Na,K-ATPase protein abundance and impaired AFC. Murine intratracheal infection with H1N1 IAV A/PR/8/34 resulted in alveolar edema at day 7 postinfection (d7 pi) not present in PBS-treated control groups (Figure 1A, upper panel). The excessive fluid in the alveolar airspace upon IAV infection was associated with severe hypoxemia at d7 pi (Figure 1B) and substantial impairment of AFC in vivo detected at d2 and more pronounced at d7 pi (Figure 1C). We therefore assessed Na,K-ATPase α 1 subunit (NKA α 1) protein abundance, after in vitro H1N1 IAV infection of primary AEC. Gene expression levels of NKA α 1 did not change after IAV infection (data not shown); however, the total cell protein abundance was significantly decreased at 16 hours pi (16h pi) and 24h pi in murine AEC (mAEC) as well as in primary human AEC (hAEC) at 16h pi (Figure 1, E and F). In addition, IAV infection was associated with reduction of the immunofluorescent signal for NKA α 1 in vivo, which was particularly found within highly inflamed alveolar regions but was found less within less inflamed alveolar regions; noninfected mice showed high NKA α 1 expression (Figure 1A, lower panels).

Alveolar epithelial plasma membrane NKA α 1 is decreased after IAV infection in vitro. Na,K-ATPase is mostly stored in intracellular compartments but contributes to active ion transport and AFC when recruited to the basolateral cell membrane (20, 21). Therefore, we assessed NKA α 1 plasma membrane abundance by flow cytometry (gating strategy in Figure 1D), as well as by plasma membrane biotinylation and subsequent pulldown in in vitro-infected AEC. Both assays revealed reduced NKA α 1 protein abundance at the plasma membrane in mAEC and hAEC following IAV infection (Figure 1, G–J).

Reduced alveolar epithelial plasma membrane expression of NKA α 1 causes impaired AFC after IAV infection in vivo. We next investigated whether Na,K-ATPase levels were affected by IAV infection in vivo and assessed NKA α 1 plasma membrane protein abundance on distal lung epithelial cells, largely comprising type II alveolar epithelial cells (Supplemental Figure 1; supplemental material available online with this article; doi:10.1172/JCI83931DS1), by flow cytometry. IAV infection resulted in a reduction of plasma membrane NKA α 1 on alveolar epithelial cells in vivo already on d2 pi and most pronounced on d7 pi (Figure 2A), which correlated with the reduced fluid clearance depicted in vivo (Figure 1C). To assess if decreased levels of NKA α 1 were a direct cause of reduced AFC capacities after IAV infection, we either induced overexpression of NKA α 1 and NKA β 1 (22, 23) in

parallel by adenoviral delivery prior to IAV infection or increased Na,K-ATPase plasma membrane abundance by treatment of AEC by the β -adrenergic agonist salbutamol (15, 24). Adenoviral overexpression of NKA α 1 and NKA β 1 indeed restored total NKA α 1 in IAV-infected AEC to baseline levels in vitro (Figure 2C) and also plasma membrane expressed NKA α 1 in vivo (Figure 2D). Similarly, salbutamol treatment increased NKA α 1 plasma membrane abundance both in vitro and in vivo (Figure 2, B and D). Importantly, increased NKA α 1 expression on alveolar epithelial cells directly contributed to improved AFC after IAV infection in vivo (Figure 2E). In line, direct blockade of Na,K-ATPase activity by its specific inhibitor ouabain resulted in decreased AFC (Supplemental Figure 2).

A soluble mediator released from infected macrophages and AEC leads to decreased plasma membrane NKA α 1 protein abundance. Given our previous findings that alveolar and BMM contribute to AEC damage (4, 16) and that NKA α 1 was particularly reduced within strongly inflamed regions of the lung, we explored whether presence of AMs or BMM would further inhibit NKA α 1 after IAV infection. Indeed, epithelial cell NKA α 1 protein abundance of noninfected AEC was significantly reduced in the presence of infected AM alone and further reduced after infection of both AEC and either AM (Figure 3A) or BMM (Figure 3B). Notably, plasma membrane-expressed NKA α 1 was significantly decreased on noninfected AEC in presence of IAV-infected BMM (Figure 3, C and D). As AEC and AM/BMM were cultured without direct physical contact to each other, these results suggest that paracrine crosstalk via a soluble macrophage-produced mediator leads to NKA α 1 downregulation and that additional infection of AEC further reduced total and plasma membrane-expressed NKA α 1 (Figure 3, C and D). We therefore investigated whether the reduction of NKA α 1 at the plasma membrane after IAV infection in the AEC monoculture was similarly mediated by paracrine signaling rather than by IAV infection itself. We correlated viral protein expression (hemagglutinin, HA) to NKA α 1 plasma membrane abundance (Figure 3E), and indeed, plasma membrane NKA α 1 was predominantly reduced in the adjacent noninfected IAV-HA⁺ fraction of mAEC (Figure 3F) and hAEC (Figure 3G), as well as of alveolar cells after IAV infection in vivo (Figure 3H). Furthermore, treatment of mAEC with conditioned media of infected but not of PBS-treated mAEC was sufficient to decrease NKA α 1 plasma membrane protein abundance (Figure 3I).

Paracrine signaling of epithelial type I IFN- and IFN-dependent macrophage TRAIL leads to reduced plasma membrane NKA α 1 protein abundance in AEC. To identify soluble factors within the AEC-macrophage crosstalk network that mediated the observed effect on NKA α 1 plasma membrane expression in AECs, we analyzed coculture supernatants for proinflammatory cytokines by ELISA and cytometric bead array (data not shown). We found that IFN α — and to a minor extent IFN β (Figure 4A and Supplemental Figure 3) — were released from infected AEC, whereas BMM did not increase IFN α release upon IAV infection (Figure 4A). We recently demonstrated that type I IFNs are potent inducers of TNF family cytokines in AM, particularly of TRAIL (4, 16). Likewise, IAV infection of BMM with IAV led to a significant release of TRAIL (Figure 4B), which was type I IFN-dependent as demonstrated by use of BMM derived from type I IFN receptor-deficient

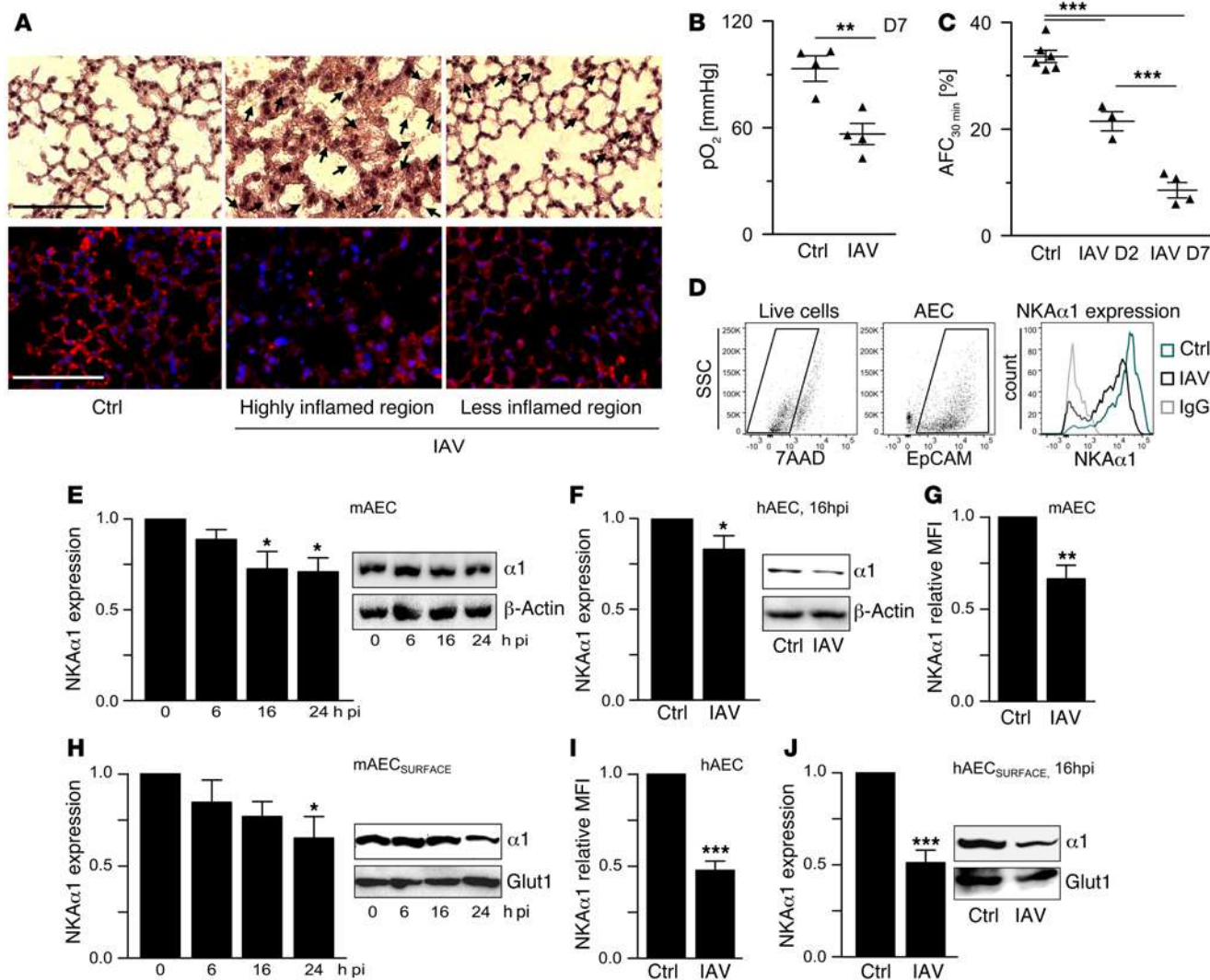


Figure 1. NKAα1 protein on the plasma membrane is decreased in a murine model of severe IAV infection. (A) Representative sections of $n = 3$ murine lungs d7 after PBS (ctrl) (left panel) or 500 pfu PR8 (IAV) inoculation in vivo, stained sequentially with anti-NKAα1 antibody (red) and DAPI (blue), followed by H&E staining. Sections of IAV-infected mice were taken from highly inflammatory (middle panel) and less inflammatory regions (right panel). Scale bars: 50 μm; arrows mark edematous regions. (B and C) Arterial partial pressure of oxygen (pO_2) (B) and in vivo AFC measurements (C) d7 pi after inoculation of PBS or PR8. (D) Gating strategy showing representative dot plots for live cells (7AAD⁻), epithelial cells (EpCAM⁺), and representative histograms of NKAα1⁺ staining or the respective IgG control from murine AEC cultures. SSC, side scatter. (E and F) Densitometric quantification of immunoblots of NKAα1 in relation to β-actin at the indicated time points in total cell lysates of mAEC (E) or hAEC (F) inoculated in vitro with PBS or PR8 for 24 hours. (G and I) Relative MFI of NKAα1 detected by FACS on live mAEC (G) or hAEC (I) treated in vitro with PBS (ctrl) or PR8 (IAV) at MOI 0.1 for 24 or 16 hours, respectively. (H and J) Densitometric analysis of NKAα1 expression in comparison to the housekeeping protein glucose transporter 1 (Glut1) within the cell surface fraction of PR8-infected mAEC at the indicated time points (H) or hAEC 16h pi (I). Values of PBS-treated control conditions were normalized to 1. Representative blots and bar graphs or dot plots show means ± SEM of 7–9 independent experiments for B, C, E, F, and H and 5–6 independent experiments for G, I, and J. Statistical significance was analyzed by unpaired Student's *t* test (B, F, G, I, and J) or by 1-way ANOVA and post-hoc Tukey (C, E, and H). * $P < 0.05$; ** $P < 0.01$; *** $P < 0.005$.

(*Ifnar*^{-/-}) mice (Figure 4C). AEC did not release TRAIL in response to IAV infection (Figure 4B). Treatment of uninfected AEC with either recombinant IFNα (rIFNα) or rTRAIL decreased NKAα1 protein abundance at the plasma membrane, and combined treatment with both IFNα and TRAIL reduced NKAα1 to similar levels as coinfection of AEC and BMM (Figure 4D). rIFNβ at levels found when released by infected AEC did not affect NKAα1 levels (Supplemental Figure 3). When using *Ifnar*^{-/-} AEC to block paracrine IFNα signaling between A/PR/8/34 (H1N1)-infected (PR8-infected) and noninfected AEC in monoculture, NKAα1 abun-

dance was rescued to baseline levels at 24h pi, whereas *Trail*^{-/-} AEC still displayed a strong decrease in NKAα1 protein abundance (Figure 4E). Moreover, transfer of conditioned media from either PBS-treated or PR8-infected AEC to *Ifnar*^{-/-} AEC did not reduce NKAα1 plasma membrane abundance (Figure 4F), suggesting that in absence of macrophages, NKAα1 surface downregulation was solely dependent on signaling through type I IFN. We next performed coculture infections using AEC and BMM from WT, *Ifnar*^{-/-}, *Trail*^{-/-}, or *Dr5*^{-/-} (TRAIL receptor) mice and assessed NKAα1 plasma membrane abundance after IAV infection. These

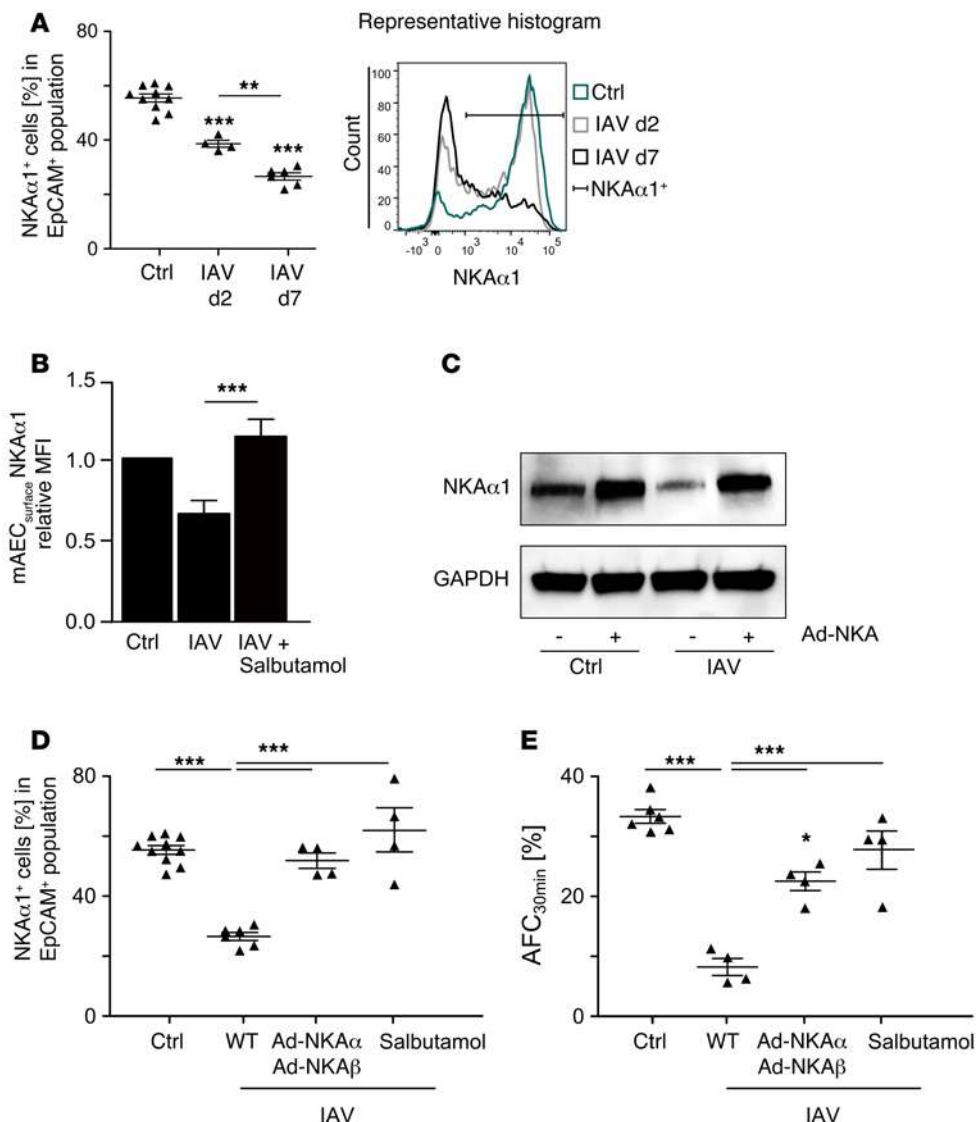


Figure 2. Reduced alveolar epithelial plasma membrane expression of NKAα1 causes impaired AFC after IAV infection in vivo. (A) Flow cytometric analysis of NKAα1 subunit expression on EpCAM⁺ epithelial cells from distal lung homogenate. WT mice were inoculated with PBS (ctrl) or PR8 (IAV) and sacrificed d2 or d7 pi. (B) Relative MFI of NKAα1 detected by FACS on live mAEC inoculated with PBS (ctrl) or PR8 at MOI 0.1 (IAV) and treated with 50 μM salbutamol. (C) Representative Western blot of 3 independent experiments blotting mAEC cell lysates for NKAα1 or GAPDH 72 hours after transfection with adenoviruses carrying NKAα1 or NKAβ1 at MOI 5 and 24 hours after PR8 infection at MOI 0.1. (D and E) WT mice were inoculated with PBS (ctrl) or PR8 (IAV) at d3 after intratracheal infection with adenoviruses overexpressing NKAα1 (Ad-NKAα) and NKAβ1 (Ad-NKAβ) or treated with 10 mg/kg salbutamol i.p. at d3 and d5. Mice were sacrificed at d7 after IAV infection. (D) Flow cytometric analysis of NKAα1 subunit expression on EpCAM⁺ epithelial cells from distal lung homogenate. (E) In vivo measurements of AFC rates over a time interval of 30 minutes. Graphs show single data points plus means ± SEM of 4–10 independent experiments for A, D, and E. Data sets depicting control conditions are identical to Figure 1C (AFC) and Figure 3A (NKAα1 expression) and included for better comparison between experimental conditions. Bar graph (B) represents means ± SEM of 3 independent experiments. Nonbracketed asterisk indicate statistical significance to control conditions. Statistical significance was analyzed by 1-way ANOVA and post-hoc Tukey. ****P* < 0.01; *****P* < 0.005.

studies revealed that lack of IFNAR signaling in AEC, together with lack of TRAIL in BMM, fully prevented NKAα1 downregulation in AEC. Partial blockade of the IFN-TRAIL signaling loop by combination of *Ifnar*^{-/-} AEC with WT BMM (allowing BMM TRAIL action), or of either WT AEC with *Trail*^{-/-} BMM or *Dr5*^{-/-} AEC with WT BMM (allowing AEC type I IFN signaling), correspondingly

resulted in reduced activation of caspase-3 in AEC at d7 pi (Supplemental Figure 4D). However, NKAα1 plasma membrane expression was not significantly altered after IAV infection by inhibition of caspase-3 activation, both in vitro as well as in vivo (Supplemental Figure 4, B and E). Accordingly, AFC rates were reduced to similar levels at d7 pi in IAV-infected mice or IAV-infected mice

resulted in partial decrease of plasma membrane NKAα1 (Figure 4G). Addition of recombinant human IFNα and/or recombinant human TRAIL to cultured hAEC reduced their ability for vectorial water transport as measured by changes in FITC-dextran concentrations in the apical versus basal medium of confluent hAEC to a similar extent as IAV infection (Figure 4H), whereas vectorial water transport of hAEC cocultured with primary human AM was significantly increased in the presence of neutralizing antibodies directed against IFNα and TRAIL after IAV infection (Figure 4I). Together, these data indicate that IAV-induced downregulation of NKAα1 and reduced ability for fluid transport depend on a signaling network between AEC and macrophages, involving epithelial type I IFN- and IFN-dependent macrophage TRAIL.

The TRAIL-mediated reduction of NKAα1 levels is induced independently of epithelial cell apoptosis. Previous work on the role of macrophage-released TRAIL during IAV infection demonstrated its contribution to extrinsic AEC apoptosis induction and to loss of barrier function (4, 16). To exclude that the observed effects of TRAIL on NKAα1 expression levels in noninfected AEC were caused by TRAIL-mediated induction of apoptosis, we inhibited activation of the effector caspase-3 by addition of the specific inhibitor Z-DEVD (25, 26) after IAV infection. In vitro and in vivo treatment with Z-DEVD resulted in significantly reduced levels of apoptotic alveolar epithelial cells after IAV infection for 24 hours and 7 days, respectively (Supplemental Figure 4, A and C). Moreover, application of Z-DEVD at d5 and d6 pi in vivo

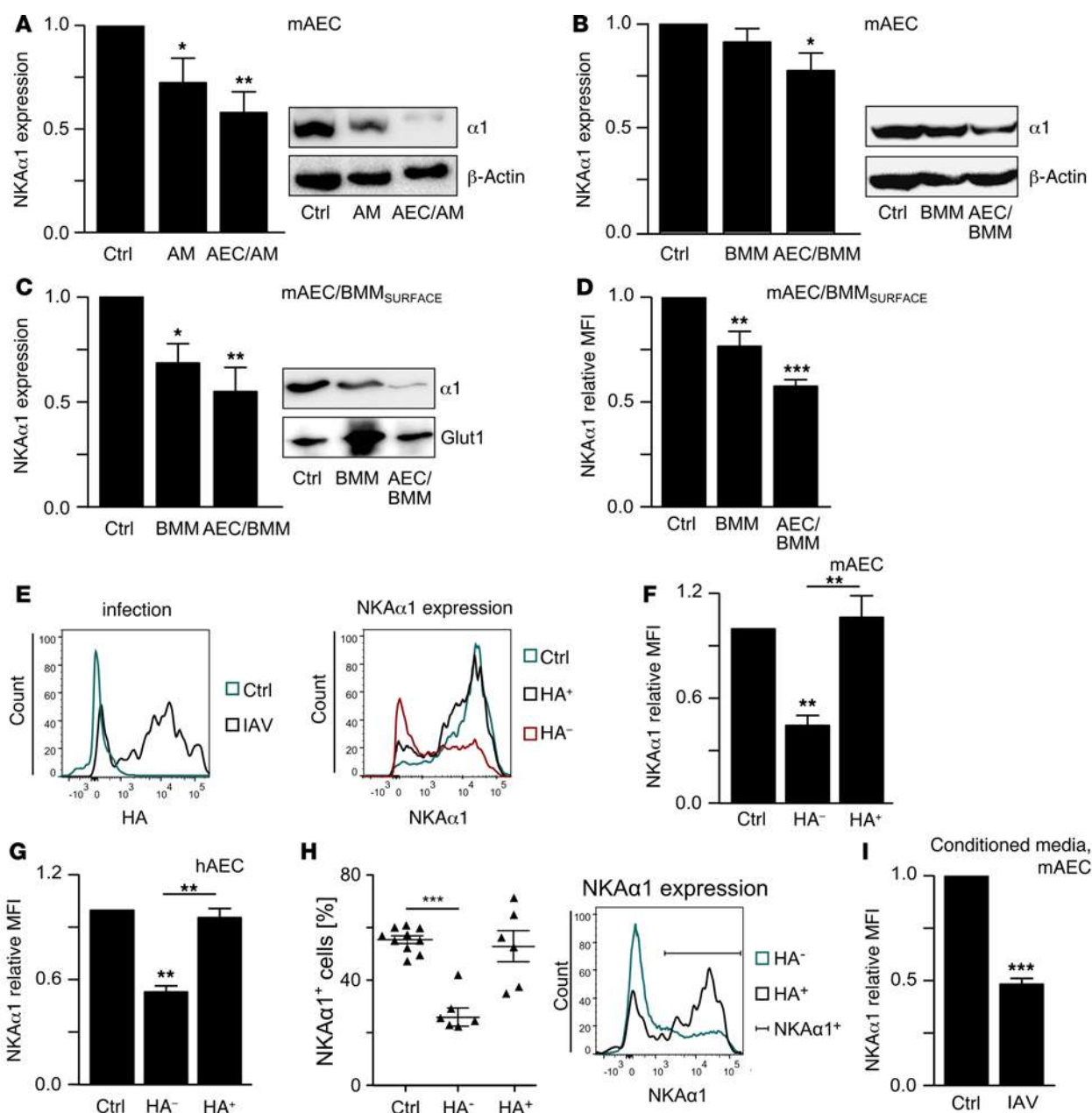


Figure 3. Epithelial plasma membrane-expressed Na,K-ATPase is decreased by a soluble mediator released from infected macrophages and AEC. (A and B) Densitometric quantification of Western blot of NKAα1 expression compared with β-actin at 24h pi in total cell lysates of mAEC after coculture with AM (A) or BMM (B) without infection (ctrl), infection of only macrophages (AM; BMM), or of both cell types (AEC/AM; AEC/BMM). (C) Densitometric analysis of NKAα1 expression compared with glucose transporter 1 (Glut1) within the cell surface fraction of 24h pi in PR8-infected mAEC cocultured with BMM. (D) Relative MFI of NKAα1 detected by FACS on live mAEC cocultured with BMM. (E) Gating strategy showing representative histograms for viral HA expression and NKAα1 expression on PBS-treated ctrl, IAV-infected HA⁺, or HA⁻ AEC. F and G depict NKAα1 MFI of HA⁺ vs. HA⁻ cell populations in mAEC (F) or hAEC (G) 24h pi with PR8 in comparison with PBS-treated cells (ctrl). (H) Flow cytometric analysis of NKAα1 subunit expression on EpCAM⁺ epithelial cells from distal lung homogenate. NKAα1 subunit expression was analyzed in AEC of PBS-treated mice (ctrl) or on the HA⁺ vs. HA⁻ cell population of AEC isolated from PR8-inoculated WT mice sacrificed at d7 pi. (I) Analysis of NKAα1 MFI of mAEC treated for 2 hours with conditioned media from 16 hours infected (IAV) or PBS-treated (ctrl) cells. For A–D, F, G, and I, values of PBS-treated control conditions were normalized to 1. Representative blots, histograms, and bar graphs showing means ± SEM of n = 8–10 experiments (A–C), n = 6 (D and F), n = 3 (G), n = 6–10 (H), and n = 4 (I). Data depicting control conditions in H are identical to 2A and are included for better comparison between experimental conditions. Statistical significance was analyzed by 1-way ANOVA and post-hoc Tukey. *P < 0.05; **P < 0.01; ***P < 0.005.

treated with Z-DEVD (Supplemental Figure 4F). Together, these data demonstrate that TRAIL-induced reduction of plasma membrane-expressed NKAα1, and its effects on net AFC are mediated independently of the induction of alveolar epithelial apoptosis.

The IFN/TRAIL-dependent reduction of NKAα1 plasma membrane abundance is mediated via AMPK. Given that Na,K-ATPase endocytosis was reported to be mediated by activation of AMP-activated protein kinase (AMPK) during lung injury-associated

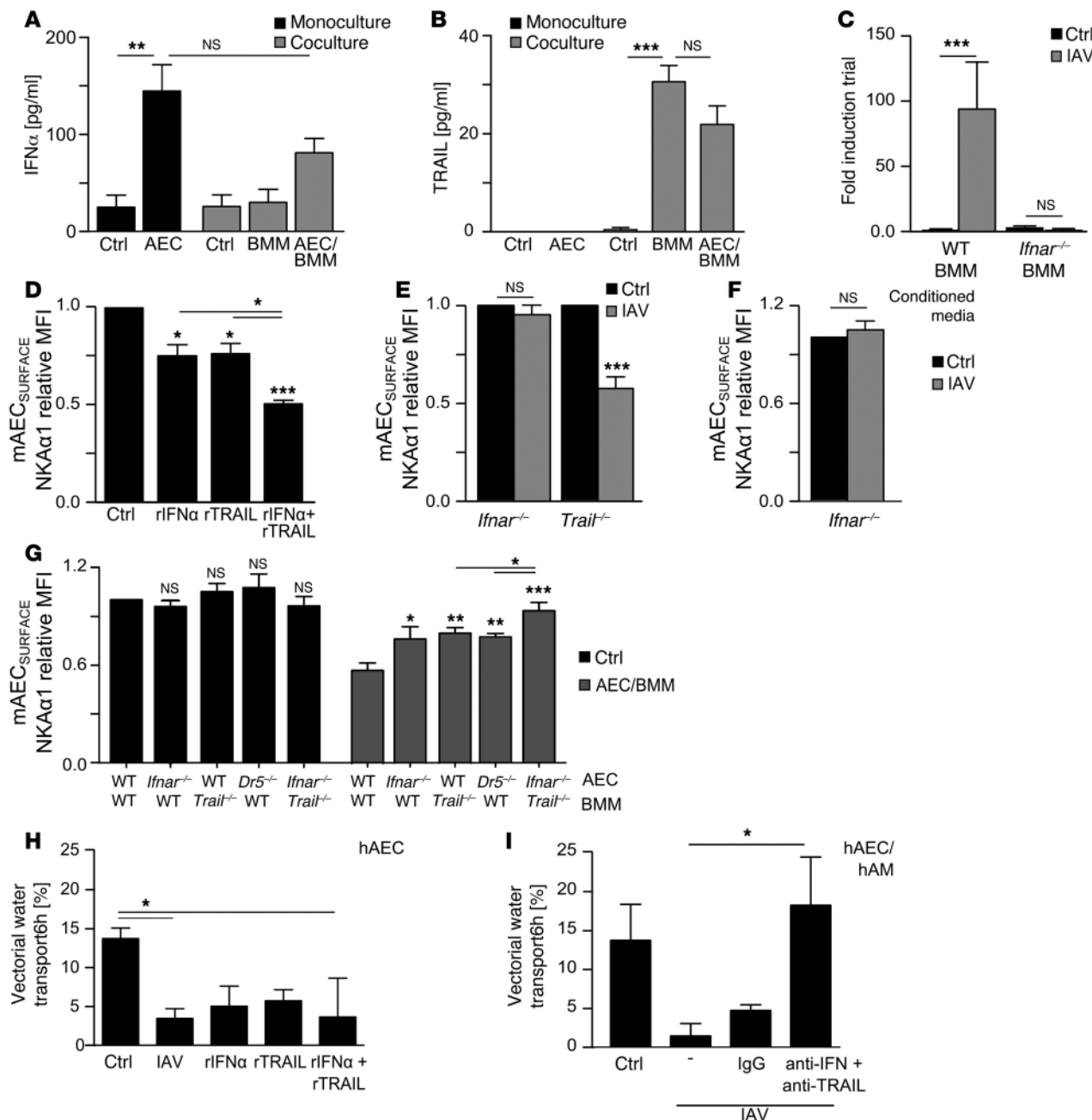


Figure 4. PR8-induced loss of Na,K-ATPase surface expression is dependent on an IFN-TRAIL signaling loop involving epithelial IFN α and type I IFN-induced macrophage TRAIL. (A and B) IFN α (A) and TRAIL (B) concentrations of AEC mono- and coculture supernatant 24h pi quantified by ELISA. mAEC were monocultured and inoculated in vitro with PBS (ctrl) or PR8 (AEC) or cocultured with BMM without infection (ctrl), with infection of only macrophages (BMM), or with infection of both cell types (AEC/BMM). (C) TRAIL mRNA expression quantified by qPCR in BMM isolated from WT or *Ifnar*^{-/-} mice noninfected (ctrl) or PR8-infected (IAV) at 16h pi. (D–G) NKA α 1 relative MFI on/of mAEC treated with 25U/ml mouse rIFN α or/and 100 pg/ml mouse rTRAIL for 16 hours (D); mAEC derived from *Ifnar*^{-/-} or *Trail*^{-/-} mice inoculated with PBS (ctrl) or PR8 (IAV) 24h pi (E); mAEC derived from *Ifnar*^{-/-} mice inoculated for 2 hours with conditioned media from PBS (ctrl) or PR8 (IAV) WT AEC infected for 16 hours (F); and mAEC derived from WT, *Ifnar*^{-/-}, or *Dr5*^{-/-} mice cocultured with BMM from WT or *Trail*^{-/-} mice and infection of none (ctrl) or both cell types (AEC/BMM) in vitro (G). Value of control conditions were normalized to 1. (H and I) Vectorial water transport of hAEC monolayers 6 hours after inoculation with PBS (ctrl), PR8 (IAV), rIFN α (150 pg/ml), and/or rTRAIL (100 pg/ml) or in coculture with human AM without additional treatment (–), in presence of neutralizing antibodies against human IFN α (0.5 μ g/ml) and human TRAIL (0.1 μ g/ml) (anti-IFN + anti-TRAIL) or the respective IgG controls (IgG). hAEC maintained barrier integrity in all assay conditions (Supplemental Figure 9). Bar graphs represent means \pm SEM of 4–6 independent experiments (A, B, and E–I), 3 independent experiments (C), and 6–8 independent experiments (D). Statistical significance was analyzed by Student's *t* test (F) or 1-way ANOVA and post-hoc Tukey (A–E and G–I). **P* < 0.05; ***P* < 0.01; ****P* < 0.005.

epithelial dysfunction (27, 28), we investigated if AMPK was involved in regulation of NKA α 1 abundance in response to IAV-induced paracrine signaling events. AMPK was indeed activated after IAV infection in AEC monocultures and AEC/BMM cocultures (Figure 5, A and B), as demonstrated by phosphorylation of the AMPK downstream substrate acetyl-CoA carboxylase (pACC) (29). Incubation of AEC with conditioned media of IAV-infected AEC and treatment with rTRAIL or rIFN α were sufficient to induce AMPK activation (Figure 5, C and D). Treatment of AEC with the AMPK activator AICA-Riboside (AICAR) (30, 31) led to decreased plasma membrane NKA α 1 in noninfected AEC and, importantly, chemical inhibition of AMPK by Compound C (32) restored NKA α 1 levels in infected AEC and in cocultured AEC in presence of infected BMM (Figure 5, E and F). In addition, adenoviral overexpression of a dominant-negative AMPK (DN-AMPK) in human lung epithelial cells (A549, ATCC) rescued NKA α 1 expression after IAV infection (Supplemental Figure 5A). We found that chemical inhibition of the AMPK upstream calcium/calmodulin-dependent protein kinase kinase β (CaMKK β) (33) by STO-609 in mAEC or siRNA knockdown of CaMKK β in A549 resulted in complete inhibition of AMPK activation and restored surface NKA α 1 abundance in IAV infection (Figure 5, G and H, and Supplemental Figure 5B). In addition, chelation of intracellular calcium needed for CaMKK β activation by BAPTA-AM increased NKA α 1 abundance on mAEC after IAV infection (Figure 5G). Inhibition of another possible upstream kinase of AMPK, the TGF β activated kinase 1 (TAK1), by (5Z)-7-Oxozeanol (34) caused partial inhibition of AMPK activity without affecting NKA α 1 expression (Figure 5, G and H). Accordingly, inhibition of Na,K-ATPase function by ouabain or IAV infection decreased, whereas inhibition of AMPK or CaMKK β prevented the reduction in fluid transport after IAV infection (Figure 5I), demonstrating that IFN/TRAIL-induced loss of membrane NKA α 1 involved a CaMKK β /AMPK-dependent pathway.

Consistent with the results from our in vitro infection model, inhibition of the intracellular kinase AMPK by intratracheal instillation and overexpression of adenoviral-expressed DN-AMPK in AEC prior to infection in vivo (Supplemental Figure 6A) prevented the IAV-induced reduction in NKA α 1 plasma membrane abundance and in AFC in vivo at d2 pi (Figure 6, A and B). Additionally, pharmacological inhibition of AMPK signaling in vivo by application of Compound C at d5 pi significantly increased NKA α 1 plasma membrane abundance and AFC at d7 after IAV infection (Figure 6, C and D). Neither DN-AMPK instillation nor Compound C treatment impacted on viral clearance (Supplemental Figure 6B and data not shown).

IFN and BMM-released TRAIL contribute to reduced NKA α 1 plasma membrane abundance and impaired AFC in vivo and are amenable to therapeutic targeting after IAV infection. We next investigated whether Na,K-ATPase levels were also dependent on the IFN/TRAIL signaling network in vivo. Interestingly, *Ifnar*^{-/-} mice (deficient for both IFN α ligation by the alveolar epithelium and for IFN β -dependent production of TRAIL by macrophages) were protected from IAV-induced reduction of NKA α 1 plasma membrane expression at d7 pi (Figure 7A). Consistent with our in vitro findings demonstrating that TRAIL released from BMM mediated the reduction of membrane NKA α 1 abundance during IAV

infection, both *Trail*^{-/-} mice and mice deficient for C-C chemokine receptor type 2 (*Ccr2*^{-/-}), which are unable to recruit macrophages from the BM to the lung after IAV-infection (35), were protected from NKA α 1 loss on distal lung epithelial cells in response to IAV infection when compared with WT animals (Figure 7, A and B). Moreover, we demonstrate, by intrapulmonary transfer of BMM flow-sorted (Supplemental Figure 7) from the lungs of WT or *Trail*^{-/-} mice at d7 after IAV infection into infected *Ccr2*^{-/-} mice, that rescue of NKA α 1 expression in *Ccr2*^{-/-} mice at d7 pi is lost in the presence of WT BMM but maintained after transfer of *Trail*^{-/-} BMM (Figure 7B). Accordingly, the IFN/TRAIL-mediated loss of surface NKA α 1 significantly reduced AFC in WT mice after IAV infection but not in *Ifnar*^{-/-}, *Trail*^{-/-}, or *Ccr2*^{-/-} mice (Figure 7C), which corresponded with decreased edema accumulation as quantified by wet-to-dry lung weight ratios in *Ifnar*^{-/-} and *Trail*^{-/-} mice (Supplemental Figure 8). Additionally, fluid clearance was completely restored in *Ccr2*^{-/-} mice that were supplemented with *Trail*^{-/-} BMM but not in *Ccr2*^{-/-} mice receiving WT BMM (Figure 7D). Moreover, in vivo targeting of the IFN/TRAIL signaling network by administration of anti-IFN α and anti-TRAIL neutralizing antibodies resulted in enhanced NKA α 1 protein abundance on the alveolar epithelium and significantly improved AFC capacities in IAV-infected WT mice, resulting in decreased edema formation and reduced morbidity, as demonstrated by body weight loss, and reduced overall morbidity scoring (Figure 8, A-D, and Supplemental Table 1). These data highlight a crucial role for the paracrine crosstalk involving IFN and macrophage-released TRAIL signaling for impairment of Na,K-ATPase-driven alveolar edema clearance capacity after IAV infection in vivo and suggest that targeting this axis is a promising approach to improve fluid clearance in humans after IAV-induced ARDS.

Discussion

Influenza virus pneumonia is characterized by infection of airway and alveolar epithelial cells and can rapidly progress to ARDS with dismal clinical outcome (1, 3). A functional impairment of the alveolar epithelial barrier after IAV infection results in pulmonary edema accumulation and impaired fluid reabsorption, which is closely correlated to mortality in ARDS patients (6, 7). Here, we report a mechanism by which a paracrine communication network between different populations of infected and adjacent cells in the alveolus downregulates alveolar epithelial Na,K-ATPase and thus inhibits AFC in response to IAV infection.

Our data demonstrate that the plasma membrane NKA α 1 protein abundance is reduced after IAV infection, indicating that the key function of Na,K-ATPase — active sodium transport out of the cell — is impaired (11, 12). Vectorial sodium and fluid clearance is a coordinated process that requires the electrochemical gradient generated by the basolateral Na,K-ATPase, thereby constituting the driving force of edema reabsorption. Sodium and water transport can also be regulated by the apically located ENaC and by chloride channels such as the cystic fibrosis transmembrane receptor (CFTR). In previous work, investigators reported that the levels of ENaC and CFTR were reduced in response to viral infection via a direct interaction with the viral matrix protein (36, 37). In contrast, we found that plasma membrane Na,K-ATPase protein abundance was disproportionately

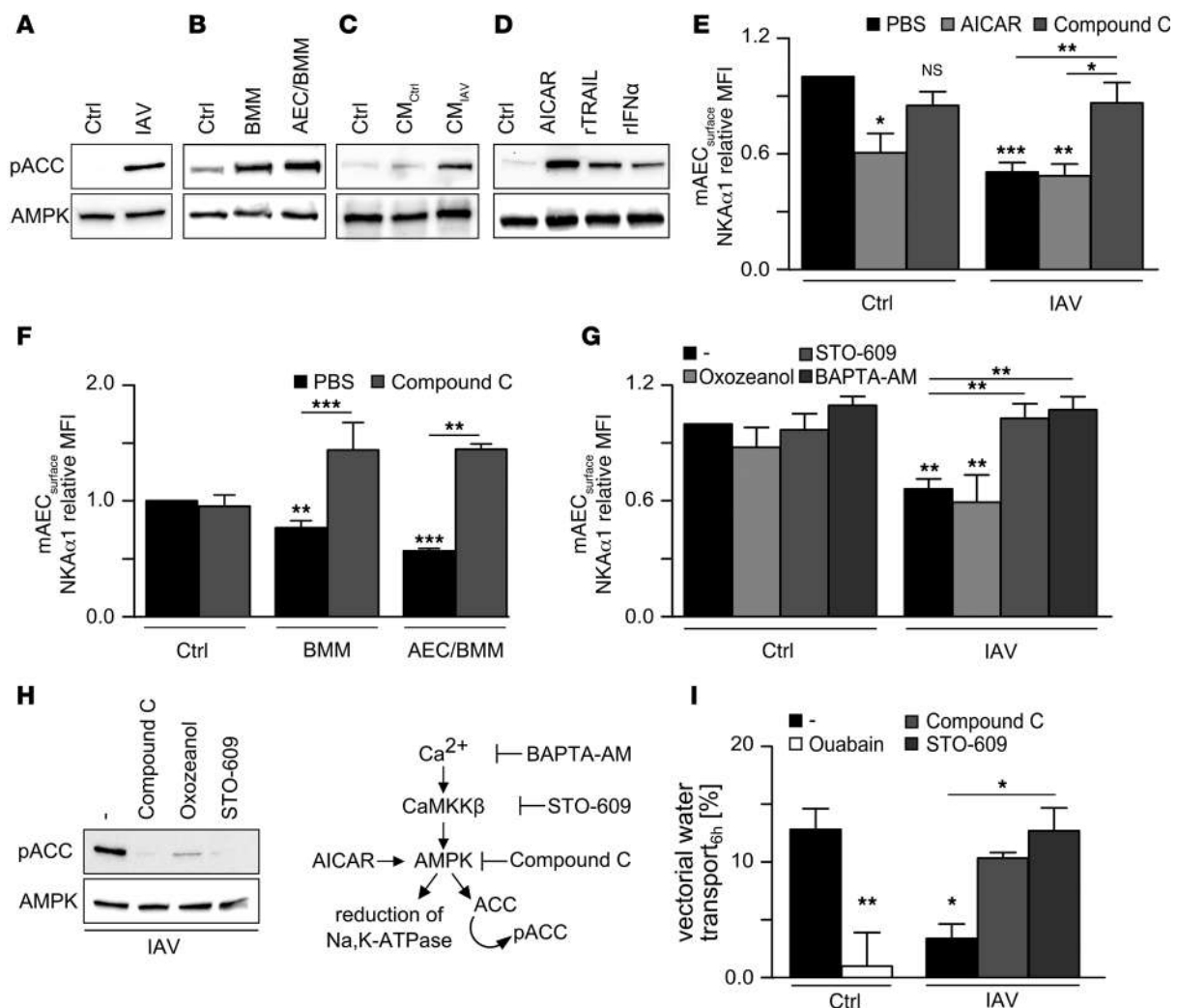


Figure 5. IAV-induced loss of NKAα1 surface expression is mediated by activation of AMPK. (A–D) Representative Western blots of $n = 3$ –4 independent experiments of AMPK (62 kDa) and the AMPK substrate pACC (280 kDa) mAEC treated with PBS (ctrl) or PR8 (IAV) (A) for 24 hours. (B) Cocultures of murine AEC and BMM were left uninfected (ctrl); only macrophages were infected (BMM) or both cell types were infected (AEC/BMM). (C) mAEC were treated with conditioned media (CM) of 16 hours PR8-infected (IAV) or PBS-treated (ctrl) mAEC for 2 hours. (D) mAEC treated with the AICAR (1 mM), rTRAIL (100 g/ml), or rIFNα (25 U/ml) for 16 hours. (E–G) Relative MFI of NKAα1 on mAEC inoculated with PBS (ctrl) or PR8 (IAV) for 24 hours without additional treatment or in presence of 1 mM AICAR or 20 μM Compound C (E); on mAEC cocultured with BMM without infection (ctrl), with infection of only macrophages (BMM), or with infection of both cell types (AEC/BMM) without additional treatment or in presence of 20 μM Compound C (F); on mAEC inoculated with PBS (ctrl) or PR8 (IAV) and incubated for 24 hours without additional treatment or in presence of 0.1 μM TAK1 inhibitor (SZ)-7-Oxozeanol or the 0.5 μM CaMKKβ inhibitor STO-609 or 10 μM of the Ca^{2+} chelator BAPTA-AM (G). (H) Representative Western blot of $n = 3$ –4 independent experiments of AMPK and pACC from 24 hours PR8-infected mAEC without additional treatment or in the presence of 20 μM Compound C, 0.1 μM (SZ)-7-Oxozeanol, or the 0.5 μM STO-609 and schematic depiction of the used inhibitors. (I) Vectorial water transport of confluent hAEC culture 6 hours after inoculation with PBS (ctrl) or PR8 (IAV) without additional treatment (–), in the presence of 25 μM Ouabain, 10 μM Compound C, or 0.5 μM STO-609. Bar graphs represent means \pm SEM of 4–6 independent experiments. Values of PBS-treated control conditions were normalized to 1. Statistical significance was analyzed by 1-way ANOVA and post-hoc Tukey. * $P < 0.05$; ** $P < 0.01$; *** $P < 0.005$.

reduced in neighboring, noninfected epithelial cells, suggesting that NKAα1 reduction is not mediated by direct interaction with a viral component but relies on paracrine signals released from the infected epithelial cells and macrophages. These findings highlight the need to understand influenza A infection in the context of integrated signaling networks involving different cell populations in the lung. Using a coculture system, we demonstrate the importance of epithelial IFNα- and IFN-induced macrophage TRAIL, which downregulated the AEC NKAα1 both in the presence and absence of IAV infection.

The type I IFNs play a complex role in the immune response to IAV infection. They are rapidly produced by AECs after viral infection to activate antiviral transcriptional programs in both epithelial and immune cells in the lung that are important for viral clearance. Furthermore, they may play a role in limiting the severity of the immune response via the production of IL-10 (38–40). Accordingly, IFNs have been suggested as potential therapeutic strategies to promote anti-IAV host defenses, particularly when applied as prophylactic treatment or early after onset of the infection (41, 42). Our data, however, indicate that

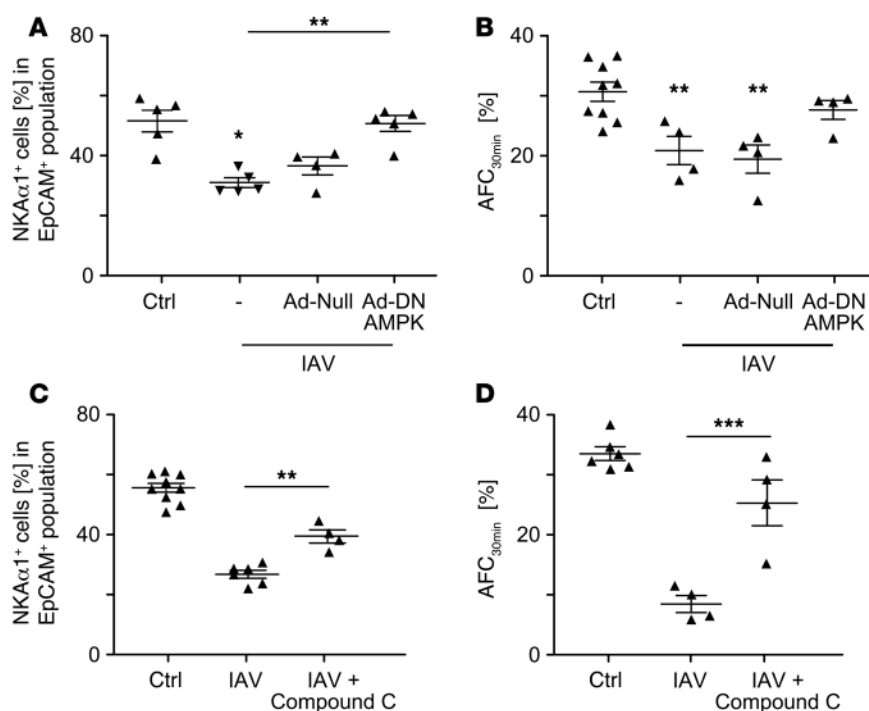


Figure 6. IAV-induced loss of NKAα1 surface expression is mediated by AMPK in vivo. (A and B) WT mice were inoculated with PBS (ctrl), Ad-Null, or Ad-DN AMPK for d7 prior to infection with PBS or IAV (Udorn) at d2 pi. (A) Flow cytometric analysis of NKAα1 subunit expression on AEC. (B) In vivo measurements of AFC rates over a time interval of 30 minutes. (C and D) WT mice were inoculated with PBS (ctrl) or PR8 (IAV) and treated with 20 mg/kg Compound C i.p. at d5 pi. Mice were sacrificed at d7 pi. (C) Flow cytometric analysis of NKAα1 subunit expression on AEC. (D) In vivo measurements of AFC rates over a time interval of 30 minutes. Graphs show means ± SEM of *n* = 4–5 (A), 4–9 (B), 4–9 (C), and 4–6 (D) independent experiments. Data set depicting control conditions in C and D are identical to Figure 1C (AFC) and Figure 3A (NKAα1 expression) and were included for better comparison between experimental conditions. Nonbracketed asterisk indicate statistical significance to control conditions. Statistical significance was analyzed by 1-way ANOVA and post-hoc Tukey. ***P* < 0.01; ****P* < 0.005.

at later time points, when the infection has spread to the alveolar compartment and progresses to lung injury, IFNs may also have a detrimental effect, evidenced by imbalanced inflammation and loss of crucial AEC functions such as edema clearance.

An important source of IFN and other proinflammatory cytokines in IAV-induced innate immune responses are AM- and CCR2-recruited BMM (43–45). Tissue resident AM play key roles in sensing viral infection and activating the initial innate and later adaptive immune responses to IAV infection (46). In concert with the macrophage populations recruited upon infection, they establish a proinflammatory environment by production and release of mediators such as IFN, leading to enhanced viral clearance and better disease outcomes (43, 47). However, it is well recognized that excessive production of cytokines during IAV infection contributes to lung injury, which impacts severity and outcome (48, 49), as shown for highly pathogenic avian influenza H5N1 or the pandemic 2009 H1N1 virus (50, 51). In particular, resident and recruited macrophages have been attributed as key roles in amplifying lung injury after IAV-infection by orchestrating an overly exuberant inflammatory response to IAV infection, worsening IAV-induced lung inflammation, lung injury severity, and mortality and hampering resolution of inflammation (4, 16, 44–48, 49, 50). In this regard, we and others revealed that IFNβ-induced autocrine activation of the death ligand TRAIL in BMM substantially deteriorates lung injury by promoting AEC injury after IAV infection (16, 52). Our current data provide important insights into these mechanisms, revealing a role of AEC-produced IFNα and macrophage-produced IFNβ-dependent TRAIL signaling within the alveolar cell-cell communication network in promoting impairment of epithelial barrier function and alveolar fluid homeostasis.

TRAIL has been widely associated with induction of extrinsic apoptosis in a variety of cells, including leukocyte subsets and cancer cells, via DR5 (53, 54). In the current study, we provide evidence

that the macrophage TRAIL/epithelial DR5 interaction exerts a role in virus-induced lung injury by activating the energy sensor AMPK. Of note, we demonstrated that TRAIL/AMPK-mediated reduction of NKAα1 plasma membrane abundance and impairment of AFC was independent of TRAIL-induced epithelial cell apoptosis induction in vivo (4, 16), as inhibition of AEC apoptosis by application of Z-DEVD did not impact on NKAα1 reduction after IAV infection. Activation of the metabolic sensor/regulator AMPK, under normal conditions, upregulates ATP generating and downregulates ATP-consuming mechanisms to promote cellular survival during metabolic stress (34, 55, 56). Of note, Herrero-Martín et al. demonstrated that rTRAIL was able to activate AMPK in immortalized epithelial cells and, thus, promote autophagy, a cytoprotective mechanism rendering cells more resistant to deleterious challenges (57), highlighting the complexity of the IFN/TRAIL network in cellular injury and protection in response to cellular stress.

The Na,K-ATPase has been well documented to be targeted for downregulation via a pathway that requires AMPK and subsequent activation of PKCζ in response to stimuli that threaten metabolic homeostasis, including alveolar hypercapnia and hypoxia (27, 28). We demonstrate activation of AMPK signaling by paracrine mediators in response to IAV infection, resulting in reduced vectorial sodium transport. Inhibiting AMPK in vivo by DN-AMPK or Compound C treatment attenuated the Na,K-ATPase downregulation and restored AFC rates in IAV-infected mice. These data highlight AMPK as a critical regulator of AFC in pulmonary injury in vivo, suggesting it as a therapeutic target for the treatment of IAV (58). At low levels, however, IFN/TRAIL- and AMPK-mediated reductions in vectorial sodium transport and fluid clearance in the IAV-infected lung may be beneficial, particularly during early stages of the disease when viral replication occurs and viral loads still increase. It has been reported that alterations of sodium currents within the IAV-infected cell show

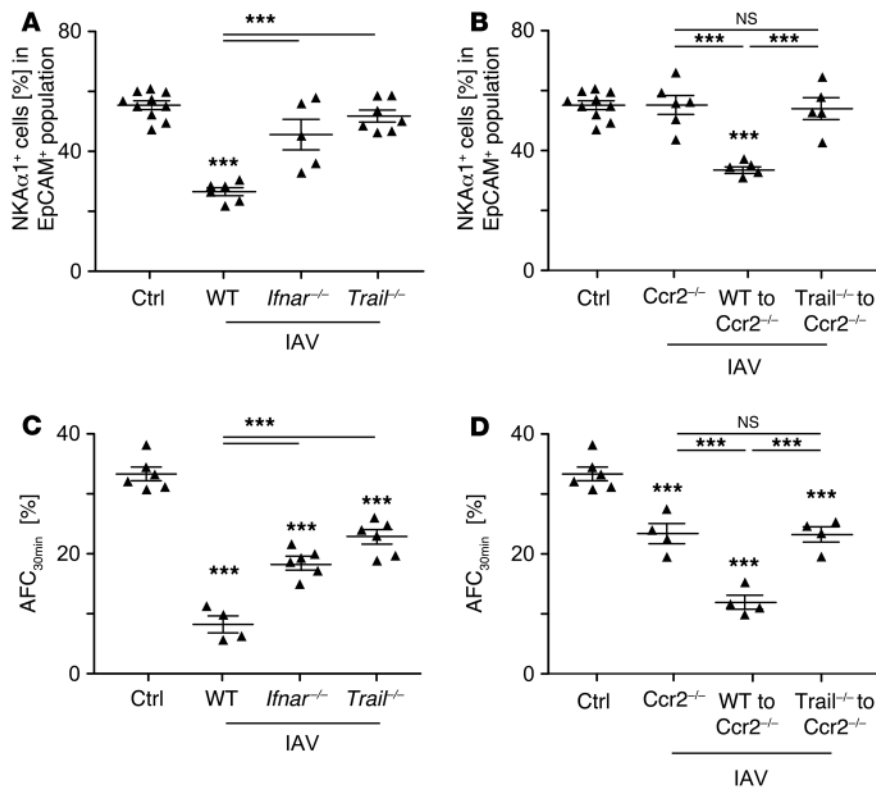


Figure 7. IAV-induced reduction of epithelial NKAα1 surface expression and AFC capacity require the presence of IFNAR and macrophage-released TRAIL in vivo. (A and B) Flow cytometric analysis of NKAα1 subunit expression on EpCAM⁺ epithelial cells from distal lung homogenate. (C and D) In vivo measurements of AFC rates over a time interval of 30 minutes. (A and C) WT, *Ifnar*^{-/-}, or *Trail*^{-/-} mice were inoculated with PBS (ctrl) or PR8 (IAV) and sacrificed d7 pi. (B and D) *Ccr2*^{-/-} mice were inoculated with PR8 (IAV) and sacrificed d7 pi without further intervention (*Ccr2*^{-/-}) or after intratracheal transfer of flow-sorted alveolar BMM from d7 infected WT (WT to *Ccr2*^{-/-}) or *Trail*^{-/-} (*Trail*^{-/-} to *Ccr2*^{-/-}) mice at d3 pi. Viral loads were not significantly altered between experimental groups (data not shown). Graphs show single data points plus means ± SEM of 5–10 independent experiments for A and B and 4–6 independent experiments for C and D. Data sets depicting control conditions are similar to Figure 1C (AFC) and Figure 3A (NKAα1 expression). Nonbracketed asterisk indicate statistical significance to control conditions. Statistical significance was analyzed by unpaired Student's *t* test (B) or by 1-way ANOVA and post-hoc Tukey. ****P* < 0.005.

an adverse effect on viral replication (59). Therefore, the resulting changes in intracellular sodium or potassium might interfere with viral signaling, providing an antiviral defense strategy for the infected cell. Alternatively, reduced Na,K-ATPase function might represent activation of a stress response pathway, perhaps secondary to changes in intracellular calcium, that reduces the susceptibility of neighboring epithelial cells to viral infection (59). Consistent with this hypothesis, we found that signaling through IFNAR and DR5 by IFN and TRAIL, respectively, activates AMPK via a pathway that requires CaMKKβ, which is in turn activated by increases in intracellular calcium (58). While the links between calcium signaling and the AMPK during influenza A infection have not been completely elucidated, previous studies have shown that, in hypoxic conditions, an influx of extracellular calcium through stromal interaction molecule 1-activated (STIM1-activated) calcium release-activated calcium channels (CRAC channels) can lead to CaMKKβ- and AMPK-mediated endocytosis of Na,K-ATPase (27). Wang et al. demonstrated that the calcium-dependent tyrosine kinase Pyk2 interacts with the IFNAR-associated tyrosine kinases Jak1/Tyk2 (60), providing a possible link to CaMKKβ activation.

Our in vitro studies provide complementary lines of evidence demonstrating an additive role for epithelial-produced IFNα- and IFN- dependent macrophage TRAIL in the downregulation of Na,K-ATPase plasma membrane protein abundance during IAV infection. Concordant with our in vitro findings, *Ifnar*^{-/-} mice deficient in the IFNα/β receptor, and thus compromised in both epithelial IFN crosstalk and IFN-dependent induction of macrophage TRAIL expression, displayed less reduction of Na,K-ATPase and were less impaired in AFC after IAV challenge.

Trail^{-/-} mice and mice lacking BMM recruitment from the circulation (*Ccr2*^{-/-}) were similarly protected from IAV-induced epithelial Na,K-ATPase downregulation. Of course, we cannot fully exclude that additional factors (e.g., infection-induced activation of intracellular pathways) affecting Na,K-ATPase function rather than mere surface expression (e.g., ion or ATP affinity or channel open probability) might have further influence on net AFC in our different in vivo models, as we observe substantially but not fully restored AFC rates ranging between similar levels in all gene-deficient mice applied (*Ifnar*^{-/-}, *Trail*^{-/-}, and *Ccr2*^{-/-}).

Further investigation on the effect of TRAIL released from recruited BMM after infection was performed via pulmonary transfer of WT but not *Trail*^{-/-} BMM into *Ccr2*^{-/-} mice after IAV infection, which led to decreased NKAα1 abundance and AFC similar to the decrease observed in IAV-infected WT mice and demonstrated the crucial role for TRAIL-expressing macrophages in the inhibition of AFC in vivo. We acknowledge that, in these studies, we did not address effects on overall survival, nor the consequences of TRAIL-deficiency on virus clearance, but we could importantly show that therapeutic blockade of the IFN/TRAIL network by neutralizing antibodies in vivo proved to increase NKAα1 expression and AFC after IAV infection. Considering that anti-TRAIL treatment was recently demonstrated to elicit profound effects in attenuating IAV-induced barrier disruption and to prevent pneumococcal superinfection (61), we suggest that therapeutic targeting of the here described signaling axis will not only ameliorate AFC after IAV infection, but will furthermore protect from TRAIL-mediated lung injury and complications thereof. We anticipate that targeting particularly macrophage TRAIL alone or together with epithelial

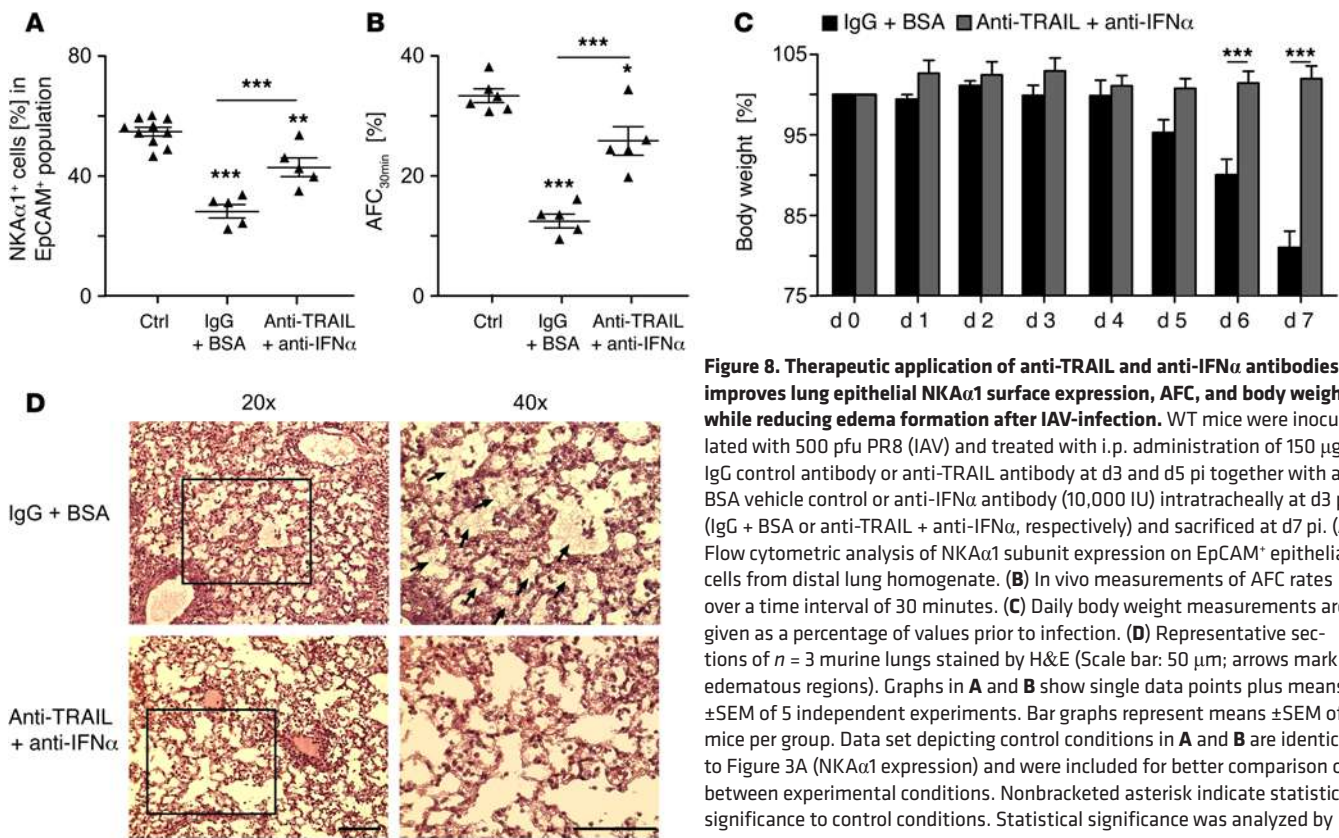


Figure 8. Therapeutic application of anti-TRAIL and anti-IFN α antibodies improves lung epithelial NKA α 1 surface expression, AFC, and body weight while reducing edema formation after IAV-infection. WT mice were inoculated with 500 pfu PR8 (IAV) and treated with i.p. administration of 150 μ g IgG control antibody or anti-TRAIL antibody at d3 and d5 pi together with a BSA vehicle control or anti-IFN α antibody (10,000 IU) intratracheally at d3 pi (IgG + BSA or anti-TRAIL + anti-IFN α , respectively) and sacrificed at d7 pi. (A) Flow cytometric analysis of NKA α 1 subunit expression on EpCAM $^{+}$ epithelial cells from distal lung homogenate. (B) In vivo measurements of AFC rates over a time interval of 30 minutes. (C) Daily body weight measurements are given as a percentage of values prior to infection. (D) Representative sections of $n = 3$ murine lungs stained by H&E (Scale bar: 50 μ m; arrows mark edematous regions). Graphs in A and B show single data points plus means \pm SEM of 5 independent experiments. Bar graphs represent means \pm SEM of 5 mice per group. Data set depicting control conditions in A and B are identical to Figure 3A (NKA α 1 expression) and were included for better comparison of between experimental conditions. Nonbracketed asterisk indicate statistical significance to control conditions. Statistical significance was analyzed by 1-way ANOVA and post-hoc Tukey. *** $P < 0.005$.

AMPK downstream signaling might be beneficial with respect to alveolar barrier protection and edema reabsorption, without compromising antiviral host defense.

In conclusion, we describe a paracrine pathway in the IAV-infected lung that links macrophage and epithelial signaling to the downregulation of the Na,K-ATPase in the non-infected fraction of AECs. This decrease is mediated by AEC-released IFN α directly and is strongly amplified through IFN α / β -induced release of TRAIL from recruited macrophages, resulting in inhibition of lung edema clearance (Figure 9). A timely modulation of this pathway might represent a novel strategy to improve fluid reabsorption and, thus, outcomes in IAV-induced lung injury and ARDS.

Methods

Supplemental Methods are available online with this article.

Mice. WT C57BL/6 mice were purchased from Charles River Laboratories. *Trail* $^{-/-}$ mice (62) were provided by AMGen. U. Kalinke (Paul-Ehrlich Institute, Erlangen, Germany) provided *Ifnar* $^{-/-}$ mice (63). *Dr5* $^{-/-}$ mice were a gift from T. Mak (Campbell Family Institute for Breast Cancer Research, University of Toronto, Toronto, Ontario, Canada) (64). *Ccr2* $^{-/-}$ mice were obtained from W. Kuziel (University of North Carolina Medical School, Chapel Hill, North Carolina, USA; ref. 65). All transgenic lines were backcrossed to the C57BL/6 background. Mice were housed under pathogen-free conditions.

Cell isolation and culture. Primary mAEC or hAEC were isolated as previously described (16, 66), seeded on 4 μ m-pore size transwells (Corning Inc.), and cultured for 3 and 5 days, respectively, prior to

experiments. AEC suspensions with a purity $>90\%$ were used for further experiments. Murine resident AMs were isolated by bronchoalveolar lavage as described (16) and cultured for 2 hours before treatment. Human resident AMs were gained from bronchoalveolar lavage fluid (BALF) of patients who did not show any accumulation of recruited inflammatory cells according to differential counts of pappenheim-stained cytopins. BMM were isolated from femurs and tibias and cultured in the presence of mouse recombinant granulocyte/macrophage-CSF (GM-CSF) at 25 ng/ml for 10 days.

Infection protocols. Cells were infected with PR8 at a multiplicity of infection (MOI) of 0.1 as previously described (16). For coculture experiments, bottom-seeded AM or BMM were combined with AEC seeded on transwells after infection of only macrophages or of both cell types with PR8. Of note, an abortive replication cycle occurred in AM and BMM, as described in Högnér et al. (16), and ensured that in the AM/BMM infection-only conditions, no virus was transferred to the epithelial cell layer excluding AEC infection. For in vitro experiments, recombinant murine TRAIL (R&D Systems, 100 pg/ml), recombinant murine GM-CSF (R&D Systems, 25 ng/ml) recombinant mouse IFN α and β (PBL Interferon Source, 25 U/ml; R&D Systems, 10–100 ng/ml), recombinant human IFN α (R&D Systems, 150 pg/ml), recombinant human TRAIL (R&D Systems, 100 pg/ml), anti-human IFN α neutralizing antibody (R&D Systems, 0.5 μ g/ml), anti-human TRAIL neutralizing antibody (R&D Systems, 0.1 μ g/ml), and the following chemical inhibitors were used: AICAR, AMPK inhibitor Compound C, (5Z)-7-Oxozeanol (Curvularia sp), STO-609 (all Calbiochem) and BAPTA-AM (Invitrogen). Conditioned media of 16h-infected mAEC cultured in 6-well plates was transferred to uninfected mAEC

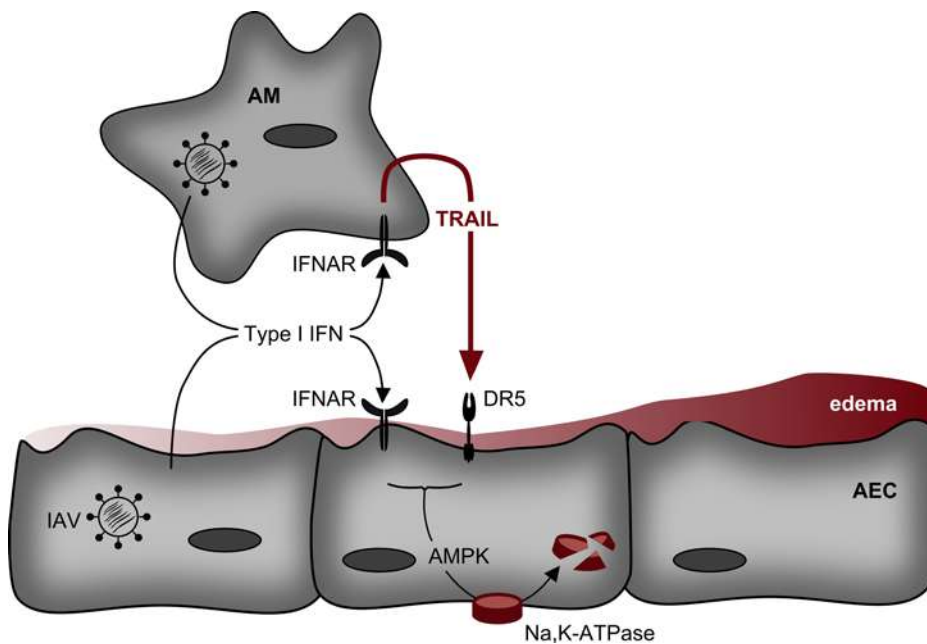


Figure 9. Model of type I IFN-mediated loss of Na,K-ATPase-mediated edema clearance in IAV infection. IAV infection results in AEC release of IFN α and induction of IFN β -dependent release of TRAIL in AMs. Ligation to their receptors, IFNAR and particularly DR5, results in activation of the stress kinase AMPK. Activation of AMPK initiates degradation and reduction of Na,K-ATPase abundance on the cell plasma membrane and impacts on fluid reabsorption, leading to the persistence of lung edema after IAV infection.

cultured in 12-well plates and incubated for 2 hours. For *in vivo* infection, mice were intratracheally inoculated with 500 plaque-forming units (pfu) PR8 or 10^5 pfu A/Udorn/307/1972 (H3N2, also known as Udorn) diluted in 70- μ l sterile PBS. Endotracheal delivery of adenovirus was performed at 1×10^9 pfu in 50% surfactant vehicle as described previously (24). Adenoviruses carrying either no additional construct (Ad-Null) — or expressing DN-AMPK, Ad-NKA α 1, or Ad-NKA β 1 — were cloned at ViraQuest Inc. Of note, NKA β 1 — which was shown to be a crucial mediator for correct heterodimerization of the Na,K-ATPase (22, 67) — was coexpressed to ensure presence of sufficient levels of NKA β 1 to support functional Na,K-ATPase formation.

Of note, transduction efficiency was >90% in AEC, as verified by FACS for mCherry in EpCAM $^+$ cells (not shown). Neutralizing antibodies against IFN α (10,000 IU/mouse, rabbit polyclonal Ab to mouse IFN α , PBL Interferon Source) were administered intratracheally at d3 pi, and neutralizing antibodies against TRAIL (150 μ g/mouse, LEAF anti-mouse CD253, BioLegend) were given *i.p.* at d3 and d5 pi as established previously (16). Infected mice were monitored 1–3 times per day.

In vivo measurement of AFC. The rate of fluid removal from the alveolar airspace was measured by assessment of changes in Evans blue-tagged albumin in an iso-osmolar alveolar instillate over 30 minutes as previously described (24). In short, mice were anesthetized, placed on a heating pad, and maintained in supine position. Body temperature was monitored using an anal probe and maintained at 37°C with heating pad and lamp. After reaching stable anesthesia, mice were cannulated with a shortened 18-gauge *i.v.* catheter, paralyzed with 2.0 mg/kg pancuronium bromide applied *i.p.*, and ventilated via catheter connected to a mouse respirator (Harvard Apparatus) using a tidal volume of 10 ml/kg (equivalent of 0.2 ml) at a frequency of 160 breaths per minute and 100% of oxygen, as described by Hardiman et al. (68). Iso-osmolar NaCl solution (324 mOsm; 300 μ l) containing 5% Evans blue-tagged (0.15 mg/ml) bovine serum albumin were installed via the catheter over a time period of 30 seconds, followed by 0.1 ml of air; then, mice were ventilated over 30 minutes. Evans blue concen-

trations, directly correlating with the amount of BSA in the solution, were analyzed from the initial instillate and the reaspirated fluid using a microplate reader (Bio-Rad, 620-nm filter) and AFC was calculated as follows: $AFC = 1 - (C_0/C_{30})$, where C_0 is the protein concentration before instillation and C_{30} is the protein concentration of the sample reaspirated after 30 minutes of ventilation.

Ex vivo measurement of vectorial water transport. Primary human AEC were seeded in 0.4 μ m-pore size transwell cell culture dishes (Corning Inc.) and cultured until achieving electrochemical resistances of $\geq 800 \Omega/\text{cm}^2$ as measured by Millicell-ERS2 device (EMD Millipore). Cells were infected with PR8 at MOI 0.1 or PBS treated for 1 hour at 37°C and then supplied with 3 mg/ml 70 kDa FITC-dextran-labeled (Sigma-Aldrich) cell culture media including selected inhibitors at indicated concentrations. After 6 hours of incubation at 37°C, apical and basal media were analyzed for FITC-dextran concentration (FL $_x$ 800, Bio-Tek). Cells were analyzed microscopically for bound FITC-dextran without apparent differences in the treatment groups. Vectorial water transport was calculated by changes in FITC-dextran concentration between apical (C_a) and basal (C_b) media in comparison with starting conditions (C_0): $[1 - (C_0/C_a)] - [1 - (C_0/C_b)]$.

Histology. Lungs were clipped at the trachea, perfused with 4% paraformaldehyde (PFA), removed, and fixed for 24 hours in 4% PFA. Lungs were embedded in Paraffin (Leica ASP200S), cut into 5- μ m thick sections, and either stained with NKA α 1 (clone C464.6, EMD Millipore) after antigen retrieval with 10 mM sodium citrate at 95°C for 20 minutes or stained with H&E (Merck). Analysis was performed with an EVOS FL imaging system (Thermo Fisher Scientific).

Cell surface labeling and Western blot. Cell surface labeling and Western blot were performed as previously described (16, 69). For immunostaining, the following antibodies were used: NKA α 1, AMPK α (clone 40H9) and phospho-Acc (clone S79, both Cell Signaling Technology), polyclonal Glut1 (catalog 07-1401, EMD Millipore), β -actin (clone Poly6221, BioLegend), GAPDH (clone 14C10, Cell Signaling Technology), secondary mouse or rabbit HRP (clones 7076 and 7074, Cell Signaling Technology). Bands were detected

with the MicroChemi system (DNR Bio-Imaging Systems Ltd.) and quantified using ImageJ software.

Flow cytometry and cell sorting. Multicolor flow cytometry and cell sorting were performed with an LSR Fortessa and BD FACSAria III cell sorter using DIVA software (BD Biosciences) as previously described (16, 70). Cells ($1-5 \times 10^5$) from AEC cell cultures or derived from lavaged, perfused, and homogenized murine lungs were freshly stained with fluorochrome-labeled antibodies for 15 minutes at 4°C in BD FACS buffer (BD Biosciences). When nonlabeled primary monoclonal antibody was used, a fluorescent-labeled secondary antibody was incubated for 15 minutes at 4°C in FACS buffer. Cells were routinely stained with 7-AAD (BioLegend) for dead cell exclusion, and were also stained with antibodies to detect CD326 (clone G8.8, BioLegend), CD74 (clone ln-1, BD Biosciences), Podoplanin (clone 8.1., BioLegend), polyclonal IAV (clone ab20841, Abcam), NKAα1, CD45 (clone 30-F11, BioLegend), GR-1 (clone RB6-8C5, BioLegend), Ly6G (clone 1A8, BioLegend), SiglecF (clone E50-2440, BD Biosciences), CD11c (clone N418, BioLegend), CD11b (clone M1/70, BioLegend), secondary goat APC (clone A21447, Invitrogen), and secondary rat PE (clone A10545, Invitrogen). Corresponding isotype antibodies were used as negative controls. For annexin V staining, cells were resuspended in annexin V staining buffer (10 mM HEPES, 140 mM NaCl, and 2.5 mM CaCl_2) and incubated with annexin V Alexa Fluor 647 (1:100, Invitrogen) for 15 minutes at 4°C. Data are presented as median fluorescent intensity (MFI) and were normalized to control groups set to 1 for in vitro experiments. NKAα1⁺ AEC from in vivo-infected mice are given as a percentage of the epithelial (EpCAM⁺) cell population.

ELISA. Cell culture supernatants were analyzed using commercially available ELISA kits for mouse TRAIL (R&D Systems, detection limit 1.8 pg/ml) and mouse IFNα (PBL Interferon Source, detection limit 12.5 pg/ml), according to the manufacturer's instructions.

Quantitative PCR. RNA was isolated using RNeasy Kit (QIAGEN) and cDNA synthesized as described previously (66). Quantitative PCR (qPCR) was performed with SYBR green I (Invitrogen) in the AB StepOnePlus Detection System (Applied Bioscience). β-Actin expression served as normalization control. Data are presented as $\Delta\Delta\text{Ct}$ ($\text{dCt}_{\text{reference}} - \text{dCt}_{\text{target}}$) or fold-change ($2^{\Delta\Delta\text{Ct}}$). The following primers were used: β-actin (forward primer, 5'-ACCCTAAGGCCAACCGTGA-3'; reverse primer, 5'-CAGAGGCATACAGGGACAGCA-3'); TRAIL (forward primer, 5'-GAAGACCTCAGAAAGTGGC-3'; reverse primer, 5'-GACCAGCTCTCCATTCTTA-3').

Pulmonary transfer of BMM. BMM of WT or *Trail*^{-/-} mice recruited to the alveolar compartment after IAV challenge with 500 pfu PR8 were obtained by bronchoalveolar lavage on d7 pi after

challenge with 500 pfu PR8. BMM were identified by the signature CD45⁺GR-1⁺Ly6G⁺CD11b^{hi}CD11c^{lo}SiglecF^{lo} and flow sorted (Supplemental Figure 5). The purity of sorted BMM (≥95%) was ensured by flow cytometric analysis, as well as by pappenheim stained cytopins. Sorted BMM were resuspended in sterile PBS, and 30,000 cells in 50 μl were transferred intratracheally to PR8-infected *Ccr2*^{-/-} mice on d3 pi; the mice were analyzed for Na,K-ATPase-mediated fluid clearance on d7 pi.

Statistics. All data are given as mean ± SEM. Statistical significance was analyzed by unpaired 2-tailed Student's *t* test or by 1-way ANOVA and post-hoc Tukey (GraphPad Prism 5). A *P* value less than 0.05 was considered significant. **P* < 0.05; ***P* < 0.01; ****P* < 0.005.

Study approval. Animal experiments were approved by the regional authorities of the State of Hesse (Regierungspräsidium Giessen) and by the Institutional Animal Care and Use Committee at Northwestern University. Human lung tissue was obtained from patients who underwent lobectomy after informed written consent. Use of human lung tissue and BALF samples was approved by the University of Giessen Ethics Committee.

Author contributions

CP, CS, IV, TW, SP, REM, JL, WS, and SH were involved in study design and concept. Data were acquired by CP, BS, LMN, EL, JB, LF, and SG. GMM and GRSB were involved in the AFC measurements. Data analysis, interpretation, and statistics was conducted by CP, EL, KM, JL, JIS, IV, and SH. CP, CS, JL, JIS, and SH drafted the manuscript.

Acknowledgments

This study was supported by the German Research Foundation (SFB-TR84 B2, IRTG1062, SFB1021 C05, EXC147 to S. Herold, J. Lohmeyer, W. Seeger, S. Pleschka, and T. Wolff) by the German Federal Ministry of Research and Education ("FluResearchNet" 01 KI 1006M to S. Herold and J. Lohmeyer), and by DZL (to S. Herold, J. Lohmeyer, W. Seeger, I. Vadasz, K. Mayer, L. Fink, and R.E. Morty), by ES015024 and ES025644 (to G.M. Mutlu), and by HL-48129 and 71643 (to G.R.S. Budniger and J.I. Sznajder). The authors wish to thank U. Kalinke, and T. Mak for providing transgenic mice.

Address correspondence to: Susanne Herold, Universities Giessen & Marburg Lung Center, Department of Internal Medicine II, Klinikstr. 33, D-35392 Giessen, Germany. Phone: 49.641.985.42552; E-mail: Susanne.Herold@innere.med.uni-giessen.de.

- Jain S, et al. Hospitalized patients with 2009 H1N1 influenza in the United States, April–June 2009. *N Engl J Med*. 2009;361(20):1935–1944.
- Short KR, Kroeze EJ, Fouchier RA, Kuiken T. Pathogenesis of influenza-induced acute respiratory distress syndrome. *Lancet Infect Dis*. 2014;14(1):57–69.
- Kuiken T, Taubenberger JK. Pathology of human influenza revisited. *Vaccine*. 2008;26(suppl 4):D59–D66.
- Herold S, et al. Lung epithelial apoptosis in influenza virus pneumonia: the role of macrophage-expressed TNF-related apoptosis-inducing ligand. *J Exp Med*. 2008;205(13):3065–3077.
- Matthay MA, Ware LB, Zimmerman GA. The acute respiratory distress syndrome. *J Clin Invest*. 2012;122(8):2731–2740.
- Sznajder JI. Alveolar edema must be cleared for the acute respiratory distress syndrome patient to survive. *Am J Respir Crit Care Med*. 2001;163(6):1293–1294.
- Matthay MA. Alveolar fluid clearance in patients with ARDS: does it make a difference? *Chest*. 2002;122(6 suppl):340S–343S.
- Folkesson HG, Matthay MA. Alveolar epithelial ion and fluid transport: recent progress. *Am J Respir Cell Mol Biol*. 2006;35(1):10–19.
- Borok Z, Verkman AS. Lung edema clearance: 20 years of progress: invited review: role of aquaporin water channels in fluid transport in lung and airways. *J Appl Physiol*. 2002;93(6):2199–2206.
- Machado-Aranda D, et al. Gene transfer of the Na⁺,K⁺-ATPase β1 subunit using electroporation increases lung liquid clearance. *Am J Respir Crit Care Med*. 2005;171(3):204–211.
- Adir Y, et al. Overexpression of the Na-K-ATPase α2-subunit improves lung liquid clearance during ventilation-induced lung injury. *Am J Physiol Lung*

- Cell Mol Physiol.* 2008;294(6):L1233–L1237.
12. Lecuona E, Trejo HE, Sznajder JI. Regulation of Na⁺/K⁺-ATPase during acute lung injury. *J Bioenerg Biomembr.* 2007;39(5–6):391–395.
 13. Mutlu GM, Sznajder JI. Mechanisms of pulmonary edema clearance. *Am J Physiol Lung Cell Mol Physiol.* 2005;289(5):L685–L695.
 14. Bertorello AM, et al. Analysis of Na⁺/K⁺-ATPase motion and incorporation into the plasma membrane in response to G protein-coupled receptor signals in living cells. *Mol Biol.* 2003;14(3):1149–1157.
 15. Saldías FJ, et al. β -Adrenergic stimulation restores rat lung ability to clear edema in ventilator-associated lung injury. *Am J Respir Crit Care Med.* 2000;162(1):282–287.
 16. Högner K, et al. Macrophage-expressed IFN- β contributes to apoptotic alveolar epithelial cell injury in severe influenza virus pneumonia. *PLoS Pathog.* 2013;9(2):e1003188.
 17. Wolk KE, et al. Influenza A virus inhibits alveolar fluid clearance in BALB/c mice. *Am J Respir Crit Care Med.* 2008;178(9):969–976.
 18. Baskin CR, et al. Early and sustained innate immune response defines pathology and death in nonhuman primates infected by highly pathogenic influenza virus. *Proc Natl Acad Sci U S A.* 2009;106(9):3455–3460.
 19. De Jong MD, et al. Fatal outcome of human influenza A (H5N1) is associated with high viral load and hypercytokinemia. *Nat Med.* 2006;12(10):1203–1207.
 20. Bertorello AM, Ridge KM, Chibalin AV, Katz AI, Sznajder JI. Isoproterenol increases Na⁺/K⁺-ATPase activity by membrane insertion of α -subunits in lung alveolar cells. *Am J Physiol.* 1999;276(1):L20–L27.
 21. Lecuona E, Sun H, Vohwinkel C, Ciechanover A, Sznajder JI. Ubiquitination participates in the lysosomal degradation of Na⁺/K⁺-ATPase in steady-state conditions. *Am J Respir Cell Mol Biol.* 2009;41(6):671–679.
 22. Factor P, et al. Augmentation of lung liquid clearance via adenovirus-mediated transfer of a Na⁺/K⁺-ATPase β 1 subunit gene. *J Clin Invest.* 1998;102(7):1421–1430.
 23. Factor P, et al. Overexpression of the Na⁺/K⁺-ATPase α 1 subunit increases Na⁺/K⁺-ATPase function in A549 cells. *Am J Respir Cell Mol Biol.* 1998;18(6):741–749.
 24. Mutlu GM, et al. Upregulation of alveolar epithelial active Na⁺ transport is dependent on β 2-adrenergic receptor signaling. *Circ Res.* 2004;94(8):1091–1100.
 25. Barut S, et al. The neuroprotective effects of z-DEVD.fmk, a caspase-3 inhibitor, on traumatic spinal cord injury in rats. *Surg Neurol.* 2005;64(3):213–220.
 26. Knoblich SM, et al. Caspase inhibitor z-DEVD-fmk attenuates calpain and necrotic cell death in vitro and after traumatic brain injury. *J Cereb Blood Flow Metab.* 2004;24(10):1119–1132.
 27. Gusarova G, et al. Hypoxia leads to Na⁺/K⁺-ATPase downregulation via Ca(2+) release-activated Ca(2+) channels and AMPK activation. *Mol Cell Biol.* 2011;31(17):3546–3556.
 28. Vadász I, et al. AMP-activated protein kinase regulates CO₂-induced alveolar epithelial dysfunction in rats and human cells by promoting Na⁺/K⁺-ATPase endocytosis. *J Clin Invest.* 2008;118(2):752–762.
 29. Park SH, et al. Phosphorylation-activity relationships of AMPK and acetyl-CoA carboxylase in muscle. *J Appl Physiol.* 2002;92(6):2475–2482.
 30. Kaushik VK, et al. Regulation of fatty acid oxidation and glucose metabolism in rat soleus muscle: effects of AICAR. *Am J Physiol Endocrinol Metab.* 2001;281(2):E335–E340.
 31. Sullivan JE, et al. Inhibition of lipolysis and lipogenesis in isolated rat adipocytes with AICAR, a cell-permeable activator of AMP-activated protein kinase. *FEBS Lett.* 1994;353(1):33–36.
 32. Zhou G, et al. Role of AMP-activated protein kinase in mechanism of metformin action. *J Clin Invest.* 2001;108(8):1167–1174.
 33. Witzczak CA, Sharoff CG, Goodyear LJ. AMP-activated protein kinase in skeletal muscle: from structure and localization to its role as a master regulator of cellular metabolism. *Cell Mol Life Sci.* 2008;65(23):3737–3755.
 34. Ninomiya-Tsuji J, et al. A resorcylic acid lactone, 5Z-7-oxozeaenol, prevents inflammation by inhibiting the catalytic activity of TAK1 MAPK kinase. *J Biol Chem.* 2003;278(20):18485–18490.
 35. Herold S, et al. Alveolar epithelial cells direct monocyte transepithelial migration upon influenza virus infection: impact of chemokines and adhesion molecules. *J Immunol.* 2006;177(3):1817.
 36. Lazrak A, et al. Influenza virus M2 protein inhibits epithelial sodium channels by increasing reactive oxygen species. *FASEB J.* 2009;23(11):3829–3842.
 37. Londino JD, et al. Influenza matrix protein 2 alters CFTR expression and function through its ion channel activity. *Am J Physiol Lung Cell Mol Physiol.* 2013;304(9):L582–L592.
 38. Jewell NA, et al. Differential type I interferon induction by respiratory syncytial virus and influenza A virus in vivo. *J Virol.* 2007;81(18):9790–9800.
 39. Hayden FG, et al. Local and systemic cytokine responses during experimental human influenza A virus infection. Relation to symptom formation and host defense. *J Clin Invest.* 1998;101(3):643–649.
 40. Arimori Y, et al. Type I interferon limits influenza virus-induced acute lung injury by regulation of excessive inflammation in mice. *Antiviral Res.* 2013;99(3):230–237.
 41. Steel J, et al. Transmission of pandemic H1N1 influenza virus and impact of prior exposure to seasonal strains or interferon treatment. *J Virol.* 2010;84(1):21–26.
 42. Kugel D, et al. Intranasal administration of alpha interferon reduces seasonal influenza A virus morbidity in ferrets. *J Virol.* 2009;83(8):3843–3851.
 43. Tumpey TM, et al. Pathogenicity of influenza viruses with genes from the 1918 pandemic virus: functional roles of alveolar macrophages and neutrophils in limiting virus replication and mortality in mice. *J Virol.* 2005;79(23):14933–14944.
 44. Lin KL, Suzuki Y, Nakano H, Ramsburg E, Gunn MD. CCR2+ monocyte-derived dendritic cells and exudate macrophages produce influenza-induced pulmonary immune pathology and mortality. *J Immunol.* 2008;180(4):2562–2572.
 45. Chan M, et al. Proinflammatory cytokine responses induced by influenza A (H5N1) viruses in primary human alveolar and bronchial epithelial cells. *Respir Res.* 2005;6(135):1–13.
 46. Herold S, Becker C, Ridge KM, Budinger GRS. Influenza virus-induced lung injury: pathogenesis and implications for treatment. *Eur Respir J.* 2015;45(5):1463–1478.
 47. Kim HM, et al. Alveolar macrophages are indispensable for controlling influenza viruses in lungs of pigs. *J Virol.* 2008;82(9):4265–4274.
 48. Walsh KB, et al. Suppression of cytokine storm with a sphingosine analog provides protection against pathogenic influenza virus. *Proc Natl Acad Sci U S A.* 2011;108(29):12018–12023.
 49. Van Reeth K. Cytokines in the pathogenesis of influenza. *Vet Microbiol.* 2000;74(1–2):109–116.
 50. Szretter KJ, et al. Role of host cytokine responses in the pathogenesis of avian H5N1 influenza viruses in mice. *J Virol.* 2007;81(6):2736–2744.
 51. To KK, et al. Delayed clearance of viral load and marked cytokine activation in severe cases of pandemic H1N1 2009 influenza virus infection. *Clin Infect Dis.* 2010;50(6):850–859.
 52. Davidson S, Crotta S, McCabe TM, Wack A. Pathogenic potential of interferon $\alpha\beta$ in acute influenza infection. *Nat Commun.* 2014;5:3864.
 53. Baritaki S, et al. Regulation of tumor cell sensitivity to TRAIL-induced apoptosis by the metastatic suppressor Raf kinase inhibitor protein via Yin Yang 1 inhibition and death receptor 5 up-regulation. *J Immunol.* 2007;179(8):5441–5453.
 54. Song K, Benhaga N, Anderson RL, Khosravi-Far R. Transduction of tumor necrosis factor-related apoptosis-inducing ligand into hematopoietic cells leads to inhibition of syngeneic tumor growth in vivo. *Cancer Res.* 2006;66(12):6304–6311.
 55. Liu C, Liang B, Wang Q, Wu J, Zou MH. Activation of AMP-activated protein kinase α 1 alleviates endothelial cell apoptosis by increasing the expression of anti-apoptotic proteins Bcl-2 and survivin. *J Biol Chem.* 2010;285(20):15346–15355.
 56. Hardie DG, Scott JW, Pan DA, Hudson ER. Management of cellular energy by the AMP-activated protein kinase system. *FEBS Lett.* 2003;546(1):113–120.
 57. Herrero-Martín G, et al. TAK1 activates AMPK-dependent cytoprotective autophagy in TRAIL-treated epithelial cells. *EMBO J.* 2009;28(6):677–685.
 58. Moseley CE, Webster RG, Aldridge JR. Peroxisome proliferator-activated receptor and AMP-activated protein kinase agonists protect against lethal influenza virus challenge in mice. *Influenza Other Respir.* 2010;4(5):307–311.
 59. Hoffmann HH, Palese P, Shaw ML. Modulation of influenza virus replication by alteration of sodium ion transport and protein kinase C activity. *Antiviral Res.* 2008;80(2):124–134.
 60. Wang L, et al. “Tuning” of type I interferon-induced Jak-STAT1 signaling by calcium-dependent kinases in macrophages. *Nat Immunol.* 2008;9(2):186–193.
 61. Ellis GT, Davidson S, Crotta S, Branzk N, Papayannopoulos V, Wack A. TRAIL+ monocytes

- and monocyte-related cells cause lung damage and thereby increase susceptibility to influenza-Streptococcus pneumoniae coinfection. *EMBO Rep.* 2015;16(9):1203-1218.
62. Cretney E, et al. Increased susceptibility to tumor initiation and metastasis in TNF-related apoptosis-inducing ligand-deficient mice. *J Immunol.* 2002;168(3):1356-1361.
63. Müller U, et al. Functional role of type I and type II interferons in antiviral defense. *Science.* 1994;264(5167):1918-21.
64. Finnberg N, et al. DR5 knockout mice are compromised in radiation-induced apoptosis. *Mol Cell Biol.* 2005;25(5):2000-2013.
65. Kuziel WA, et al. Severe reduction in leukocyte adhesion and monocyte extravasation in mice deficient in CC chemokine receptor 2. *Proc Natl Acad Sci U S A.* 1997;94(22):12053-12058.
66. Cakarova L, et al. Macrophage tumor necrosis factor- α induces epithelial expression of granulocyte-macrophage colony-stimulating factor: impact on alveolar epithelial repair. *Am J Respir Crit Care Med.* 2009;180(6):521-532.
67. Barwe SP, et al. Novel role for Na,K-ATPase in phosphatidylinositol 3-kinase signaling and suppression of cell motility. *Mol Biol.* 2005;16(3):1082-1094.
68. Hardiman KM, Lindsey JR, Matalon S. Lack of amiloride-sensitive transport across alveolar and respiratory epithelium of iNOS(-/-) mice in vivo. *Am J Physiol Lung Cell Mol Physiol.* 2001;281(3):L722-731.
69. Dada LA, et al. Hypoxia-induced endocytosis of Na,K-ATPase in alveolar epithelial cells is mediated by mitochondrial reactive oxygen species and PKC- ζ . *J Clin Invest.* 2003;111(7):1057-1064.
70. Unkel B, et al. Alveolar epithelial cells orchestrate DC function in murine viral pneumonia. *J Clin Invest.* 2012;122(10):3652-3664.